Hemispheric contrasts of ice formation in stratiform supercooled liquid clouds

Long-term observations with the ground-based remote-sensing supersite LACROS

Von der Fakultät für Physik und Geowissenschaften
der Universität Leipzig
genehmigte

Dissertation

zur Erlangung des akademischen Grades

Doctor rerum naturalium
Dr. rer. nat.

vorgelegt

von Martin Radenz, M.Sc. Meteorologie
geboren am 03. Mai 1991 in Hof

Gutachter: Prof. Dr. Andreas Macke
Prof. Dr. Julia Schmale

Tag der Verleihung 24. Januar 2022

Bibliographische Beschreibung:

Radenz, Martin
Hemisphärische Kontraste der Eisbildung in Schichtwolken aus unterkühltem Wasser: Langzeitbeobachtungen mit der bodengebundenen Fernerkundungsplattform LACROS
Universität Leipzig, Dissertation
133 Seiten, 217 Literaturzitate, 46 Abbildungen, 6 Tabellen

Referat:
Die vorliegende Arbeit untersucht hemisphärische Unterschiede der heterogenen Eisbildung in unterkühlten Schichtwolken auf Basis von drei Datensätzen, die mit der mobilen bodengebundenen Fernerkundungsplattform LACROS (Leipzig Aerosol and Cloud Remote Observations System; Leipziger Aerosol- und Wolken- Fernerkundungssystem) erhoben wurden. Für die Nordhemisphäre wurden zwischen 2014 und 2018 gesammelte LACROS-Datensätze aus Leipzig (Deutschland, 51,4°N, 12,4°E) und Limassol (Zypern, 34,7°N, 33,0°E) verwendet. Ein zentraler Bestandteil dieser Arbeit war die Umsetzung des mehr als zwei Jahre umfassenden Einsatzes von LACROS im Rahmen der Kampagne DACAPO-PESO (Dynamics Aerosol Clouds And Precipitation Observation in the Pristine Environment of the Southern Ocean; Beobachtung von Dynamik, Aerosol, Wolken und Niederschlag in der unverschmutzen Umgebung des Südozeans) in Punta Arenas, Chile (53,1°S, 70,9°W). Dieser Datensatz stellt die ersten mehrjährigen bodengebundenen Fernerkundungsbeobachtungen in der westlichen Hälfte des Südozeans dar. Durch die Kombination aus Radar- und Lidarinstrumenten, einschließlich der Fähigkeit Vertikalbewegungen zu beobachten, ist es möglich, mit LACROS Aerosol-Wolken-Dynamik-Wechselwirkungen detailliert zu untersuchen. Von großer Bedeutung für die Umsetzung der Arbeit war die durchgeführte Entwicklung und Integration eines automatisierten Datenanalyseschemas. Besonders hervorzuheben sind die kontinuierliche Charakterisierung der Luftmassenherkunft, die Auswertung von multiplen Maxima im Wolkenradar-Dopplerspektrum, eine Methode zur Erkennung von durch Schwerewellen beeinflussten Wolken mit Doppler Lidar und die Integration aller Datenquellen in die verteilte LACROS-Forschungsdatenanwendung. Wichtigste Ergebnisse dieser Arbeit sind, dass atmosphärische Schwerewellen die Bildung und Detektierbarkeit der Eisphase erschweren und dass eine Kopplung von Wolken mit der planetaren Grenzschicht die Häufigkeit der Eisbildung erhöht. Wenn diese beiden Effekte berücksichtigt werden, tritt Eisbildung in Schichtwolken über Punta Arenas etwas weniger häufig auf als über Limassol und Leipzig. Dieser Unterschied kann auf eine geringere Verfügbarkeit von Eiskeimen in der freien Troposphäre über Punta Arenas zurückgeführt werden.

Bibliographic Description:

Radenz, Martin
Hemispheric contrasts of ice formation in stratiform supercooled liquid clouds: Long-term observations with the ground-based remote-sensing supersite LACROS
University of Leipzig, Dissertation
133 Pages, 217 References, 46 Figures, 6 Tables

Abstract:
This work investigates hemispheric contrasts of ice formation in stratiform supercooled liquid clouds using observations of three long-term campaigns of the mobile ground-based remote-sensing supersite LACROS (Leipzig Aerosol and Cloud Remote Observations System). For the northern hemisphere, LACROS datasets collected at Leipzig (Germany, 51.4°N, 12.4°E) and Limassol (Cyprus, 34.7°N, 33.0°E) between 2014 and 2018 were used. A key component of this work was the implementation of the more than two-year-long deployment of LACROS as part of the Dynamics Aerosol Clouds And Precipitation Observation in the Pristine Environment of the Southern Ocean (DACAPO-PESO) field campaign at Punta Arenas (Chile, 53.1°S, 70.9°W). The dataset assembled during this campaign resembles the first comprehensive multi-year ground-based remote-sensing dataset in the western part of the Southern Ocean. The synergistic combination of radar and lidar, including the capability to observe vertical velocities, allows detailed investigation of aerosol-cloud-dynamics interaction. One major part of this work was the development and integration of an automated data analysis scheme. Highlights are a continuous time-height-resolved airmass source characterization, a multi-peak analysis algorithm for radar Doppler spectra, a gravity-wave identification method based on Doppler lidar-vertical velocity observation, and the integration of the data sources into the distributed LACROS Research Data Application. The most important results of this work were that atmospheric gravity waves impede the formation and detectability of the ice phase, whereas the coupling of clouds with the planetary boundary layer increases the frequency of ice formation. When these two effects are taken into account, ice formation in stratiform clouds over Punta Arenas occurs slightly less frequent than over Limassol and Leipzig. This difference can be attributed to a lower availability of ice nuclei in the free troposphere over Punta Arenas.

"The mysteries of cloud formation, and the precipitation that can follow, have proven to be one of the most challenging aspects of the global climate system. Except for man himself, the weather is probably the most variable, unreliable, and fluctatory phenomenom of which human intelligence has dared to attempt science."

Joanne Malkus, 1962

Contents

1 Introduction

Clouds are one of the most volatile components of the Earth's climate system. Depending on their optical thickness, thermodynamic phase, and temperature, they may warm or cool our planet. As a prerequisite for precipitation, they govern the weather and provide fresh water. Nevertheless, we still struggle to understand the processes that control their formation and life cycle. Especially the microphysics of mixed-phase clouds is a topic of current research. At temperatures between 0 and about $-40\,^{\circ}\mathrm{C}$ supercooled liquid droplets and ice crystals can coexist. Though, different saturation water vapor pressures over water and ice make this coexistence thermodynamically unstable. Aerosol particles are a prerequisite for initial formation of liquid droplets and ice crystals from the vapor phase, but clouds and aerosol particles are entangled via complex pathways of interaction. In the first place, aerosol particles are required as cloud condensation nuclei (CCN) on which liquid droplets can nucleate. On the other hand, primary ice formation in the heterogeneous freezing temperature range (0 to about $-40\,^{\circ}\mathrm{C}$) requires ice-nucleating particles (INP) to be present in the aerosol reservoir. The ways in which aerosol and cloud particles interact are controlled by the dynamics and thermodynamics of the atmospheric environment, with temperature being the most important driver, impacting ice formation itself and subsequent growth by water vapor deposition. Equally important are vertical motions of air, as cooling during adiabatic ascend determines the available supersaturation activation of INP. Thermodynamic processes are considered dominating the cloud microphysical properties compared to aerosol-related influences. This dominance makes it difficult to isolate aerosol-related effects in observed cloud properties. A typical structure of mixed-phase clouds in the heterogeneous freezing regime is a liquid-dominated layer at cloud top and ice sedimenting out of the liquid base (Barrett et al., 2017). The temperature at the top of the liquid layer is usually the lowest temperature found in a stratiform cloud. Hence, this cloud top temperature (CTT) is a feasible first constraint of the thermodynamics controlling the cloud.

Despite the dominance of dynamics and thermodynamics, observations as well as aerosol-permitting model studies suggest a considerable influence of the aerosol conditions on the properties and evolution of clouds and precipitation (Seifert et al., 2012; Rosenfeld et al., 2008; Possner et al., 2017; Solomon et al., 2018; Zhang et al., 2018). Solomon et al. (2018) used high-resolution modeling of Arctic mixed-phase clouds to show that perturbations in the INP concentration dominate over changes in the CCN concentration. Cloud chamber studies suggest that for constant CCN concentration, the ratio of ice-water to liquid-water content in the steady state is predominantly controlled by INP concentrations (Desai et al., 2019).

Aerosol load and composition vary strongly across the globe, with especially strong contrasts between mid-latitudes of the northern and southern hemisphere (e.g., Tegen et al., 1997; Kinne, 2019). Similarly, there is distinct spatio-temporal variability in the performance of weather and climate model simulations, with less accurate results in the southern hemisphere. This difference in performance is attributed to the insufficient representation of aerosol-cloud-dynamics interaction processes in the models (Fan et al., 2016; Seinfeld et al., 2016). For instance, a less accurate treatment of the radiative balance in the southern-hemispheric mid-latitudes compared to their northern-hemispheric counterparts was found (Trenberth and Fasullo, 2010; Grise et al., 2015). The reported biases in the solar radiation budget are attributed to shallow supercooled liquid-topped clouds, which are insufficiently represented by current models (Bodas-Salcedo et al., 2014; Kay et al., 2016; Bodas-Salcedo et al., 2016; Kuma et al., 2020). With the frequency of liquid-cloud tops too low, less short-wave radiation is reflected. Hence, the simulations show a too strong heating at the surface, leading to a bias in ocean heat uptake (Franklin et al., 2013; Hyder et al., 2018).

Correct treatment of the processes related to supercooled stratiform clouds in the southern hemisphere is crucial for climate prediction, as a large share of the anthropogenic carbon and heat is stored in the Southern Ocean (Frölicher et al., 2015). There is an ongoing controversy about the reasons for the observed differences and prevailing model deficiencies, but indications are given that a combination of hemispheric contrasts in aerosol load—especially the low abundance of INP form terrestrial sources—and atmospheric dynamics plays a role. These findings lead to the first overarching research question (RQ) of this work:

RQ I: Are there aerosol-related contrasts in ice formation in stratiform mixed-phase clouds in the mid-latitudes of the southern hemisphere and the polluted northern hemisphere?

In numerous previous studies, liquid-topped supercooled stratiform cloud layers have been proven to be suitable natural laboratories for the investigation of the relationships between aerosol properties, thermodynamics, and microphysical properties of clouds in the heterogeneous freezing regime. Turbulence is usually confined to the liquid-dominated cloud top (Westbrook and Illingworth, 2013; de Boer et al., 2009) and due to the limited thickness of this layer, secondary ice formation or ice multiplication are inhibited (Fukuta and Takahashi, 1999; Myagkov et al., 2016a). The temperature at which the ice formation occurs needs to be well defined, because the concentration of efficient INP increases rapidly with decreasing temperature (e.g., Kanji et al., 2017) and thus the amount of ice formed increases with decreasing temperature (Bühl et al., 2016).

Supercooled liquid clouds are frequent over the Southern Ocean (Hu et al., 2010; Huang et al., 2015; Tan et al., 2014). Studies by Kanitz et al. (2011) and Choi et al. (2010) showed, that—at similar temperatures—ice is formed less frequently in supercooled liquid layers in the southern compared with northern mid-latitudes. The study of Kanitz et al. (2011) first used a ground-based lidar at Punta Arenas (53.1°S,

70.9°W, Chile) to asses the thermodynamic phase of stratiform mixed-phase clouds in the southern mid-latitudes. Alexander and Protat (2018), using ground-based lidar and A-Train observations from Cape Grim (40.7°S, 144.7°E, Australia),confirmed the basic findings also for the eastern parts of the Southern Ocean. Only recently, more extensive observations became available from the Southern Ocean, including shipborne, land-based, and aircraft campaigns. Most of these efforts targeted aerosols and clouds above the Southern Ocean between Australia and Antarctica (60 to 160°E). An overview is provided by McFarquhar et al. (2020). Using a shipborne remote-sensing dataset, Mace and Protat (2018) also found frequent supercooled liquid layers between Australia and Antarctica. Zaremba et al. (2020) investigated airborne active remote-sensing observations of Southern Ocean clouds south of Tasmania. They found widespread liquid cloud tops at temperatures down to −30 °C. Though, limited sampling at single heights provides no information on the vertical structure of clouds. Also sampling inside supercooled liquid layers is difficult due to aircraft and sensor icing. By investigating the ground-based remote-sensing dataset assembled at McMurdo (77.8°S, 166.7°E, Antarctica), Silber et al. (2018) found frequent long-lived liquid-topped clouds, even below −30 °C.

Different causes for regional contrasts in the abundance of supercooled liquid cloud layers are proposed. On the one hand, a reason for the excess of supercooled liquid water in southern-hemispheric cloud systems could be the inhibition of ice formation caused by the lack of INP in the predominantly pristine environment of the Southern Ocean (Hamilton et al., 2014), where terrestrial sources, which are considered as the major source for INP, are rare or far apart (Vergara-Temprado et al., 2017). In a study that assembled observations from several shipborne campaigns, Welti et al. (2020) corroborated the low INP concentrations in that regions. Recent studies based on the A-Train satellite constellation suggest systematically lower ice amounts in the southern mid-latitudes (Zhang et al., 2018) and a strong susceptibility to dust load (Villanueva et al., 2020). By adding marine organic aerosol as an explicit species to an Earth system model, Zhao et al. (2021) confirmed this finding and identified marine organic aerosol as the primary ice nuclei above the Southern Ocean. Liquid layers in deeper clouds, observed during another shipborne campaign (McFarquhar et al., 2020; Alexander et al., 2021), could only be reproduced in regional model simulations, when the INP parametrization was tuned to lower concentrations (Vignon et al., 2021). Comparing airborne aerosol observations from the Northern Atlantic and the Southern Ocean, Minikin et al. (2003) reported a factor 2 to 3 lower aerosol concentration in the free troposphere of the southern mid-latitudes. Consequently, Gayet et al. (2004) derived lower ice crystal number concentrations (ICNCs) compared to the northern mid-latitudes in cirrus clouds from the same dataset.

In the heterogeneous freezing regime, suitable aerosol particles are a prerequisite for ice formation. Without ice formation as a sink for cloud water, the liquid phase may be sustained for long periods of time. On the other hand, dynamical processes could lead to an enhancement of supercooled liquid water. Korolev (2007) showed, that depending on the number and size of ice crystals, a threshold vertical velocity can be

found, which allows for sufficient supersaturation to grow the ice as well as the liquid phase. Gravity waves have been suggested playing a role in the phase partitioning of Southern Ocean clouds (Alexander et al., 2017; Silber et al., 2020). Due to the orographic effects and the strong westerlies, gravity waves are a general feature in the vicinity of all landmasses in the middle and high latitudes of the southern hemisphere (Sato et al., 2012; Alexander et al., 2016). Also, stronger turbulence increases the amount of ice formed in stratiform cloud layers (Bühl et al., 2019a). Indications are thus given that it is necessary to also consider turbulence in studies of ice formation. The potential contribution of aerosol-related and dynamical effects to contrasts in the frequency of supercooled liquid cloud layers motivate the second research question of this thesis:

RQ II: Is the reported high frequency of supercooled liquid water in the southern hemisphere caused by the low abundance of INP alone?

Generally, aerosol load in the free troposphere is lower than in the boundary layer (e.g., Bourgeois et al., 2018). Griesche et al. (2021) found a strong increase in the frequency of ice formation for cloud layers coupled to the surface via the boundary layer. So far, no similar investigation is available for mid-latitudes, especially for the southern hemisphere. The importance of surface coupling on cloud properties is further underlined by the challenges satellite-derived datasets face in characterization of low, shallow clouds (Alexander and Protat, 2018; McErlich et al., 2021). Hence, research question three is posed as:

RQ III: Do enhanced INP concentrations in surface-coupled cloud layers influence the frequency of ice formation?

Still, only few long-term observations are available from the southern mid-latitudes, and most of them are either based on lidar-only or spaceborne radar-lidar datasets with limited sensitivity. As shown by Bühl et al. (2013a) for the northern mid-latitudes, most of the ice formation by stratiform clouds at temperatures above $-12\,^{\circ}\mathrm{C}$ is missed by these instruments. Using a shipborne remote-sensing dataset, Mace and Protat (2018) also found frequent liquid-dominated clouds with low radar reflectivities, and one-third of the liquid layers could only be observed with lidar. Comparing the observations with a Cloud-Aerosol Lidar and Infrared Pathfinder Satellite Observations (CALIPSO) dataset from Hu et al. (2010), they found an underestimation of ice, especially strong at temperatures above $-15\,^{\circ}\mathrm{C}$. Consequently, such satellite datasets overestimate the frequency of liquid-only supercooled clouds at those temperatures. Comparing CALIPSO observations with airborne in-situ data, Ahn et al. (2018) came to a similar conclusion. In a follow-up study, Mace et al. (2020) refined the CALIPSO classification scheme, which led to more frequent detections of the mixed-phase, especially during wintertime and in the lower latitudes of the Southern Ocean. However, no CTT-resolved phase occurrence statistics was presented. The ground-based studies by Kanitz et al. (2011) and Alexander and Protat (2018) are also solely based on lidar. Hence, research question four is the following:

RQ IV: Did prior lidar-only studies underestimate the frequency of ice formation at high temperatures?

This thesis addresses the research questions I-IV in the framework of a contrasting study by comparing the cloud properties at locations with differing aerosol load. Contrasting studies, such as done, e.g., by Kanitz et al. (2011), Seifert et al. (2015), Zhang et al. (2018), and Villanueva et al. (2020) have proved successful in pinpointing aerosol-related differences in cloud microphysics. When collected with identical instrumentation, aerosol and cloud properties observed at different locations can be compared. To determine the impact of varying aerosol load and composition on clouds, targeted long-term observations at suitable sites have to be performed. However, the dynamical forcing on the cloud under investigation needs to be comparable between the sites as well, a task which is not easily achieved for satellite-based datasets, such as the ones used by Villanueva et al. (2021).

So far, a statistical analysis of the relationships between aerosol conditions, cloud dynamics, and the phase partitioning in stratiform cloud layers of the southern mid-latitudes based on long-term observations has not been established. One reason is that, despite increased activity in the recent past, ground-based remote-sensing observations of clouds and aerosol are still sparsely distributed in the Southern Ocean and at the coast of Antarctica. Even those recent campaigns are mainly focused on austral summer and are usually limited to periods less than a year.

To address the need for comprehensive long-term observations, the mobile Leipzig Aerosol and Cloud Remote Observations System (LACROS) has been deployed at Punta Arenas (53.1°S, 70.9°W, Chile) for the Dynamics Aerosol Clouds And Precipitation Observation in the Pristine Environment of the Southern Ocean (DACAPO-PESO) field campaign since November 2018. The core instrumentation of LACROS consists of a polarimetric Doppler cloud radar, a multi-wavelength Raman polarization lidar, a microwave radiometer, and a Doppler lidar. These instruments are combined to provide comprehensive observations of cloud and aerosol properties as well as vertical motions. Considerable effort was spent within the framework of this thesis in planning, preparing, and conducting this field campaign. The resulting dataset and data of observations by LACROS at Leipzig (51.4°N, 12.4°E, Germany) and Limassol (34.7°N, 33.0°E, Cyprus) are used for the contrasting study. Together, these three datasets cover the aerosol conditions of a continental northern-hemispheric background site, a hot-spot of mineral dust, and the marine-dominated pristine Southern Ocean. Hence, the datasets collected with a single set of ground-based remote-sensing instrumentation provide an ideal basis for contrasting studies. The broad variety of instruments covers the decisive properties of aerosols, dynamics, clouds, and precipitation for a comprehensive picture of aerosol-cloud interaction. The observations at Punta Arenas provide the first multi-year dataset of synergistic ground-based remote-sensing observations in the western half of the Southern Ocean and allow us to contextualize prior findings, especially the ones by Kanitz et al. (2011).

Analyzing the large datasets collected by the various instruments of LACROS at

three different locations requires sophisticated methods and retrievals. While well-established synergistic retrievals such as Cloudnet (Illingworth et al., 2007) or the lidar processing chain of PollyNET (Baars et al., 2016; Baars et al., 2017; Yin and Baars, 2021) are readily available and provide the backbone of the data analysis, yet not all crucial aspects are covered. Work published in two peer-reviewed publications contributed important methodological extensions and is included into this thesis. When multiple hydrometeor species coexist within a cloud radar observation volume, they frequently appear as distinct peaks in the Doppler spectrum because of their different terminal velocities. This multi-peak information is not yet routinely used in synergistic retrievals due to the complexity of this information. In Radenz et al. (2019a) the structure-preserving Doppler spectra analysis technique peakTree, which helps to access this complexity with automated algorithms is introduced. The second publication addresses the issue of airmass source estimates for continuous profiling observations. In Radenz et al. (2021a) a method for obtaining a continuous time-height-resolved airmass source attribution from backward simulations is described. A third paper, Radenz et al. (2021b), includes a scheme for the identification of gravity waves using the autocorrelation of the Doppler lidar vertical velocity and covers the obtained contrasts in the frequency of ice formation. A full publication record is provided in the appendix.

The remainder of this thesis is structured as follows. In Chapter 2, a brief overview on microphysics in shallow mixed-phase clouds including the impact of vertical motions is given. Afterwards, Chapter 3 introduces the mobile ground-based remote-sensing facility LACROS and the campaigns covered in this work. Naturally, the recent Punta Arenas deployment is the main focus. The data processing chain and synergistic retrievals are explained in Chapter 4. Methods that were newly developed and published are described extensively in this section, including case examples. Already existing retrievals such as the Cloudnet algorithm and the PollyNET processing chain are only briefly introduced. An overview on the thermodynamic conditions, cloud occurrence, and lidar-derived aerosol properties for all three datasets is given in Chapter 5. Afterwards, Chapter 6 focuses on the properties of stratiform mixed-phase clouds, especially the frequency of ice formation. Here, the effects of instrument sensitivity, surface coupling, and gravity waves on cloud phase are addressed. The amount and efficiency of ice production by mixed-phase clouds is also quantified. In Chapter 7, the long-term statistics of the multi-peak radar Doppler spectra are presented. The identification of conditions, under which multiple particle populations coexist, serves as a first step for future investigation of deeper clouds. A summary and outlook conclude the work.

2 Heterogeneous ice formation in shallow mixed-phase clouds

This chapter briefly introduces some theoretical concepts that are useful to understand processes in mixed-phase clouds. Starting with primary ice nucleation, the relevance of aerosol particles for this process is described. Once the three phases, water vapor, liquid droplets, and solid ice crystals coexist, the further evolution of the cloud depends on the mass transfer between the phases. Vertical motion crucially controls this transfer, but for stratiform clouds, frequently an almost steady state is reached. The ice particles grow via deposition of water vapor and at some point the particles are large enough to sediment out of the mixed-phase layer. Ice particles may also grow by the collection of liquid or other ice particles, also called riming and aggregation, respectively. Large ice crystals might also shatter, with their fragments explosively enhancing the number of ice particles. An overview on the complexity of these interactions is given, e.g., by Seifert and Beheng (2006). To isolate the process of primary ice formation, this work focuses on shallow stratiform cloud layers. As described in multiple studies such as Ansmann et al. (2008), Seifert et al. (2010), Bühl et al. (2016), and Barrett et al. (2017) stratiform mixed-phase clouds have a distinct structure with a liquid or liquid-dominated layer at top and an ice virga below. Due to this structure, ground-based remote sensing is well suited to investigate primary ice formation in such clouds.

Ice nucleation is a stochastic process and can be described in terms of classical nucleation theory (CNT). Overviews are given, e.g., by Murray et al. (2012) and Kanji et al. (2017). To freeze a liquid droplet, a cluster of ice needs to form inside the liquid, which is able to overcome the barrier in the Gibbs free energy ΔG_{hom}. ΔG_{hom} depends on the radius of the cluster r_G and is the sum of a surface term proportional to the radius ${r_G}^2$ and a volume term proportional to ${r_G}^3$, with the equations provided, e.g., by Murray et al. (2012). At the critical radius r_G^*, the volume term starts to dominate over the surface term. Once the cluster is larger than r_G^*, further growth is energetically favored and the droplet freezes. With stronger supercooling, the critical size r_G^* and the energy barrier $\Delta G_{\mathrm{hom}}^*$ get smaller. Homogeneous freezing only occurs at temperatures below about $-38\,^{\circ}\mathrm{C}$ (Pruppacher and Klett, 1997).

Freezing may occur at higher temperatures as well, if a suitable solid substrate, i.e., an INP, is available on which the ice cluster may form. This freezing pathway is called heterogeneous freezing. Different pathways or modes of nucleation have been proposed (see Murray et al., 2012; Vali et al., 2015, for an overview). In the case of deposition nucleation, the water vapor deposits to the INP without liquid involved. Immersion freezing requires an INP inside the droplet to trigger freezing, whereas

for contact nucleation an INP collides with the droplet and then triggers freezing. It is still open to debate, if the latter two processes can be distinguished outside of laboratory experiments. Variants of these modes have also been proposed, such as droplet collision or evaporation favoring the freezing. But also their relevance is still unknown. In terms of Gibbs free energy, the surface of the INP reduces the energy barrier to $\Delta G^*_{\mathrm{het}} = \Delta G^*_{\mathrm{hom}} f(\Theta)$, with $f(\Theta)$ describing the efficiency of an INP in terms of the contact angle Θ. Based on CNT, the nucleation rate $\mathrm{d}N_{\mathrm{l}\to\mathrm{i}}$ depends on the nucleation-rate coefficient $j_{\mathrm{het}}(T, \Theta)$, the INP surface area A_{n}, and the number of droplets N_{l}:

$$\mathrm{d}N_{\mathrm{l}\to\mathrm{i}} = N_{\mathrm{l}} A_{\mathrm{n}} j_{\mathrm{het}}(T, \Theta)\mathrm{d}t. \tag{2.1}$$

For naturally occurring INP, a single contact angle is generally not sufficient to describe the freezing behavior. A stochastic distribution of contact angles can be used to improve the description of a weak time dependence in some laboratory studies (e.g., Niedermeier et al., 2011). For many INP populations, the time dependence is much less important than the temperature dependence (Vali, 2014). Under this condition, the more simple singular hypothesis is a sufficient description of ice formation. An INP is conceptualized to have nucleation sites at its surface. Each of these sites may trigger freezing at a characteristic temperature. The activation of the INP as a whole is then determined by the highest of those characteristic temperatures, i.e., a droplet freezes once the characteristic temperature for the 'best' site is reached.

In terms of a droplet population at a certain temperature, all droplets are frozen, which contain INP with surface sites acting at a higher characteristic temperature (Connolly et al., 2009):

$$\mathrm{d}N_{\mathrm{l}\to\mathrm{i}} = N_{\mathrm{l}} A_{\mathrm{n}} \frac{\mathrm{d}n_{\mathrm{s}}(T)}{\mathrm{d}T}\mathrm{d}T, \tag{2.2}$$

where $n_{\mathrm{s}}(T)$ is the temperature-dependent ice-active surface site density. From the singular hypothesis it becomes clear that the nucleation rate only depends on the number of activated sites for a certain amount of cooling, where the number of active sites depends on the composition and size of the aerosol particles and their distribution within the droplets.

Generally, INP are a small subset of aerosol particles and their number increases with decreasing temperature. Petters and Wright (2015) provided an overview on concentrations, typically observed in the atmosphere, ranging from 10^{-6} to $10^{-2}\,\mathrm{L}^{-1}$ at $-5\,^{\circ}\mathrm{C}$ and 10^{2} to $10^{4}\,\mathrm{L}^{-1}$ at $-35\,^{\circ}\mathrm{C}$. Though depending on location, height, and airmass source, a variability of several orders of magnitude is observed (e.g., Welti et al., 2020). Much effort is put into characterizing what subset of aerosol particles serves as a reservoir for INP (Kanji et al., 2017; Hoose and Möhler, 2012). The most abundant INP in the atmosphere is considered to be mineral dust, which predominantly is ice-active below $-15\,^{\circ}\mathrm{C}$. Mineral dust particles fulfill two criteria that are considered a prerequisite for ice activity: insolubility and large size (Pruppacher and Klett, 1997). More recent research found that also soluble components, such as certain biological macromolecules with sizes of about 10 nm, can show ice activity (Pummer et al., 2015). These macromolecules were also found sticking to other aerosol particles such as soil

dust, thus significantly enhancing the ice activity of the latter (Conen et al., 2011). Especially fungal spores and soil dusts were found to be efficient INP at temperatures above −10 °C (O′Sullivan et al., 2015).

While different modes of heterogeneous ice formation are discussed (see Vali et al., 2015, for an overview), immersion freezing is considered the predominant pathway in mixed-phase clouds and was identified to dominate heterogeneous freezing at temperatures above approximately −25 °C (Ansmann et al., 2008; Westbrook and Illingworth, 2011; Hoose and Möhler, 2012; Murray et al., 2012). For immersion freezing, first a liquid droplet has to form, then freezing is triggered by an INP already residing inside the droplet. The immersion freezing process is suspected to be even more efficient during droplet evaporation, when ice formation is triggered at the time of contact between the shrinking droplet surface and the immersed INP (Durant, 2005). Based on Eq. (2.2), parametrizations of heterogeneous ice nucleation in the immersion mode are available (Connolly et al., 2009; Niemand et al., 2012; Diehl and Mitra, 2015). When a population of liquid droplets N_l is cooled from T_0 to T_1, ΔN_i additional ice crystals will form:

$$\Delta N_\mathrm{i} = N_\mathrm{l} \left(1 - \exp\left\{A_\mathrm{n} \left[n_\mathrm{s}(T_1) - n_\mathrm{s}(T_0)\right]\right\}\right). \tag{2.3}$$

This description is only valid for a single, monodisperse INP population. If no sites become ice-active in the temperature interval between T_0 and T_1, no additional ice particles will form.

Other formulations of freezing parametrizations are not based on the surface concentration, but on the bulk number of aerosol particles larger than a certain threshold (e.g., DeMott et al., 2010; Tobo et al., 2013; DeMott et al., 2015). In the atmosphere, a mixture of aerosol particles with different sizes and ice-activation characteristics is nucleating ice, which further complicates the description of this process. In addition to a correct understanding of the complexity of ice nucleation itself, a precise characterization of the aerosol mixture in the cloud volume is needed. Nevertheless, the key message from the stochastic hypothesis is that for a given cloud volume any additional ice nucleation requires cooling and hence updrafts. In the absence of suitable INP, no ice particles might form at all and the cloud will consist of supercooled liquid cloud droplets only. The percentage of those supercooled layers that form ice at a specific CTT is frequently used to characterize ice nucleation in models or observations (e.g., Kanitz et al., 2011; Seifert et al., 2010; Seifert et al., 2015; McCoy et al., 2015; Alexander and Protat, 2018; Villanueva et al., 2021). This fraction of ice-containing clouds is considered typical for certain geographical regions.

Once ice is nucleated in a supercooled cloud, the three-phase system of vapor, liquid, and ice is thermodynamically unstable (Korolev, 2007). The water-vapor saturation pressure over ice $e_{\mathrm{i,s}}$ is smaller than that over water ($e_{\mathrm{l,s}}$), thus the ratio of saturation pressures $\phi = e_{\mathrm{l,s}}/e_{\mathrm{i,s}}$ is larger than 1. When the saturation pressure of an air parcel e is larger than the saturation pressure, this parcel is supersaturated:

$$S = \frac{e - e_\mathrm{s}}{e_\mathrm{s}}, \tag{2.4}$$

where supersaturations for ice and liquid are defined as S_i and S_l, respectively. In the case of $e_{\mathrm{i,s}} < e < e_{\mathrm{l,s}}$, an air parcel can be supersaturated with respect to ice and subsaturated with respect to liquid water. Under mixed-phase conditions, the difference in saturation pressures causes a mass transfer from the liquid droplets via the vapor phase to the ice phase. The ice phase will grow at expense of the liquid phase, which is also called Wegener-Bergeron-Findeisen process (WBF). If no source of water vapor is available, the droplets will dissolve, leaving a glaciated cloud consisting only of ice crystals. However, depending on the actual supersaturation, the ice crystals might not be able to consume all the excess water vapor, supporting the mixed-phase state for long time. In the following, this mass transfer is analyzed analytically, in order to estimate the preconditions for glaciation of a cloud and to quantify the time scales.

The change of supersaturation over liquid water S_l in a vertically moving, adiabatic mixed-phase parcel is given as (Korolev and Mazin, 2003; Korolev et al., 2017):

$$\frac{1}{S_\mathrm{l}+1}\frac{\mathrm{d}S_\mathrm{l}}{\mathrm{d}t} = a_0 w - a_2 B_\mathrm{i}^* N_\mathrm{i} \bar{r}_\mathrm{i} + \left(a_1 B_\mathrm{l} N_\mathrm{l} \bar{r}_\mathrm{l} + a_2 B_\mathrm{i} N_\mathrm{i} \bar{r}_\mathrm{i}\right) S_\mathrm{l}, \tag{2.5}$$

where a_0, a_1, a_2, B_i^*, B_i, and B_l are the constants given in the original publication (where w is used as a subscript for liquid droplets instead of l) and in appendix A. They scale the mass fluxes between the three phases and depend on temperature and pressure. Here, w is the vertical velocity (positive for upward motion), $\bar{r}_\mathrm{l}$ and $\bar{r}_\mathrm{i}$ are the average radii of the liquid and ice particles, respectively. From Eq. (2.5) a limiting supersaturation can be obtained, assuming no growth of the cloud particles:

$$S_{\mathrm{qs,l}} = \frac{a_0 w - b_\mathrm{i}^* N_\mathrm{i} \bar{r}_\mathrm{i}}{b_\mathrm{l} N_\mathrm{l} \bar{r}_\mathrm{l} + b_\mathrm{i} N_\mathrm{i} \bar{r}_\mathrm{i}}. \tag{2.6}$$

Following Korolev and Mazin (2003), the quantity $S_{\mathrm{qs,l}}$ is called quasi-steady supersaturation. Again, $b_\mathrm{l} = a_1 B_\mathrm{l}$, $b_\mathrm{i} = a_2 B_\mathrm{i}$, and $b_\mathrm{i}^* = a_2 B_\mathrm{i}^*$ are given in the original publication and in appendix A. The limiting supersaturation can also be interpreted as an equilibrium state, where changes in the supersaturation are balanced by the cloud particles. In case $S_{\mathrm{qs,l}} \geq S_\mathrm{l}$, both phases ice and liquid water might grow, which will be discussed in further detail later in this section. The phase relaxation time τ_p gives the time scale necessary until this quasi-steady supersaturation is reached:

$$\tau_p = \frac{1}{a_0 w + b_\mathrm{l} N_\mathrm{l} \bar{r}_\mathrm{l} + (b_\mathrm{i}^* + b_\mathrm{i}) N_\mathrm{i} \bar{r}_\mathrm{i}} \approx \frac{1}{{\tau_{\mathrm{p,l}}}^{-1} + {\tau_{\mathrm{p,i}}}^{-1}}, \tag{2.7}$$

where $\tau_{\mathrm{p,l}}$ and $\tau_{\mathrm{p,i}}$ are the relaxation times for liquid water and ice, respectively. In typical stratiform mixed-phase clouds, liquid droplets control the phase relaxation, with times on the order of 0.1 to 10 s (Korolev and Mazin, 2003). In the absence of updrafts, $S_{\mathrm{qs,l}}$ is always negative, but the evaporating droplets keep the the saturation over water close to 1. Typical N_l in mixed-phase clouds are $10^5\,\mathrm{L}^{-1}$, with $\bar{r}_\mathrm{l}$ of 5 to 10 μm. Ice particles are usually less abundant with N_i of 0.1 to $100\,\mathrm{L}^{-1}$, but larger sizes of 50 to 1000 μm.

The time τ_g until full glaciation without additional ice nucleation is (Pinsky et al., 2014):

$$\tau_\mathrm{g} = \frac{3}{2(\phi-1)} \left\{ \frac{1}{\Upsilon_\mathrm{i} B_\mathrm{i} {N_\mathrm{i}}^{2/3}} \left[\left(q_{\mathrm{i},0} + \frac{a_1}{a_2} q_{\mathrm{l},0} + \frac{a_0}{a_2} w \tau_\mathrm{g} \right)^{2/3} - {q_{\mathrm{i},0}}^{2/3} \right] + \frac{\phi}{\Upsilon_\mathrm{l} B_\mathrm{l} {N_\mathrm{l}}^{2/3} {q_{\mathrm{l},0}}^{2/3}} \right\}, \tag{2.8}$$

with the initial liquid-water and ice-water mixing ratios $q_{\mathrm{l},0}$ and $q_{\mathrm{i},0}$, respectively. The products $N_\mathrm{l}\bar{r}_\mathrm{l}$ and $N_\mathrm{i}\bar{r}_\mathrm{i}$ are the integral radii of water and ice, respectively. With the typical values given above, the integral radius for droplets is 500 to 1000 m^{-2} and for ice 0.005 to 100 m^{-2}. The vertical velocity w has to be assumed constant, when deriving Eq. (2.8). Υ_l and Υ_i are prefactors to harmonize the definitions of Pinsky et al. (2014) with Korolev and Mazin (2003) and Korolev and Field (2008).

Now, Eq. (2.8) will be used to discuss the impact of N_i, $q_{\mathrm{l},0}$, and w on the glaciation time. For the moment, any shape effects that would support enhanced growth are neglected (i.e., all particles are assumed spherical). At first, the case of $w = 0$ is discussed. Under this condition, Eq. (2.8) is in good agreement with Eq. (29) by Korolev and Mazin (2003). With vertical motions being absent, glaciation time mainly depends on $q_{\mathrm{l},0}$ and N_i and is on the order of 10^2 to 10^5 seconds (Korolev and Mazin, 2003). For constant $q_{\mathrm{l},0}$ across all temperatures, as shown by (Korolev and Mazin, 2003), a minimum τ_g is reached at about −15 °C, where ϕ is highest. Fig. 2.1 shows the glaciation time for typical $q_{\mathrm{l},0}$ and $q_{\mathrm{i},0}$ as reported by Bühl et al. (2016). Different to the the glaciation time for a fixed $q_{\mathrm{l},0}$, the temperature dependence is lessened. However, for low temperatures, more INP are active, hence higher N_i are usually observed. It becomes clear that a reduction of INP in pristine environments causes a prolonged glaciation time. A factor of 2 lower number of INP at, e.g., −20 °C increases the glaciation time by a factor of ~ 1.6. Droplet number concentration has a negligible effect on this consideration. Only for $N_\mathrm{l} < 100\,\mathrm{cm}^{-3}$, the glaciation time is underestimated by 5%–10% (Pinsky et al., 2014).

When up- or downdrafts are present, they can serve as an additional source or sink for supersaturation (see first term at right-hand side of Eq. (2.5)). Following up on Korolev and Mazin (2003), Korolev (2008) identified four regimes of mass transfer between the three phases, depending on vertical velocity. The regimes are separated by the threshold velocities w^0, w^+, and w^*:

$$w^0 = \frac{e_{\mathrm{i,s}} - e_{\mathrm{l,s}}}{e_{\mathrm{l,s}}} \frac{a_1}{a_0} B_\mathrm{l} N_\mathrm{l} \bar{r}_\mathrm{l}, \tag{2.9}$$

$$w^+ = \frac{(\phi-1)\,(B_\mathrm{l} b_\mathrm{i} - b_\mathrm{l} B_\mathrm{i})\, N_\mathrm{l}\bar{r}_\mathrm{l} N_\mathrm{i}\bar{r}_\mathrm{l}}{a_0 \phi\,(B_\mathrm{l} N_\mathrm{l}\bar{r}_\mathrm{l} + B_\mathrm{i} N_\mathrm{i}\bar{r}_\mathrm{i})}, \tag{2.10}$$

$$w^* = (\phi-1)\,\frac{a_2}{a_0} B_{\mathrm{i}0} N_\mathrm{i} \bar{r}_\mathrm{i}. \tag{2.11}$$

For a vertical velocity $w < w^0$, droplets and ice crystals evaporate, whereas for $w > w^*$ both phases can grow. Strictly, the WBF process is only possible for $w^0 < w < w^*$, where ice grows and droplets shrink. However, this regime is separated by w^+, where

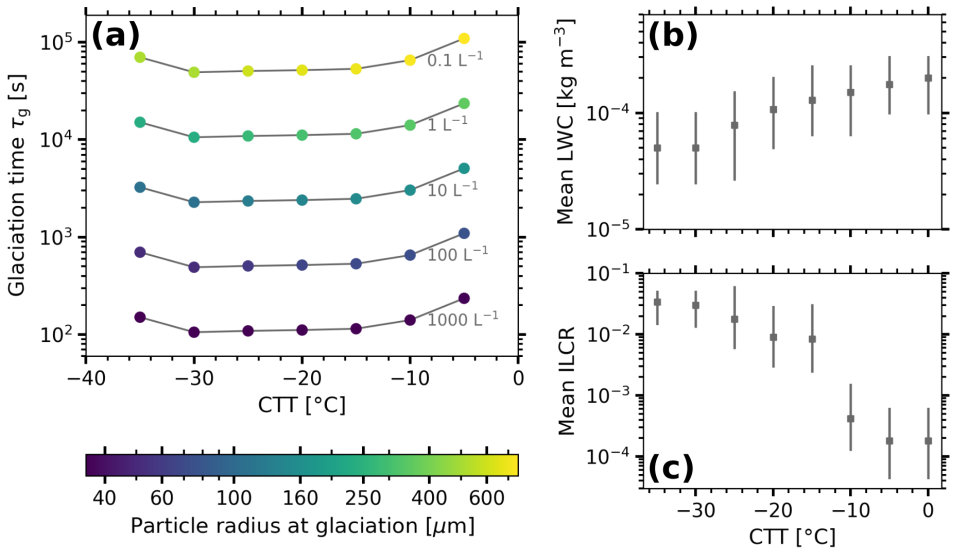

Figure 2.1: Glaciation time under the absence of vertical motion for typical mixed-phase clouds. (a) Glaciation time depending on temperature and ice particle number concentration. Typical values of LWC and ILCR are taken from Bühl et al. (2016) and are shown in (b) and (c), respectively. The color in (a) shows the hypothetical radius of the ice spheres at glaciation. Calculations are for a pressure of 750 hPa.

the water-vapor mixing ratio is in equilibrium. Below w^+, the water-vapor mixing ratio increases and above, it decreases over time. The relationship between N_i, $\bar{r}_\mathrm{i}$, and w^* is illustrated in Fig. 2.2. For increasing N_i and $\bar{r}_\mathrm{i}$, the vertical velocity required for supersaturation over liquid water also increases. Under typical conditions, w^* is on the order of a few $\mathrm{cm\,s^{-1}}$ to $\mathrm{m\,s^{-1}}$ of upward velocity, whereas the evaporation of both phases ($w < w^0$) requires downdrafts of more than $1\,\mathrm{m\,s^{-1}}$. To actually reach saturation over water in an adiabatic ascend, a certain vertical displacement ΔZ is required,

$$\Delta Z = \frac{1}{a_0} \ln\left(\frac{e_{\mathrm{l,s}}}{e_{l,0}}\right), \tag{2.12}$$

where $e_{l,0}$ is the water-vapor pressure at the start of the vertical displacement. The vertical displacement and the threshold velocity together provide a necessary and sufficient criterion for liquid-water saturation under the presence of ice particles (Korolev and Field, 2008).

Eq. (2.8) also can be used to obtain the glaciation time in the presence of vertical motion. For $w \neq 0$, τ_g appears on both sides of Eq. (2.8). The equation can be transformed into a quadratic equation and solved for τ_g. Fig. 2.3 shows the glaciation time dependence on w for a variety of possible N_i. In the presence of downward motion, glaciation is accelerated, leading to glaciation times of less than a few minutes. Under the influence of updrafts, the glaciation time strongly depends on N_i. For low ICNC or weak updrafts, no glaciation will occur for reasonable vertical displacements at all.

Korolev and Field (2008) showed that also cyclic vertical motions exceeding a threshold vertical displacement and vertical velocity can sustain liquid water. However, also turbulent up- and downdrafts are able to sustain a mixed-phase cloud, as long as the

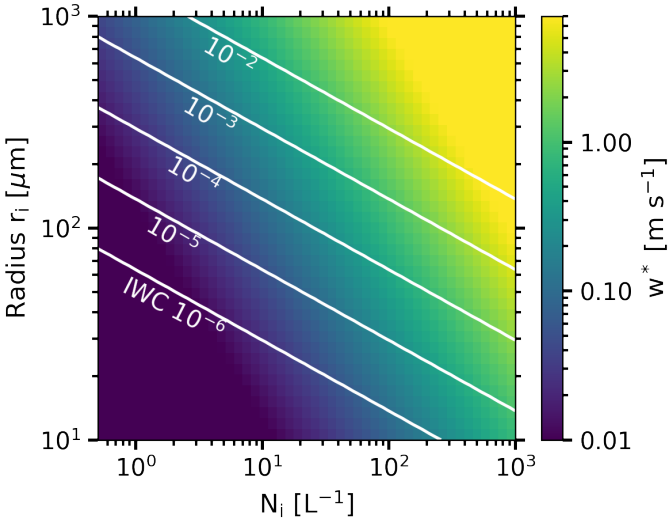

Figure 2.2: Vertical velocity w^* required for reaching liquid-water saturation under the presence of ice crystals. The white contour lines indicate the resulting q_i. Calculations are for a temperature of $-15\,°C$ and a pressure of 750 hPa.

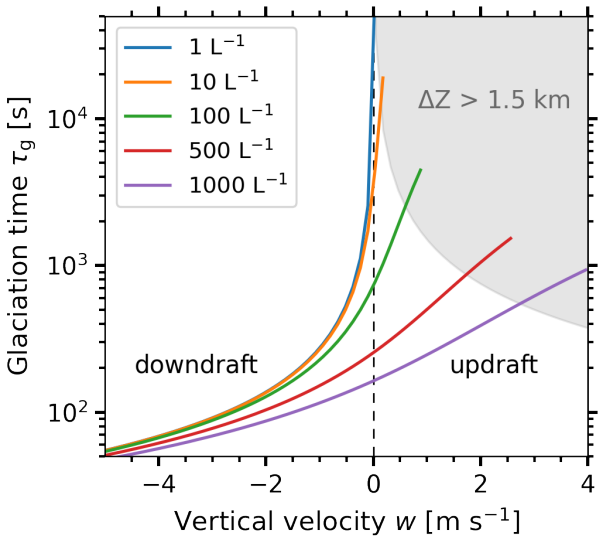

Figure 2.3: Glaciation time dependence on vertical velocity for an initial $q_l = 0.2\,g\,m^{-3}$, $q_i = 10^{-4}\,g\,m^{-3}$, $N_l = 10^8\,m^{-3}$, $T = -15\,°C$, and $p = 750$ hPa. Assumed is a constant vertical velocity. Areas that would require a vertical displacement larger 1.5 km are depicted grey.

the vertical displacement is large enough (Field et al., 2014). In idealized model simulations, a quasi-steady state can be reached for a wide variety of N_i, with average ice and liquid contents staying constant (Korolev and Isaac, 2003).

Now, the growth of individual ice particles is analyzed in more detail. The theoretical framework by Chen and Lamb (1994) is used, which allows the shape of a crystal to evolve freely, only depending on temperature. This approach is also called mass distribution hypothesis. The mass growth m_i of an individual ice particle due to deposition of water vapor is (Fukuta and Walter, 1970):

$$\frac{\mathrm{d}m_\mathrm{i}}{\mathrm{d}t} = 4\pi\rho_\mathrm{i}C_\mathrm{i}A_\mathrm{i}(\phi - 1), \tag{2.13}$$

where it is assumed that the supersaturation over ice is given by the saturation pressure over water, as typical for mixed-phase clouds. ρ_i is the density of ice and A_i is the deposition growth coefficient (given in Korolev and Mazin, 2003, and in appendix A). In the deposition growth factor, the effects of mass and heat transfer are combined. The capacitance C_i depends on the size and shape of the ice crystal. When the ice crystal is considered a spheroid, C_i depends on the major and minor semi axis r_a and r_c, respectively. Formulas are given in appendix A. The growth rates along the major and minor axis are controlled by the inherent growth ratio $\Gamma(T)$,

$$\frac{\mathrm{d}\ln r_\mathrm{c}}{\mathrm{d}\ln r_\mathrm{a}} = \Gamma(T). \tag{2.14}$$

This temperature-dependent inherent growth ratio is inferred from laboratory observations. Furthermore, a reduced density is used to relate the change in mass to the change in volume. Fig. 2.4 illustrates the growth of initially spherical particles by water-vapor deposition at different temperatures. Rapid growth can be seen at temperatures of -23, -15, and $-6\,^\circ$C, where also the deviation from the spherical shape is strongest. In the region of fastest growth around $-15\,^\circ$C, the mass of the particles is almost an order of magnitude larger for non-spherical shapes. Similar results were obtained by Fukuta and Takahashi (1999) using wind tunnel studies. In agreement to their studies, the mass of a single particle is between 10^{-6} and 10^{-5} g after 20 minutes. For growth times of less than ~ 20 minutes or fall distances of ~ 350 m, Fukuta and Takahashi (1999) found no influence of riming or aggregation. As the deposition growth, the terminal velocity depends on the particle habit and size (Heymsfield and Westbrook, 2010), but a typical terminal velocity after 20 minutes of growth is $0.7\,\mathrm{m\,s^{-1}}$. Using polarimetric cloud observations, Myagkov et al. (2016b) could confirm the pristine shape of particles for shallow stratiform clouds in the temperature range of -3 to $-24\,^\circ$C.

Sulia and Harrington (2011) used a parcel model based on the mass distribution hypothesis to investigate the impact of non-spherical ice particles on glaciation time. They found that the glaciation time is reduced for temperatures of strong shape-dependent growth. For N_i less than $100\,\mathrm{L^{-1}}$, glaciation is more than a factor of 3 faster at temperatures around $-15\,^\circ$C. Also initially smaller particles show a faster

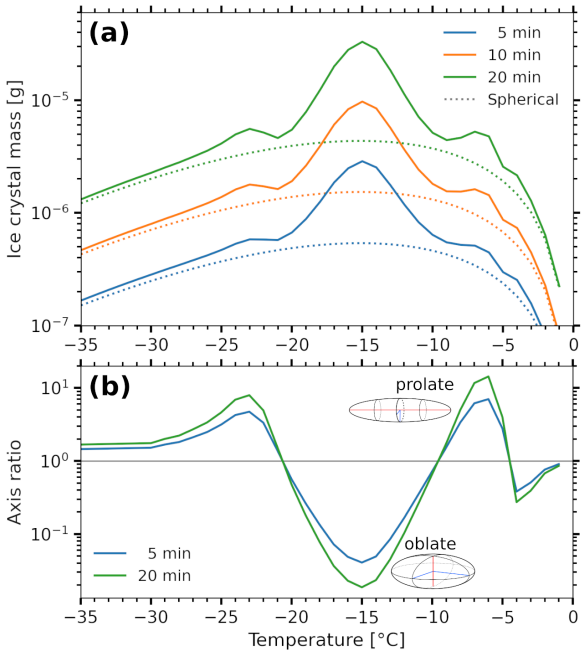

Figure 2.4: Habit evolving growth of ice crystals of different initial shape by water-vapor deposition. (a) Mass after growth times of 5, 10, and 20 minutes. Dotted lines indicate the mass for spherical growth. (b) Axis ratio of the evolved spheroid. Initially the ice particles are spheres of $r_\mathrm{i} = 6\,\mu$m.

glaciation time than larger particles, indicating a weak influence of droplet size on glaciation time as well.

With growth, the terminal velocity of the ice particle increases and it will start to sediment out of the mixed-phase cloud top (Mitchell, 1996). If sedimentation is rapid, significant portions of the condensed water will be removed from the cloud. Hence, if no moisture is supplied, the cloud will dissolve once the liquid water is depleted. A first indicator of how sensitive a cloud is to changes in the ice phase is the ice-to-liquid content ratio (ILCR). The lower this ratio, the less susceptible the cloud is to the ice phase and changes in the ICNC. Observations in shallow stratiform clouds by Bühl et al. (2016) showed a two orders of magnitude decrease of ILCR between temperatures of -35 and $-5\,^\circ$C. Alternative measure for the importance of the ice phase is the static lifetime index, for which the ice flux at cloud base is related to the liquid-water path. The index describes the time after which, under the absence of large-scale vertical motion, the liquid phase would be depleted from the cloud. In the same 30 K interval as above, this lifetime increases from minutes to days (Bühl et al., 2016). Hence, the effect of a pristine environment is likely to be most pronounced for clouds with rather high ILCR, i.e., temperature below about $-15\,^\circ$C.

All the described processes are entangled and it is tough to single them out in real clouds. A strongly simplified back-of-the-envelope calculation shall illustrate this again. At $-20\,^\circ$C, a mixed-phase layer might contain $7\,\mathrm{L}^{-1}$ ice crystals and a liquid-water content (LWC) of $0.1\,\mathrm{g\,m}^{-3}$, yielding a glaciation time of $\sim 1.4\,$h. In this case, an updraft of less than $10\,\mathrm{cm\,s}^{-1}$ is sufficient to bring the cloud parcel to supersaturation over liquid water. Under a persistent updraft, the glaciation time increases by more

than an order of magnitude. But also instantly, the cooling will nucleate new ice particles. A temperature decrease of just 2 K will almost double the number of ice crystals. A doubled number of ice crystals, in turn, will reduce the glaciation time by almost a factor of two. Hence, the analysis based on the theoretical framework presented above can only provide a first insight into the complex interactions occurring in mixed-phase clouds. To isolate the aerosol effect on primary ice formation, it is pivotal to constrain the analysis to shallow clouds with thin liquid layers. This condition excludes riming, aggregation, and secondary ice formation. Then, detailed remote-sensing observations can provide the required information of aerosol load, ice and liquid water mass, and vertical motions. These constraints will finally help to better characterize microphysical processes in shallow clouds directly in the atmosphere.

The following chapter will introduce the mobile ground-based remote-sensing facility used to collect the dataset and the locations of the field deployments. Afterwards, the data analysis methods are presented. The contrasts of aerosol and cloud properties are then discussed in Chapters 5 to 7.

3 The mobile ground-based remote-sensing facility LACROS

3.1 LACROS instruments

The core facility used in this study is the mobile Leipzig Aerosol and Cloud Remote Observations System (LACROS) of the Leibniz Institute for Tropospheric Research (TROPOS) with state-of-the-art instrumentation for synergistic observations of aerosol, clouds, dynamics, radiation, and precipitation. Having been established in 2011 (Bühl et al., 2013b), LACROS was continuously expanded and currently consists of the following instruments:

- **METEK MIRA-35**, a 35 GHz scanning cloud radar with slanted linear depolarization configuration;
- **Polly$^{\mathbf{XT}}$**, a multi-wavelength Raman and polarization lidar;
- **RPG HATPRO G2**, a 14-channel microwave radiometer (MWR);
- **HALO Photonics StreamLine XR**, a 1.5 μm scanning Doppler lidar;
- **METEK Micro Rain Radar**, a vertically pointing 24 GHz radar (since May 2018);
- **Jenoptik CHM15kx**, a 1064 nm ceilometer;
- **Ott Parsivel^2**, an optical disdrometer;
- **Radiation sensors**, namely a Cimel sun and sky photometer and sensors for broadband irradiation measurements.

An overview of technical specifications is provided in Tab. 3.1. All the instruments are housed in two custom-built, standard-size 20 ft shipping containers (Fig. 3.1). This allows mobility and standardized, hence cost-efficient, logistics. Once on site, a team of 3–4 persons needs two days for the deployment and another three days for quality assurance and setup of the data streams. Afterwards, a single person is sufficient to operate LACROS and maintain the instruments, while the instruments collect the data autonomously. For dedicated deployments additional instrumentation from partner institutions might be added.

Apart of the instruments, automated data processing and synergistic retrieval are a crucial component of LACROS. The data processing is described in Chapter 4 in more detail. The remainder of this chapter briefly describes the key instruments used during this study and the locations LACROS was deployed at.

Table 3.1: Specifications of the LACROS instruments and measured quantities used in this study.

Instrument (Reference)	**Frequency ν Wavelength λ**	**Measured quantities used in this study**	**Temporal resolution**	**Vertical range**	**Vertical resolution**
Doppler cloud radar METEK MIRA-35 (Görsdorf et al., 2015)	$\nu = 35\,\mathrm{GHz}$	Radar reflectivity factor	2–10 s	150–13000 m	30 m
		Line-of-sight velocity	2–10 s	150–13000 m	30 m
		Linear depolarization ratio	2–10 s	150–13000 m	30 m
Raman polarization lidar Polly^{XT} (Engelmann et al., 2016)	$\lambda = 355, 532, 1064\,\mathrm{nm}$	Attenuated backscatter coeff.	30 s	100–15000 m	7.5 m
	$\lambda = 355, 532\,\mathrm{nm}$	Raman backscatter signal	1 h	300–5000 m	$\sim$ 50 m
	$\lambda = 355, 532\,\mathrm{nm}$	Linear depolarization ratio	30 s	100–15000 m	7.5 m
Microwave radiometer RPG HATPRO G2 (Rose et al., 2005)	$\nu = 22.24$–$31.4\,\mathrm{GHz}$	Brightness temperatures	1 s	column integral	
	$\nu = 51.0$–$58.0\,\mathrm{GHz}$	Brightness temperatures	1 s	column integral	
Doppler Lidar HALO Photonics StreamLine XR (Pearson et al., 2009)	$\lambda = 1.5\,\mu\mathrm{m}$	Attenuated backscatter coeff.	2 s	48–12000 m	48 m
		Line-of-sight velocity	2 s	48–12000 m	48 m
Ceilometer Jenoptik CHM15kx	$\lambda = 1064\,\mathrm{nm}$	Attenuated backscatter coeff.	30 s	15–15300 m	15 m
Optical disdrometer Ott Parsivel^2 (Löffler-Mang and Joss, 2000)	$\lambda = 650\,\mathrm{nm}$	Hydrometeor size distribution	30 s	4 m	-
Sun and sky photometer Cimel CE318-T (Barreto et al., 2016)	$\lambda = 340$–$1640\,\mathrm{nm}$	Aerosol optical thickness	variable	column integral	

Figure 3.1: The mobile facility LACROS deployed at the campus of the University of Magallanes at Punta Arenas, Chile.

Table 3.2: MIRA-35 cloud radar settings of the long-term vertical-stare observations. The abbreviations are: pulse repetition frequency (PRF), number of points in the Fast Fourier Transform (NFFT), number of averaged spectra (n_{avg}), and Nyquist velocity (v_{Nyquist}).

Start date	PRF [Hz]	NFFT	n_{avg}	v_{Nyquist} [m s^{-1}]
2011-08-03	5000	256	200	10.56
2016-07-13	5000	1024	10	10.56
2016-08-25	5000	512	10	10.56
2016-09-13	7500	512	15	15.83
2017-03-16	3750	512	15	7.91
2019-01-11	5000	512	20	10.56

3.1.1 MIRA-35 cloud radar

The central instrument of LACROS is a METEK MIRA-35 cloud radar, which is a magnetron-based pulsed 35 GHz coherent-on-receive cloud radar with polarization and Doppler capabilities (Görsdorf et al., 2015). At a wavelength of 8.5 mm, the radar is well suited for the observation of hydrometeors with sizes commonly found in clouds. A 208 ns pulse length combined with oversampling provides a vertical resolution of 31.2 m. The transmitter, data acquisition, and the parabolic dish are mounted on a zenith and azimuth scanner. An antenna diameter of 1.2 m generates a pencil-beam with a 6 dB beamwidth of 0.5°. Most of the time vertical-stare observations are performed. Range-height-indicator (RHI) and plan-position-indicator (PPI) scans are done once per hour from minute 29 to 35, though they are not further investigated in this work. The original horizontal/vertical depolarization configuration was changed to a slanted linear depolarization basis in March 2016 (Myagkov et al., 2016a). Depolarization channel decoupling in terms of integrated cross-polarization ratio (ICPR) was found to be as low as −31 dB (Myagkov et al., 2015).

By default, MIRA-35 provides noised-cleaned compressed Doppler spectra (zspc-format) and moment data separately for meteorological targets and atmospheric plankton (Görsdorf et al., 2015). Over the years covered by this work, the default settings of

MIRA-35 were modified several times, mostly to improve the usability of the Doppler spectra. An overview of the settings is given in Tab. 3.2. With these settings a detection threshold of better than −45 dBZ at 5000 m can be achieved. The cloud radar signal processing is covered in more detail in Sec. 4.3.

3.1.2 Polly^{XT} multi-wavelength lidar

The main instrument for the measurement of aerosol properties and cloud droplets is the multi-wavelength Raman and polarization lidar Polly^{XT}. The technical setup is only briefly described here, detailed information is provided by Althausen et al. (2009) and Engelmann et al. (2016). A frequency-doubled and tripled Nd:YAG laser emits pulses of light at 355, 532, and 1064 nm at a repetition rate of 20 Hz. The light scattered back from atmospheric targets is collected by three telescopes with different fields of view and directed to 13 detection channels depending on wavelength and polarization state. Detection is done using a 500 MHz photon counting system and a spatio-temporal resolution of 7.5 m (50 ns) and 30 s (600 pulses). As the whole optical setup of Polly^{XT} is pointing at $\theta = 5°$ off-zenith to prevent the detection of specular reflection from ice crystals (Westbrook and Illingworth, 2011), the measured range r needs to be converted to height h using the relationship $h = \cos(\theta)\, r$. The far-range telescope achieves a full overlap with the emitted beam at roughly 800 m range. Detection channels are available for the total signal at the three emitted wavelengths, the N_2 Raman signals at 387 and 607 nm, a water-vapor Raman signal at 407 nm, and two signals for detection of cross-polarized light at 355 and 532 nm. Full overlap at the wider field of view of the near-range telescope is reached at around 250 m range. Channels are available for the total signal at 355 and 532 nm as well as for the two corresponding N_2 Raman wavelengths. In 2018, a matching cross-polarized channel at 532 nm was added to allow for novel dual-field-of-view observations of liquid droplets (Jimenez et al., 2020b).

Following the LACROS policy, Polly^{XT} is designed for continuous operation without the permanent attendance of operators on-site. Built by TROPOS the instrument deployed as part of LACROS is one of more than ten in the emerging network of PollyNET (Baars et al., 2016). The data processing is described in Sec. 4.2. Only after mid of 2016, a dedicated Polly^{XT} system was incorporated into LACROS. Before, the Polly^{XT} instruments 'IfT' and 'Arielle' were co-located to LACROS temporally (Fig. 3.2). Engelmann et al. (2016) provide an overview on the characteristics of each instrument. Profiles of optical parameters are analyzed with the automated PollyNET processing chain (see Sec. 4.2), which also harmonizes the observations from different Polly^{XT} instruments.

3.1.3 StreamLine XR Doppler lidar

A HALO Photonics StreamLine XR 1.5 μm scanning Doppler lidar is used to obtain velocity observations along the beam line-of-sight (Pearson et al., 2009). Vertical-stare observations are only interrupted by fixed elevation scans of three minute duration

twice per hour at minutes 03 and 33. The scanning period at minute 33 is synchronized with the MIRA-35 cloud radar scanning. During the vertical-stare periods, the return from particles with negligible terminal velocity, such as aerosol particles or cloud droplets, serves as an accurate measure of vertical air velocity. The Doppler lidar was added to LACROS at the end of 2014, with continuous observations available since July 2015.

3.1.4 Additional instruments and auxillary datasets

Since the initial setup, a vertically-looking Jenoptik (now Lufft) CHM15kx ceilometer is part of LACROS. It provides continuous profiles of attenuated backscatter at a wavelength of 1064 nm. Also since the beginning, a 14-channel RPG HATPRO G2 MWR is included for observations of brightness temperatures in two frequency bands from 22.24 to 31.4 GHz and 51.0 to 58.0 GHz (Rose et al., 2005). Using statistical retrievals, the integrated water vapor (IWV), liquid-water path (LWP) as well as temperature and humidity profiles are derived (Crewell and Löhnert, 2007). The statistical retrieval is based on long-term radiosonde observations (Leipzig and Limassol) or high-resolution reanalysis data (Punta Arenas). Type and size distribution of surface precipitation are recorded with an optical disdrometer of the Parsivel^2 type at a temporal resolution of 30 s. A Cimel sun and sky photometer is also operated at Punta Arenas. The raw radiance observations are delivered to the Aerosol Robotic Network (AERONET) through AERONET-Europe, where retrievals of aerosol optical thickness (AOT) and column-integrated aerosol properties are performed.

Numerical weather prediction (NWP) model analysis data at the respective locations is used to obtain profiles of temperature, pressure, and humidity, which are required for the synergysitc retrievals. The datasets at Leipzig and Limassol use the Global Data Assimilation System analysis data set at 1° horizontal resolution (GDAS1), which is provided by the Air Resources Laboratory (ARL) of the U.S. National Weather Service's National Center for Environmental Prediction (NCEP-ARL, 2020). Since the start of the Punta Arenas campaign, the analysis of the Integrated Forecasting System (IFS) of the European Centre for Medium-Range Weather Forecast (ECMWF) is used. The analysis field from GDAS1 and GFS (NCEP, 2000) are used for the airmass transport simulations.

A pre-study on the heights and frequency of environments allowing heterogeneous ice formation is based on a long-term record of radiosonde ascends. The ascends of the stations closest to the deployment of LACROS are obtained through the Integrated Global Radiosonde Archive (IGRA) dataset (Durre et al., 2006; Durre et al., 2018).

3.2 Campaigns under study

This section briefly describes the recent LACROS campaigns at Limassol, Cyprus and Punta Arenas, Chile. Additionally, the observations at Leipzig are used for comparison. A temporal overview is given in Fig 3.2 together with some key numbers in Tab. 3.3. In the remainder of this section, each location and the associated campaign is briefly summarized.

3.2.1 CyCARE field campaign

The Cyprus Clouds, Aerosol and Rain Experiment (CyCARE) took place from October 2016 to March 2018. LACROS was deployed at the city of Limassol for the full duration (Fig. 3.3). During an intensive observation period, additional measurements were conducted at Paphos airport in the framework of the Absorbing aerosol layers in a changing climate: aging, lifetime and dynamics (A-LIFE) aircraft campaign (Weinzierl and A-LIFE Science Team, 2021). Cyprus is located in the eastern Mediterranean Sea and is frequently influenced by aerosol transport from northern Africa, the Middle East, and Europe. Typical aerosol mixtures include dust (mineral and soil), marine (sea salt and organics), as well as anthropogenic pollution (Nisantzi et al., 2015). The proximity to such a variety of aerosol sources makes Cyprus an ideal laboratory for aerosol-cloud interaction studies (e.g., Ansmann et al., 2019). Limassol is located at the southern coast of the island with the Troodos mountain range 20 km to the north.

3.2.2 DACAPO-PESO field campaign

Since November 2018, LACROS has been deployed at Punta Arenas, Chile for the DACAPO-PESO field campaign (on the date of submission of this work, the campaign was still ongoing). Being located at 53.1°S, 70.9°W, Punta Arenas is in the midst of the Southern Ocean, farther south than any other continental land mass or major island

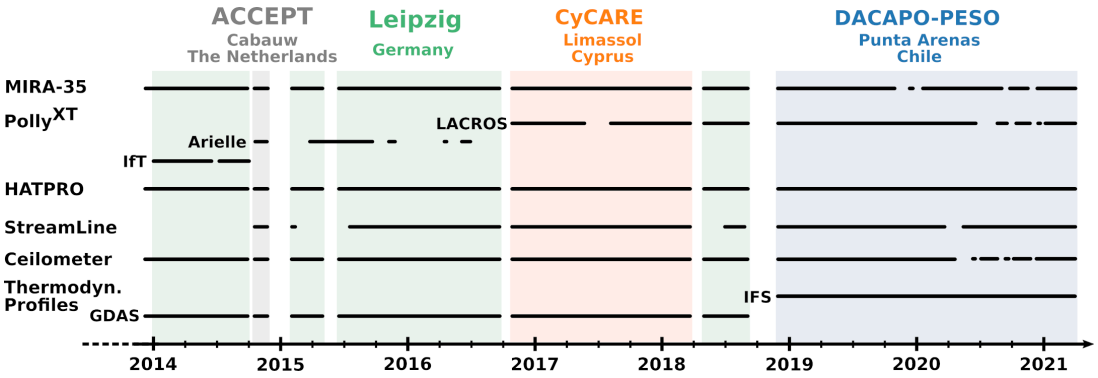

Figure 3.2: Timeline of LACROS deployments and instrument availability since 2014. Details of the three different Polly^{XT} systems named IfT, Arielle, and LACROS are provided in Engelmann et al. (2016). Data from the Analysis of the Composition of Clouds with Extended Polarization Techniques (ACCEPT) campaign (Myagkov et al., 2016a) is not used in this work.

Table 3.3: Overview on location, data availability, climate, aerosol load, and related studies for the LACROS datasets used. The altitudes are given above mean sea level (asl).

Location	Leipzig, Germany	Limassol, Cyprus	Punta Arenas, Chile
	51.4°N, 12.4°E	34.7°N, 33.0°E	53.1°S, 70.9°W
Station altitude	125 m asl	11 m asl	9 m asl
Campaign name		CyCARE	DACAPO-PESO
Duration	976 d	524 d	765 d
Cloudnet	771 d	520 d	674 d
Doppler lidar	513 d	523 d	717 d
Polly^{XT}	633 d	460 d	702 d
Climate	Northern mid-latitudes	Northern subtropics	Southern mid-latitudes
Typical aerosol load	Continental background, occasionally dust	Dust, marine, continental	Marine, occasionally continental
Related studies	Ansmann (2005) Seifert et al. (2010) Bühl et al. (2013a) Myagkov et al. (2015) Bühl et al. (2016) Radenz et al. (2021b)	Ansmann et al. (2019) Radenz et al. (2021b)	Kanitz et al. (2011) Ohneiser et al. (2020) Bromwich et al. (2020) Jimenez et al. (2020b) Floutsi et al. (2021) Radenz et al. (2021b)

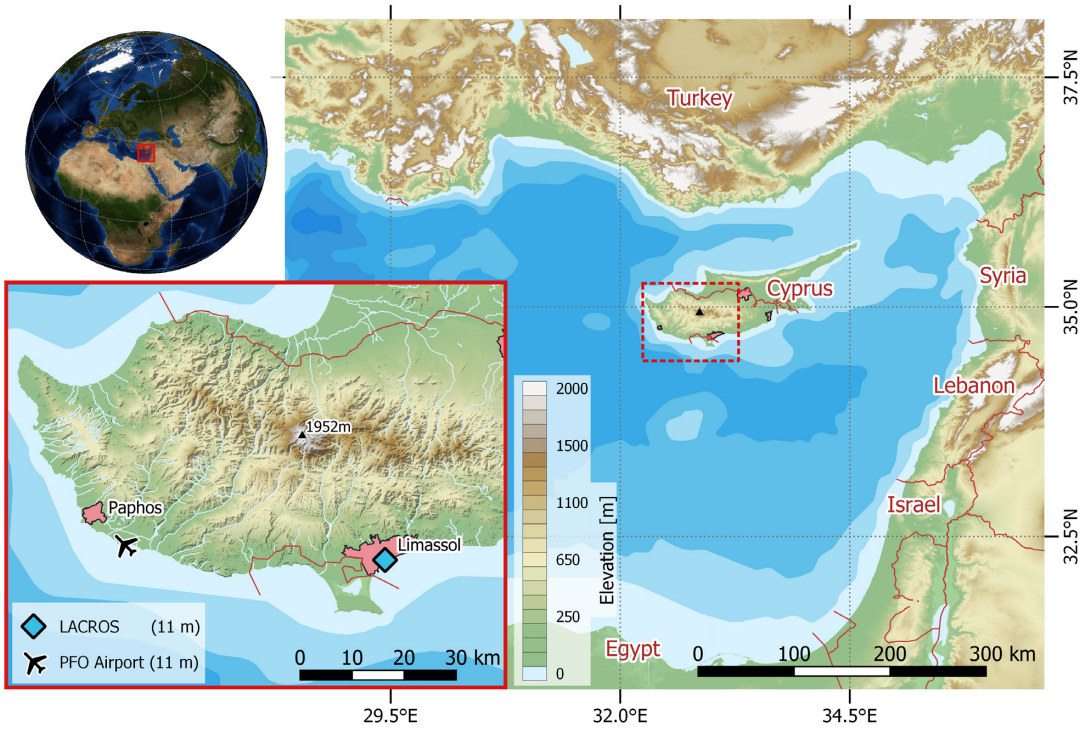

Figure 3.3: Map of the area surrounding the LACROS field site at Limassol, Cyprus.

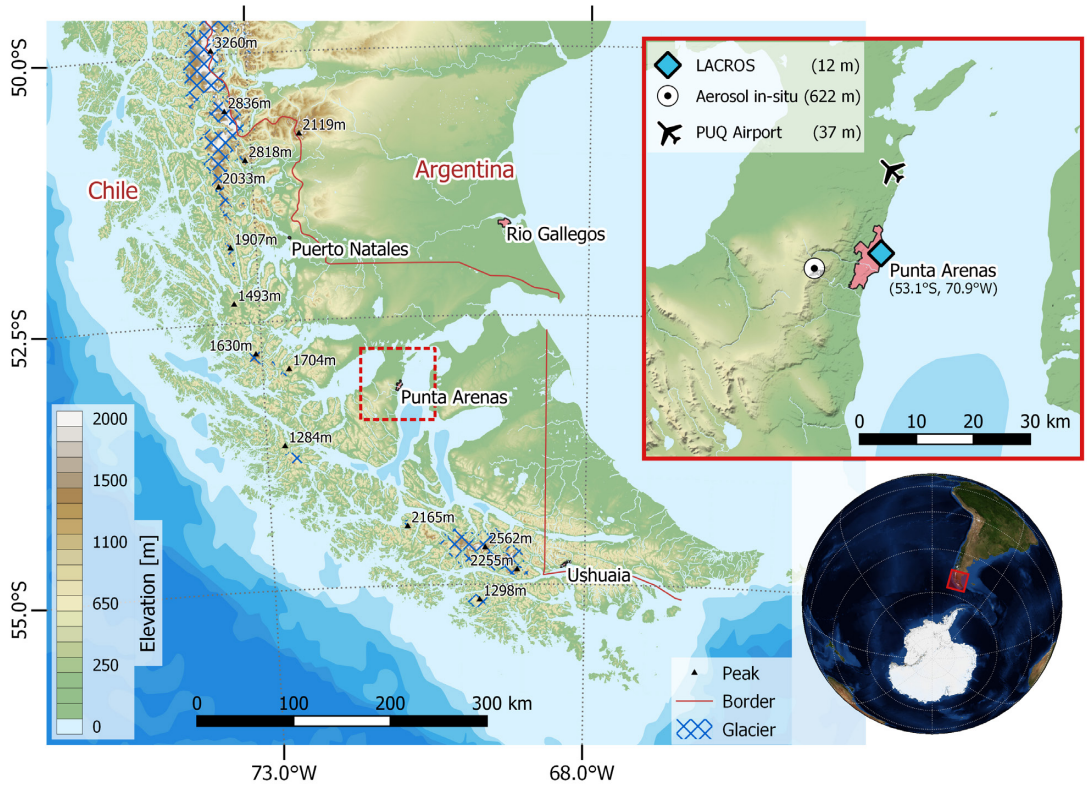

Figure 3.4: Map of the area surrounding the LACROS deployment at Punta Arenas, Chile.

apart Antarctica. Other capes only extend to 47.0°S (Steward Island, New Zealand), 43.6°S (Tasmania, Australia), and 34.8°S (Cape Agulhas, South Africa). Under the prevailing westerly flow the next land mass upwind is more than 8000 km away. Hence, the free troposphere is dominated by marine aerosol from the Southern Ocean, with almost no changes since pre-industrial times (Hamilton et al., 2014). Events of tropospheric aerosol long-range transport from Australia were seldomly observed (Foth et al., 2019; Floutsi et al., 2021). Looking at smaller scales, Punta Arenas is located next to the Magellan Strait, roughly half way between the Atlantic and Pacific Ocean (Fig. 3.4). Toward the west, the outermost foothills of the Andes reach heights of up to 1600 m, with the larger altitudes and glaciers to the north-west and south. The remote-sensing instrumentation is located at the main campus of the Universidad de Magallanes in the north-eastern part of the city. The logistical effort to bring material and personnel to Punta Arenas is relatively low. Altogether, these features make the city an ideal location for the DACAPO-PESO campaign.

Additionally to the remote-sensing instrumentation, a site with in-situ aerosol instrumentation is established on top of the Cerro Mirador at an elevation of 622 m and $\sim$ 12 km upwind of the city center (Fig. 3.4). The analysis of these measurements is still ongoing and not included into this study.

3.2.3 Observations at Leipzig

Before and between the above-mentioned campaigns, LACROS was maintained and operated at Leipzig (51.4°N, 12.4°E, Germany). Located in Central Europe, this site provides a northern mid-latitude background dataset. Aerosol conditions and cloud properties are well investigated by previous studies. Typically, the aerosol mixture is dominated by continental aerosol with anthropogenic pollution (Baars et al., 2016). Long-range transport of Saharan dust, volcanic plumes, and wildfire smoke occurs regularly (Ansmann et al., 2012; Haarig et al., 2018b; Baars et al., 2021). Detailed ground-based lidar (Seifert et al., 2010) and regional modeling studies (Weger et al., 2018) suggest dust aerosol impacts on ice formation in clouds at Leipzig. This work only includes data from 2014 onwards. Since then, the basic set of instrumentation was kept unchanged.

4 Methods and advancements in data processing

The analysis of datasets that are as extensive as the ones provided by LACROS for the three locations requires sophisticated processing tools. An overview of the layered architecture is provided in Fig. 4.1, with the developments that were conducted or led during this work highlighted.

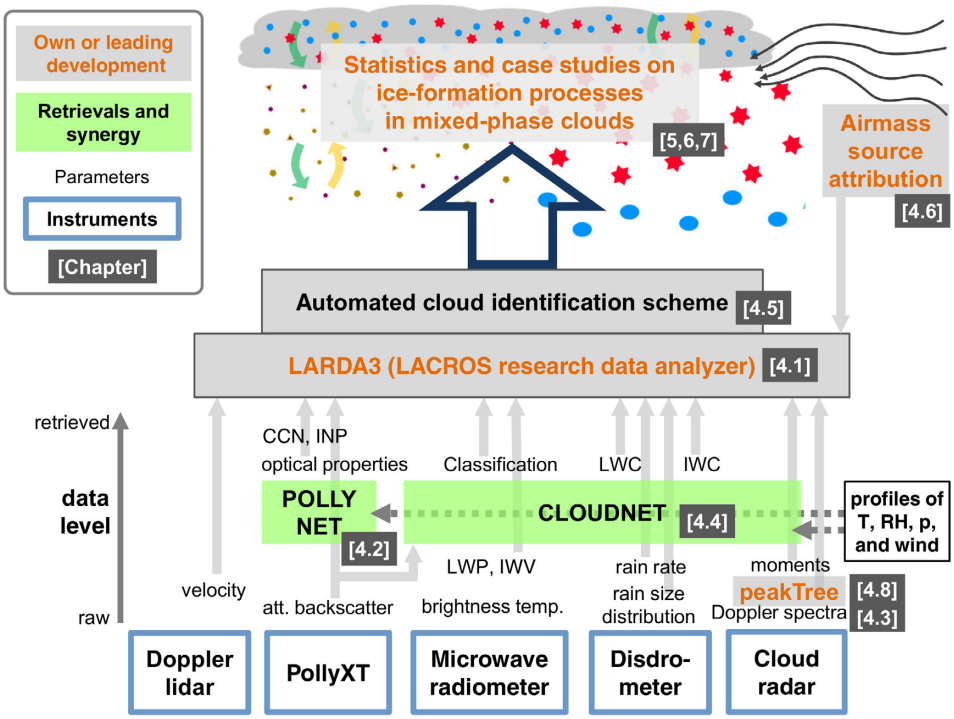

Figure 4.1: Dataflow from the LACROS instruments via the synergistic retrievals, LARDA, and the automated cloud identification to the statistics on ice formation in layered clouds.

The well-established (synergistic) Cloudnet algorithm (Sec. 4.4) and the PollyNET processing chain (Sec. 4.2) are the backbone of the data analysis. As both were just applied, they are only briefly introduced. To aid the wearisome process of airmass source interpretation for continuous profiling datasets, an automated algorithm based on residence times was developed and published (Radenz et al., 2021a). Details are described in Sec. 4.7. At the raw-data layer, a multi-peak analysis scheme for cloud radar Doppler spectra was developed and published (Radenz et al., 2019a). It is described in Sec. 4.8. The crucial link between the retrieved data and the analyzed case studies and ice formation statistics is the LACROS Research Data Application (LARDA). This in-house-developed data cube ties together all the different variables at different levels and provides easy, standardized access to the data (Sec. 4.1). Based

on LARDA, the automated cloud identification scheme connects the pixel-by-pixel Cloudnet target classification to coherent clouds and creates a database of observed cloud cases. The gravity-wave detection algorithm is also applied at this step. These two methods are part of Radenz et al. (2021b) and are presented in Sec. 4.5 and Sec. 4.6, respectively. The source code of all the developments is open source and publicly available. A list is provided in the publication record appended.

4.1 LACROS Research Data Application

The multitude of data sampled with the various sensors of LACROS together with different levels of retrieved products (140 variables across 1.4 Mio. files) requires sophisticated methods for accessing, harmonizing, processing, and interpretation of the data. The LACROS Research Data Application brings together the results of these retrieval results and allows direct access to different levels of data.

LARDA provides a generic interface implemented in the programming language 'python' for data loading, joining, slicing, analyzing, and plotting. Within this work, responsibility for development of LARDA was taken over. An existing prototype (J. Bühl, personal communication) was ported to python3, modularized, significantly extended, and published under a public license (Bühl et al., 2021). A scheme of the new architecture is provided in Fig. 4.2. Most prominently, a distributed architecture was realized, which allows the remote loading of data from a backend server and to do further processing locally. An additional web-interface (http://larda3.tropos.de) allows quick visualization of the data, without the need for preprocessed images.

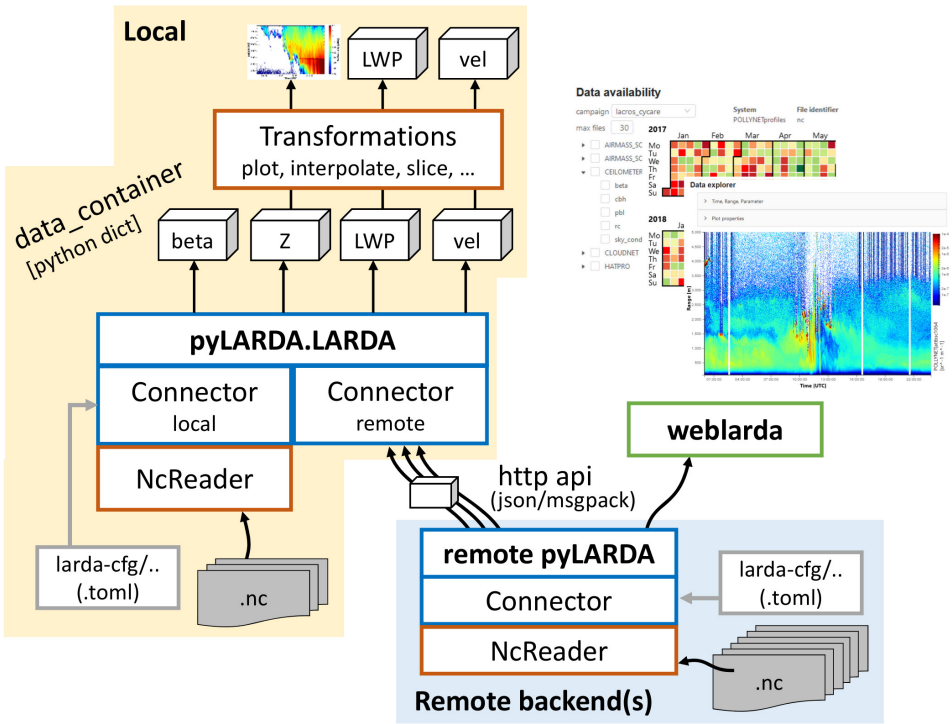

Figure 4.2: Modularized version of LARDA3 with the local and remote backend option. The web-interface accesses the same database as the remote backend.

4.2 Aerosol statistics based on the PollyNET processing chain

The observations of the Polly^{XT} lidar are used to obtain profiles of aerosol optical properties. Quantities of interest are the particle backscatter coefficient, the particle extinction coefficient, and the particle linear depolarization ratio. Based on these optical properties, microphysical properties like the INP concentration can be inferred. The automated retrieval of optical properties is done with the PollyNET processing chain (Baars et al., 2016; Baars et al., 2017; Yin and Baars, 2021). Together with the standardized setup and continuous measurements, this retrieval is one cornerstone of the PollyNET philosophy (Baars et al., 2016). Automated, continuous calibration of the lidar observations provides the basis for a plethora of products, comprising high-resolution, molecular-attenuation-corrected estimates of particle backscatter coefficients, water-vapor products, and a target classification. Using this retrieval ensures a homogenized analysis of the data from the three different Polly^{XT} instruments, which were utilized in the framework of this study (see Fig. 3.2).

The basic product is the attenuated backscatter coefficient at 355, 532, and 1064 nm at a resolution of 30 s. It is estimated by normalizing the background-, range- and dead-time-corrected lidar profiles with the lidar calibration factor, which is derived from regular Raman or Klett retrievals (Baars et al., 2016). As a second step, the attenuated backscatter coefficient is corrected for molecular backscatter and extinction as well as a first estimate of particle extinction, giving the quasi backscatter coefficient (Baars et al., 2017). For the particle extinction, a fixed lidar ratio has to be assumed. The quasi backscatter coefficient combines a first estimate of the particle backscatter coefficient with a high temporal resolution and is a suitable variable for analysis of the temporal evolution of thin aerosol layers (see the example cases in Sec. 4.7).

The long-term statistical analysis is based on the particle backscatter coefficient β_p at 532 nm wavelength, which is computed with the Klett method (Fernald, 1984) whenever conditions are suitable. Profiles of the particle linear depolarization ratio are calculated from the calibrated volume depolarization ratio (Freudenthaler, 2016) only when the ratio of molecular backscatter coefficient to β_p is below a value of 18. Additionally, any particle linear depolarization ratios larger than 0.7 are masked, as they are indications for noise artifacts in the cross-polarized signal component. All profiles are then filtered with the co-located Cloudnet target classification to exclude clouds, especially optically thin ice clouds, which are only reliably classified by cloud radar. Finally, a manual screening excludes fragments of thin liquid clouds, which would otherwise artificially increase β_p. For the averages, the optical data of each retrieved profile is binned to vertical intervals of 200 m for the height statistics or 3 K for the temperature statistics.

Next, the microphysical properties, such as concentrations of INP, are derived from the average optical properties. This is an important step to evaluate the datasets of the three sites with respect to contrasts in the potential contribution of aerosol effects on heterogeneous ice-formation efficiency. Conversion from optical properties as observed by lidar to microphysical aerosol properties is based on the parametrizations described

by Mamouri and Ansmann (2016). By means of this approach, the lidar-measured aerosol extinction coefficient is converted to the number and surface concentration N_{500} and S_{500}, respectively, of aerosol particles larger than 500 nm in diameter. These quantities are applied in available in-situ-based parametrizations for the retrieval of INP concentrations. Prerequisite for the retrieval is a correct aerosol typing, as different types of particles differ by orders of magnitude in their ice-forming efficiency. In order to do so, the average backscatter profile is separated into the categories marine, continental, and mineral dust based on airmass source (see Sec. 4.7 and Radenz et al., 2021a) and particle linear depolarization ratio (one-step POLIPHON; Mamouri and Ansmann, 2017). The average extinction is calculated from the profiles of β_{p} by assuming a typical lidar ratio of 20 sr for marine, 50 sr for continental, and 45 sr for dust aerosol (Müller et al., 2007; Baars et al., 2017; Bohlmann et al., 2018). In the next step, the extinction coefficient is converted to N_{500} and S_{500} using sun-photometer-based conversion factors (Mamouri and Ansmann, 2016). Then, the above-mentioned INP parametrizations are applied for each aerosol class, following DeMott et al. (2015) for mineral dust, DeMott et al. (2010) for continental aerosol, and McCluskey et al. (2018a) and McCluskey et al. (2018b) for marine aerosol.

4.3 Estimating moments from radar Doppler spectra

The cloud radar MIRA-35 is the core instrument of LACROS for observing clouds. As its observations are the backbone of the synergistic retrieval Cloudnet, the basic signal processing is briefly explained. The signal received by a weather or cloud radar can be expressed as (Doviak and Zrnic, 1993):

$$P(\vec{r}_0) = \int_V I(\vec{r}_0, \vec{r})\, \eta(\vec{r}) \mathrm{d}^3\vec{r}, \tag{4.1}$$

where $\vec{r}_0$ is the center of a range bin, $\eta(\vec{r})$ the volume reflectivity, and $I(\vec{r}_0, \vec{r})$ the instrument weighting function The product of the two latter is integrated over the observation volume V. The instrument weighting function depends on the antenna radiation pattern, especially the beamwidth and the characteristics of the pulse, most importantly the pulse length. Its rather complex form can be simplified under certain assumptions into the calibration constant C/r^2 (Doviak and Zrnic, 1993).

Following Atlas et al. (1973), Kneifel et al. (2011), and Radenz et al. (2018), the received power can be decomposed through the velocity-dependent Doppler spectrum $\mathcal{S}(\vec{r}_0, v)$, with the velocity v, as

$$P(\vec{r}_0) = \int \mathcal{S}(\vec{r}_0, v) dv = \iint I(\vec{r}_0, \vec{r})\, \eta'(\vec{r}, v)\, \mathrm{d}^3\vec{r}\, \mathrm{d}v, \tag{4.2}$$

where $\eta'(\vec{r}, v)$ is the spectral reflectivity.

The cloud radar samples the Doppler spectrum at discrete velocity bins determined by the number of points in the Fast Fourier Transform (NFFT). Hence, $\mathcal{S}(\vec{r}_0, v)$ at range $\vec{r}_0$ is represented as $\mathcal{S}(v_k) = \mathcal{S}_k$, where v_k is the velocity of bin k. Within this spectrum, signal caused by scattering at hydrometeors only occupies a narrow band-

width and most of the bins are noise dominated. An example of such a spectrum is shown in Fig. 4.15 and will be further discussed in Sec. 4.8. A noise level, discriminating between bins with signal and noise bins, is determined, e.g., with the method of Hildebrand and Sekhon (1974). The boundaries of a peak above the noise floor are $v_{\mathrm{k_L}}$, $v_{\mathrm{k_R}}$.

As the spectral reflectivity $\eta'(\vec{r}, v)$ is strongly wavelength dependent, it is scaled by $\frac{\lambda^4}{\pi^5|K|^2}$, with the wavelength of the radar λ and the dielectric factor $|K|^2$. The dielectric factor depends on the radar wavelength, temperature, and phase of the scatterer. With the parametrization of Ray (1972), at 35 GHz $|K|^2$ is 0.176 for ice and 0.874 for liquid water. The first moment of this spectrum is the reflectivity factor

$$Z = 10 \log_{10} \left(\frac{\lambda^4}{\pi^5 |K|^2} \sum_{k=k_\mathrm{L}}^{k_\mathrm{R}} \mathcal{S}_k \right). \tag{4.3}$$

Commonly, scattering by water droplets is assumed and the equivalent reflectivity factor Z_e is provided. However, for the sake of convenience the word 'factor' and the subscript e are frequently omitted. The second moment of the spectrum is the mean Doppler velocity $\overline{v}$, the third moment is the spectral width σ, and the skewness γ characterizes the asymmetry of the peak:

$$\overline{v} = \frac{\sum_{k=k_\mathrm{L}}^{k_\mathrm{R}} \mathcal{S}_k \, v_k}{\sum_{k=k_\mathrm{L}}^{k_\mathrm{R}} \mathcal{S}_k}, \tag{4.4}$$

$$\sigma^2 = \frac{\sum_{k=k_\mathrm{L}}^{k_\mathrm{R}} \mathcal{S}_k \, [v_k - \overline{v}]^2}{\sum_{k=k_\mathrm{L}}^{k_\mathrm{R}} \mathcal{S}_k}, \tag{4.5}$$

$$\gamma = \frac{\sum_{k=k_\mathrm{L}}^{k_\mathrm{R}} \mathcal{S}_k \, [v_k - \overline{v}]^3}{\sigma^3 \sum_{k=k_\mathrm{L}}^{k_\mathrm{R}} \mathcal{S}_k}. \tag{4.6}$$

For higher-order moments, tails of the signal on one side of the peak might cause a bias, when the other side is bound by an internal minimum. To prevent potential biases, only spectral reflectivity values $\mathcal{S}_k$ above the threshold that separate a peak from its neighbor are included for calculating moments other than Z.

The linear depolarization ratio (LDR) is calculated by using the spectral reflectivity in the cross channel $\mathcal{S}_{\mathrm{cx}\,k}$:

$$\mathrm{LDR} = 10 \log_{10} \frac{\sum_{k=k_\mathrm{L}}^{k_\mathrm{R}} \mathcal{S}_{\mathrm{cx}\,k}}{\sum_{k=k_\mathrm{L}}^{k_\mathrm{R}} \mathcal{S}_{\mathrm{co}\,k}}. \tag{4.7}$$

Generally, the lowest detectable LDR is determined by the quality of the antenna and can be characterized by the ICPR (see Sec. 3.1.1 and Myagkov et al., 2015). In the spectral LDR, this cross-talk appears as a weakened shadow of the co-channel, if the latter signal is strong enough. Further details are discussed when the multi-peak analysis algorithm ist introduced in Sec. 4.8. The synergistic retrieval Cloudnet is based on the spectral moments evaluated assuming mono-modality.

4.4 Synergistic retrieval Cloudnet

For determination of cloud macro- and microphysical properties and as a basis for the stratiform cloud identification, synergies between lidar, cloud radar, microwave radiometer, and disdrometer are utilized. State-of-the-art routines for achieving this requirement are comprised in the Cloudnet retrieval (Illingworth et al., 2007). Cloudnet re-grids the observations to a common resolution (30 s and 31.18 m, determined by the vertical resolution of MIRA-35) and provides products, such as a target classification and microphysical cloud properties. Regridding is a crucial step, as each of the instruments has different temporal and vertical resolution (Tab. 3.1). Regular PPI scans of the MIRA-35 cloud radar (hourly) and the StreamLine Doppler lidar (twice per hour) are not used within the Cloudnet processing scheme. Additionally to the PPI scan, MIRA-35 also performs an RHI scan, which is also not processed within Cloudnet. Profiles of temperature, pressure, and humidity are obtained from gridded model analysis (Sec. 3.1.4). LWP and IWV are retrieved from brightness-temperature observations of the microwave radiometer. The statistical retrieval is based on long-term radiosonde observations (Leipzig and Limassol) and high-resolution reanalysis data (Punta Arenas), as described in Sec. 3.1.4. Attenuated backscatter of the ceilometer is regularly cross-calibrated with Polly$^{\mathrm{XT}}$ using the calibrated attenuated backscatter of PollyNET (see Sec. 4.2). Usually, the ceilometer data is used in the synergistic retrieval, as the dataset is more robust and less prone to interruptions. Rare gaps in the observations are filled with the Polly$^{\mathrm{XT}}$ attenuated backscatter at 1064 nm. While the zenith-pointing observations of the ceilometer provide better spatial matching of mid- and upper-level clouds, they are sensitive to specular reflection by ice crystals (Westbrook and Illingworth, 2011).

The Cloudnet target classification product is based on a bit-wise mask, each of the five bits being based on one criterium. The different bit combinations of the mask are later converted to eleven categories for practical purposes. A detailed description is given in Hogan and O'Connor (2004). Liquid droplets are primarily identified using the lidar backscatter signal. Strong backscatter is observed at liquid-layer base, followed by a rapid decrease due to attenuation in the optically thick liquid layer. Ice

particles are basically classified whenever radar return is observed at subfreezing temperatures. When ice and supercooled water coexist, the classification scheme frequently misclassifies the target as liquid droplets. As described in the following section, such ambiguities can be addressed by considering coherent structures. Aerosol is classified, rather basically, for pixels with significant attenuated backscatter under the absence of hydrometeors. Furthermore, classification of the melting layer, insect clutter, and rain is provided.

4.5 Automated cloud identification

While the Cloudnet algorithm provides a pixel-by-pixel classification of cloud phase and microphysical properties, information on temporal coherence and cloud evolution is not readily available. Hence, an automatic reproducible filtering algorithm for the selection of targeted stratiform, supercooled cloud systems is necessary. Based on LARDA (Sec. 4.1), the approach of Bühl et al. (2016) is implemented into an automated selection algorithm. Also this implementation is publicly available (Radenz and Bühl, 2021). An example of the Cloudnet processing of measurement data and the application of the cloud selection scheme is shown in Fig. 4.3. Starting from the profile of the Cloudnet target classification mask (Hogan and O'Connor, 2004), consecutive pixels classified as containing cloud hydrometeors (liquid droplets, ice, ice and supercooled liquid) are grouped together and defined as features. In case similar types of hydrometeors were observed in matching heights, single features in neighboring timesteps are connected to coherent cloud cases. For the analysis, the cloud cases are filtered for shallow stratiform clouds, which are liquid-topped and either possess an ice virga or not (rectangles in Fig. 4.3d).

An overview of the microphysical parameters sampled for each cloud case is provided in Table 4.1. It is assumed that, if ice is formed in a liquid layer, it will also sediment out of the cloud. This assumption is required, as the signal at cloud top is dominated by the scattering from liquid droplets and Cloudnet cannot reliably classify the coexistence of ice and liquid there. To pinpoint potential effects of aerosol load on cloud microphysics, thermodynamic and dynamic influences on ice formation have to be constrained. This restriction is especially important, when comparing observations in different climate zones. Hence, it is presumed that thin stratiform clouds serve as a natural laboratory, with only a small number of physical processes being active.

The cloud cases are filtered for a length of more than 20 minutes and smooth cloud top heights (standard deviation $< 150\,\mathrm{m}$) to exclude convective clouds. Laboratory studies of Fukuta and Takahashi (1999) and the cloud radar observations by Myagkov et al. (2016a) indicate that the average thickness of the liquid dominated cloud top layer has to be less than 350 m in order to restrict the dataset to the regime of pristine ice formation and avoid strong effects of secondary ice formation. Seeding by ice clouds above is excluded by filtering liquid layers with ice pixels above the liquid cloud top. CTT is taken at the topmost pixels of the liquid-dominated layer. Only clouds with CTT between -38 and $0\,^{\circ}\mathrm{C}$ are considered in the analysis, as the focus

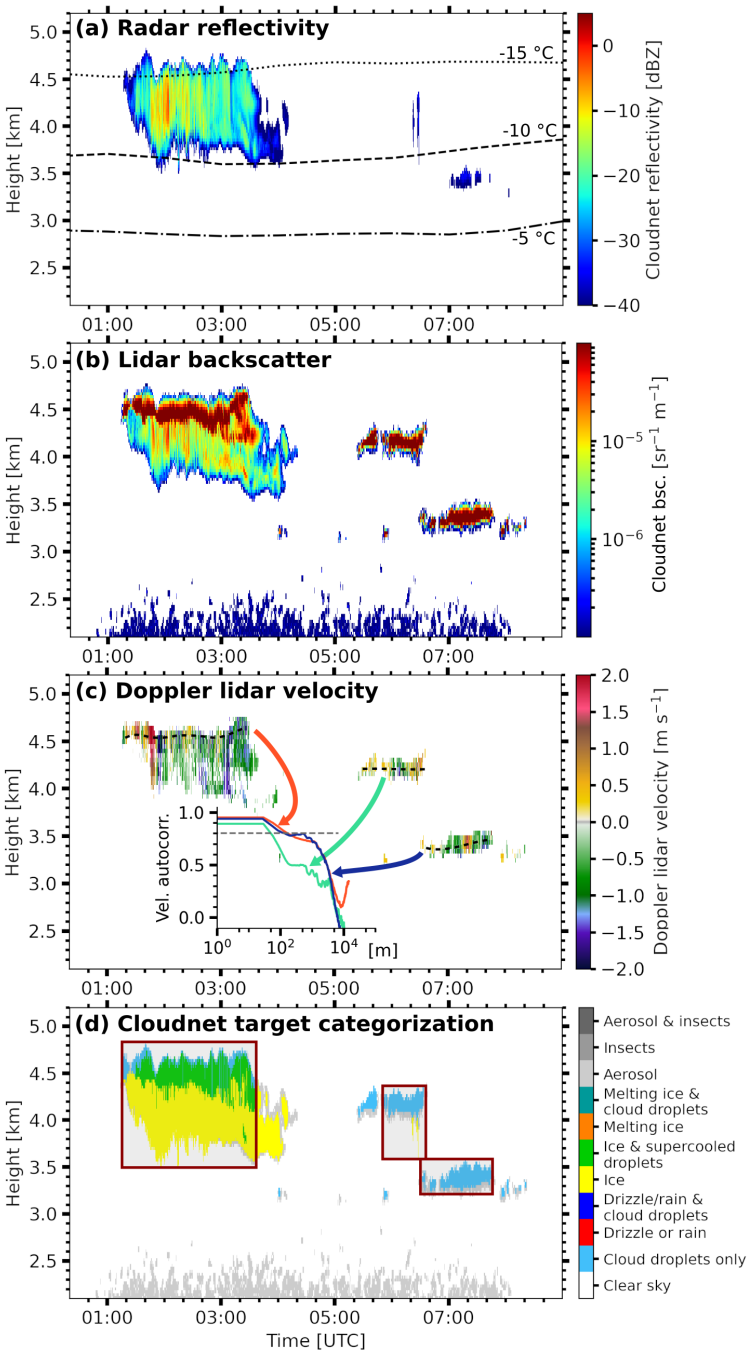

Figure 4.3: Application of Cloudnet and the automatic cloud identification scheme to the LACROS observations at Punta Arenas on 28 November 2018, 00:20–09:00 UTC. (a) Cloud radar reflectivity overlaid with the temperature, (b) lidar attenuated backscatter, (c) Doppler lidar vertical velocity, and (d) Cloudnet target categorization. Red rectangles in (d) show the detected liquid-topped shallow stratiform clouds. The inset in (c) shows the autocorrelation function of the vertical velocities in the liquid-dominated layer (heights indicated by dashed lines) of each cloud. Further details on the autocorrelation-based gravity-wave detection are provided in Sec. 4.6.

Table 4.1: Parameters sampled from the automatically identified cloud cases. A more detailed description of the automated spatio-temporal selection method is provided in Bühl et al. (2016).

Parameter	Time series	Description
Cloud top temperature	yes	Temperature of the topmost liquid pixel
Cloud top height	yes	Geometrical height of the topmost liquid pixel
Liquid-layer thickness	yes	Geometrical depth of the liquid-dominated cloud top layer
Phase classification	no	Ice pixels observed below liquid-dominated layer $> 5\%$ of duration
Cloud-base vertical velocity	yes	Doppler lidar vertical velocity at the base of the liquid-dominated layer
LWC	yes	LWC content of the liquid-dominated layer
Reflectivity in virga	yes	Radar reflectivity 180 m below the base of the liquid-dominated layer
IWC in virga	yes	Reflectivity-derived IWC 180 m below the base of the liquid-dominated layer (Hogan et al., 2006)
Extinction in virga	yes	Ice extinction 180 m below the base of the liquid-dominated layer derived from reflectivity (Hogan et al., 2006)
Ice-to-liquid content ratio	yes	Ratio of IWC in virga to LWC in liquid-dominated layer

of this study is to investigate heterogeneous ice formation. For the phase occurrence frequency statistics, a cloud is classified as ice producing, if ice pixels are observed to sediment out of the liquid-dominated layer during at least 5% of the cloud duration. On the other hand, cloud cases are classified as liquid-only, if ice pixels are observed to sediment out of the liquid-dominated layer during less than 5% of the time. The microphysical properties of the ice in the virga are taken 180 m below the liquid-dominated cloud top layer to avoid contamination by uncertainties in the liquid-base estimate and sublimation further down the virga (Bühl et al., 2016). The ice-water conent (IWC) and ice extinction coefficient are derived from the radar reflectivity and the temperatures using the retrieval by Hogan et al. (2006). With this automated cloud selection scheme, multi-year datasets can be analyzed based on objective criteria, while yielding statistics similar to manual cloud selection (e.g., Seifert et al., 2010; Kanitz et al., 2011; Seifert et al., 2015).

4.6 Gravity-wave detection

In order to enable the attribution of aerosol and dynamical effects on the phase partitioning in the stratiform cloud dataset, an approach is required to assign cloud dynamics regimes to each cloud case. Here, we focus on the temporal structure of vertical velocity to constrain the dynamics forcing on a cloud. Usually, shallow clouds are characterized by a fully developed turbulence in the liquid-dominated cloud top (Bühl et al., 2019a), where the vertical motion is driven by cloud-top cooling (e.g., Shao et

al., 1997; Fang et al., 2014; Simmel et al., 2015). In the turbulent layer at cloud top, up- and downdrafts alternate at horizontal scales on the order of 100 m or less.

However, orographic gravity waves can trigger cloud formation as well. Microphysical processes in these wave clouds are governed by large-scale dynamics, where vigorous up- and downdrafts may appear stationary. Due to this dynamics, the mixed-phase and the ice phase are horizontally separated (Fig. 4.4), with the liquid drops predominantly in the ascending branch and the ice particles in the descending branch (Heymsfield and Miloshevich, 1993; Baker and Lawson, 2006). The properties of the horizontal wind field determine the regions of the up- and downdrafts in such orographic clouds. Observations of these clouds with stationary ground-based remote sensing might thus not sample the full horizontal extent of the cloud, which causes a misclassification of the cloud in terms of liquid-only and ice-producing. A measurement example of such a cloud at Punta Arenas is shown in Fig. 4.5, where the ice phase is only visible downwind as soon as the droplets have evaporated (more detailed discussion follows in Sec. 6.2.2). Similar clouds occurring at Leipzig were reported by Ansmann (2005) solely based on lidar observations. For clouds in the heterogeneous freezing regime, Cotton and Field (2002) found that only rapid evaporation freezing once the downdraft commences could explain their observations, where evaporation freezing can be better characterized as inside-out contact freezing of shrinking particles (Durant, 2005). A more recent study by Field et al. (2012) found that condensation and immersion freezing are needed together with deposition and evaporation freezing to explain their aircraft observations of ice formation in wave clouds. However, due to the highly laminar flow, opposed to the confined, fully developed turbulence found in layered mixed-phase clouds, the microphysical conditions cannot be directly compared. Consequently, the frequent occurrence of atmospheric gravity waves in a specific region might increase the frequency of thermodynamic conditions that favor the presence of a sustained liquid phase. As Korolev (2007) demonstrated, long-lasting steady updrafts are required to make the liquid phase dominating over the ice phase. Probing an observational dataset for the presence of long-lasting updrafts could therefore provide a hint on the role of atmospheric gravity waves in the occurrence of enhanced concentration of supercooled liquid water.

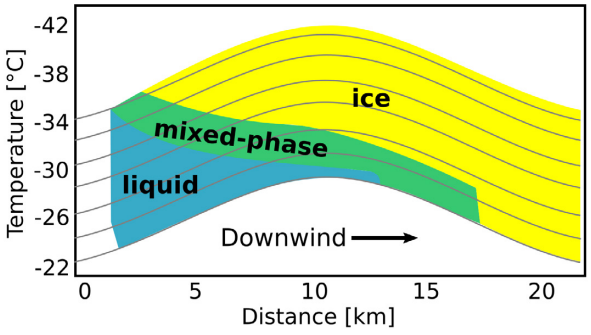

Figure 4.4: Schematic depiction of cloud phase under wave conditions. Adapted from Heymsfield and Miloshevich (1993).

Turbulence properties of the liquid layer in the clouds subject to our study can be derived from the vertical-velocity observation by Doppler lidar (Bühl et al., 2019a). The small size of droplets in the liquid-dominated cloud top layer and their negligible terminal velocity make them tracers of air motion. From the Doppler lidar observations, the vertical velocity is sampled at the pixel with the maximum backscatter out of the heights identified as liquid-containing in the Cloudnet classification. The height of these samples is indicated with dashed lines in Fig. 4.3c and 4.5a. The temporal resolution of the resulting time series is 2 s, i.e., equal to the Doppler lidar raw data. This time-series is then used to characterize the vertical air velocities of the cloud top layer. As described above, the dynamics in wave clouds differs from the radiative-cooling-driven stratocumulus clouds. Just comparing the clouds shown in Fig. 4.3c and Fig. 4.5a illustrates how the vertical-velocity patterns differ for both cloud types. To separate both regimes in the large dataset, an characteristic parameter is needed. The autocorrelation function was found to be a pragmatic choice for such a parameter.

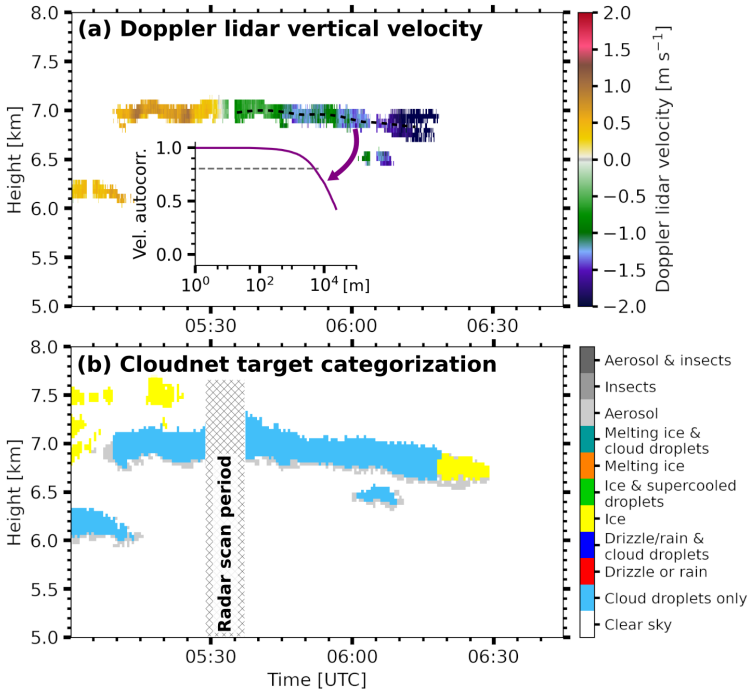

Figure 4.5: Wave cloud observed at Punta Arenas on 27 September 2019, 05:00–06:45 UTC. (a) Doppler lidar vertical velocity and (b) Cloudnet target categorization. The inset in (a) shows the autocorrelation function of the vertical velocities in the liquid-dominated layer (heights indicated with dashed lines).

The autocorrelation function Ψ for a time series of vertical velocities v_t is defined as

$$\Psi = \sum_t v_t \, v_{t+\tau}, \tag{4.8}$$

with the temporal shift τ and the vertical velocity v at time t. To compare different cloud cases, the autocorrelation function Ψ is normalized with Ψ_0, i.e., at $\tau = 0$. The temporal shift τ from the observations is converted into a horizontal shift or

autocorrelation length l with the Cloudnet model-based horizontal wind velocity v_{hor}:

$$\Psi_l = \Psi v_{\mathrm{hor}}. \tag{4.9}$$

Similarly, the vertical-velocity spectral power density is calculated by a FFT of the vertical-velocity time series. High autocorrelation coefficients for large shifts and low power density are indications for wave-driven, low-turbulent flow. The inset in Fig. 4.3c shows the autocorrelation function for each of the identified cloud cases. All of them are weakly affected by gravity waves, but small-scale turbulence dominates. In contrast, the wave cloud in Fig. 4.5b shows high autocorrelation coefficients for longer shifts. As a characteristic value of the autocorrelation function, the shift at which the coefficient drops below 0.8 was chosen after visually inspecting the whole dataset. When the ice formation frequency statistics is investigated for an influence of gravity waves (Sec. 6.6), the shift threshold is reduced step by step. As the autocorrelation function is generally decreasing, a lower characteristic value than 0.8 would result in larger shift thresholds. For shifts larger than about 500 m, random fluctuations appear for clouds with a rapid drop in autocorrelation coefficients. Hence, 0.8 is a robust choice for the characteristic value.

4.7 Continuous airmass source attribution

Time-height-resolved airmass source attribution is an important prerequisite for the interpretation of profiling ground-based remote-sensing observations. Ideally, such an airmass source estimate continuously covers the same time-height section as the remote-sensing observations in question. The methodology described in this section combines backward trajectories or particle positions from a dispersion model with geographical information (a surface classification, manually defined areas, and latitude bands) into an automated algorithm. The product is a continuous and vertically resolved estimate of an airmass source above a certain location. After the methodology is introduced in the following, two example cases characterizing long-range transport are shown, one with dust transport to Limassol and one with smoke transport to Punta Arenas. The content described in this section is part of the publication Radenz et al. (2021a). More details and additional analysis can be found therein. Long-term statistics of airmass source for the campaign periods will follow in Chapter 5.3.

Method

The approach combines backward simulations of air parcel locations with geographical information such as surface classes into residence times per surface category. The simulations are repeated at intervals of 3 h in time and 500 m in height, giving a continuous estimate of airmass source.

The transport pathway of an airmass arriving over the site can be computed using either mean-wind trajectories or a particle dispersion model (see an overview provided by Fleming et al., 2012). Trajectory models calculate the transport of a single air parcel imposed by the mean meteorological fields. The model simulations can be

run either forward or backward in time, providing information about the source and the destination of the airmass, respectively, after a given transport time. Turbulence and vertical motion during the transport are usually parameterized on the grid scale. Commonly used models are HYSPLIT (Hybrid Single-Particle Lagrangian Integrated Trajectory model; Stein et al., 2015), FLEXTRA (FLEXible TRAjectories; Stohl et al., 1995), and LAGRANTO (Lagrangian analysis tool; Wernli and Davies, 1997; Tarasova et al., 2009). Due to the rather simple approach, the results are quite uncertain (Seibert, 1993; Polissar et al., 1999), but computational requirements are comparably low. A straightforward approach for representing some of the variability is calculating spatial or temporal ensembles of the trajectories (Merrill et al., 1985; Kahl, 1993; Draxler, 2003). Lagrangian particle dispersion models (LPDMs), with a large number of particles, are set up to cover turbulent and diffusive transport even more realistically (Stohl et al., 2002). The fate of each particle is tracked individually, allowing more variability to be included into the transport simulation. A frequently used LPDM is FLEXPART (FLEXible PARTicle dispersion model; Stohl et al., 2005; Pisso et al., 2019).

Generally, the representation of chaotic motion in the atmosphere improves with larger ensembles of trajectories or increasing numbers of particles. However, with dozens to hundreds of air parcel locations available, interpretation rapidly becomes cumbersome. A number of infinitesimally small air parcels grouped together gives an airmass, which is a larger volume of air with similar properties. The calculation of residence times is a well-established technique for attributing regional information to airmass properties, such as being laden with aerosol, moisture, or trace gases (Ashbaugh, 1983; Ashbaugh et al., 1985; Heintzenberg et al., 2013).

Using backward simulations of air parcel positions, analysis of the residence time yields useful information about the potential source region of an observed airmass. The basic assumption is that the longer an air parcel was close to the surface in a certain region, the more likely it was influenced by the surface characteristics. The proximity to the surface can be parametrized as a reception height, which depends on the mixing state of the atmosphere at the respective location and on the type of aerosol particles that could potentially be emitted (e.g., mineral dust or sea salt). Conceivable choices for the reception height are the model-derived depth of the atmospheric boundary layer or fixed thresholds. As a first estimate for the identification of possible surface effects on an air parcel, 2 km is widely used (Val Martin et al., 2018). Different settings can be easily applied to study events that are entrained at greater heights, such as wildfire smoke emission or volcanic eruptions.

The challenge is to reduce the dimensionality of an air parcel's 4D location. Approaches for clustering backward trajectories by direction, source regions, or latitude are widely used. The majority focus on the interpretation of time-series observations at single heights, mostly close to the ground (e.g., Escudero et al., 2011), for aircraft intersects (e.g., Paris et al., 2010), or over a whole region (Lu et al., 2012).

For the backward simulations both mean-wind trajectories and particle positions from a LPDM are used. Mean-wind trajectories for the past 10 days are calculated

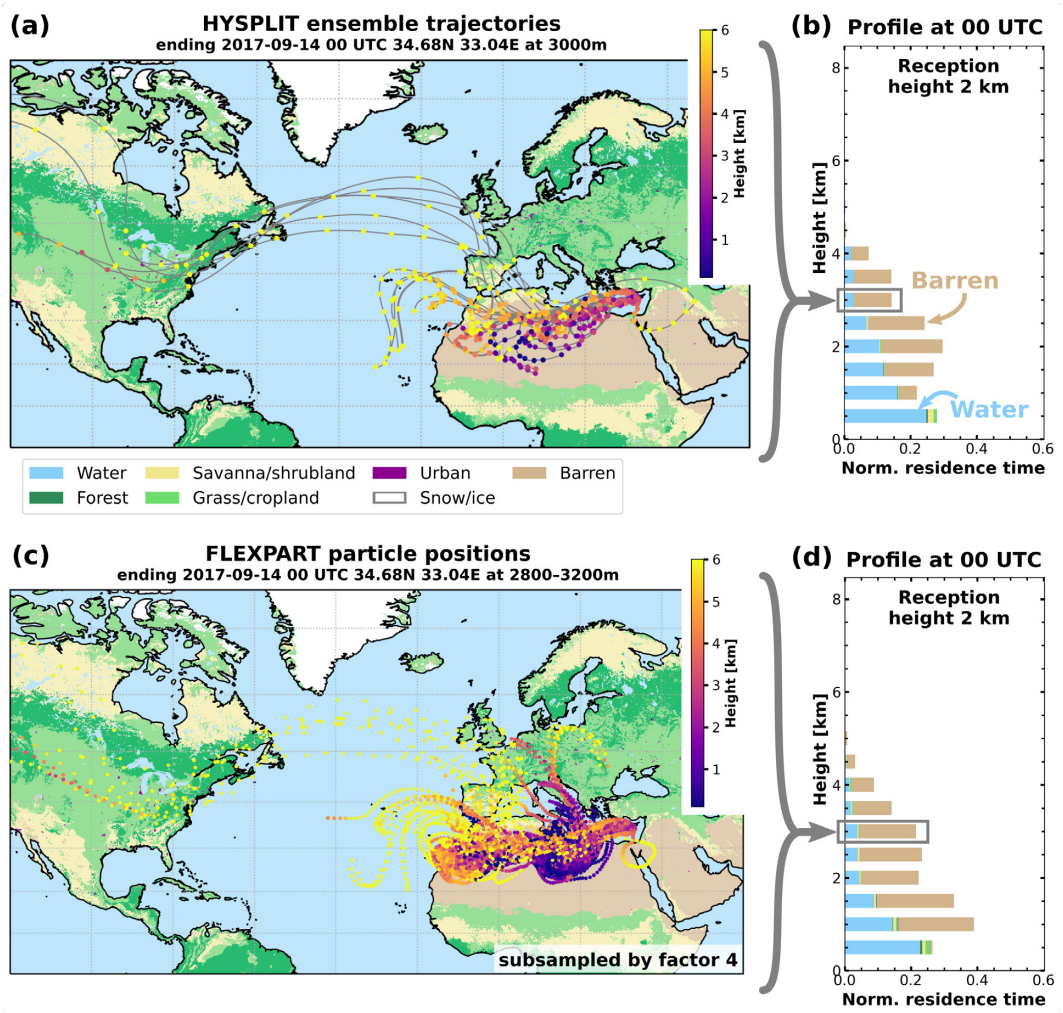

Figure 4.6: Example of how the residence-time profile is calculated above Limassol on 14 September 2017. (a) HYSPLIT ensemble backward trajectories and (c) FLEXPART particle positions ending at 3 km height at 00 UTC. The profiles of normalized residence time with a reception-height threshold of 2 km for (b) HYSPLIT ensemble trajectories and (c) FLEXPART particle positions are shown for all heights. The number of FLEXPART particles is reduced by a factor of 4 in this visualization (i.e., 10000 instead of 40000). Air parcel height is color-coded. The simplified MODIS surface classification (Fig. 4.7) is shown in the background.

using HYSPLIT (Stein et al., 2015). To account for variability, ensemble trajectories consisting of 27 members, spaced 0.3° horizontally and 220 m vertically around the end point, are used (Fig. 4.6a). Meteorological input data for HYSPLIT are obtained from Global Data Assimilation System at 1° (GDAS1). The location of the air parcel is stored in 1 h steps. A more realistic representation of turbulence and mixing can be achieved using a LPDM, which simulates the pathway of hundreds to thousands of particles. Here, the most recent version of FLEXPART (Stohl et al., 2005; Pisso et al., 2019) is used. Meteorological data are obtained from the Global Forecast System (GFS) analysis at a horizontal resolution of 1°. For each height, 500 particles are used, with the particle positions being stored every 3 h (Fig. 4.6c). These simulations are run every 3 h, with height steps of 500 m for the whole period of interest.

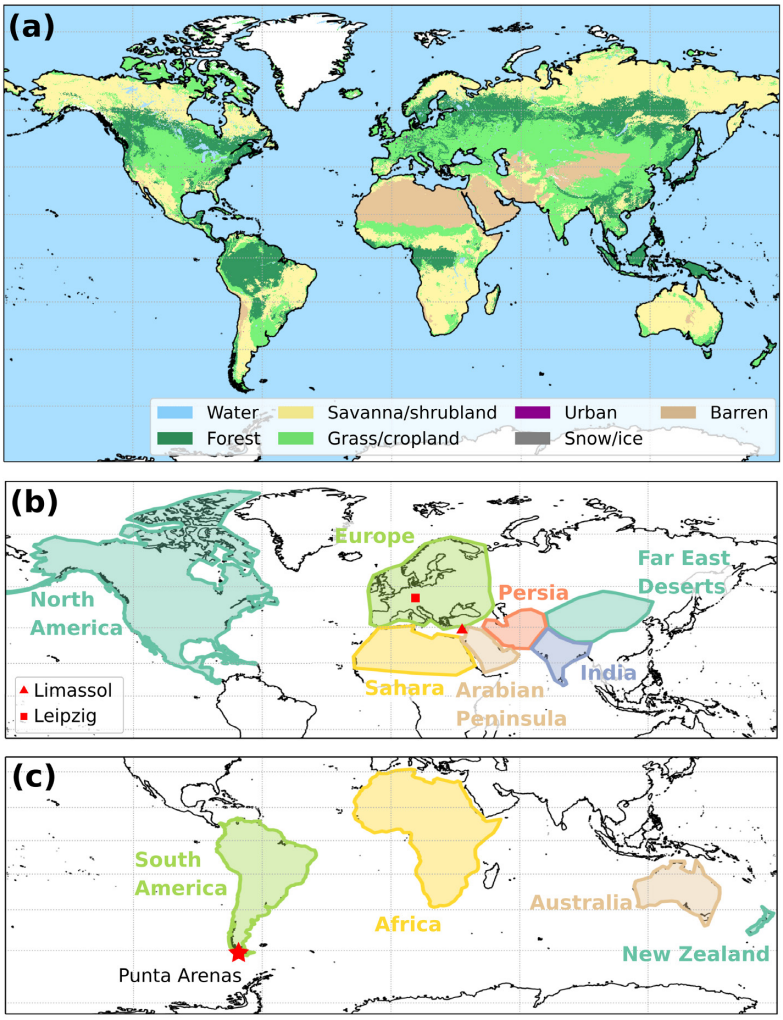

Figure 4.7: The simplified MODIS surface classification (a) with details given in the text. The customly defined geographical areas for Limassol, Leipzig (both a) and Punta Arenas (b). 'North America' is used for Leipzig and 'Far East Deserts' for Limassol, but the selection of regions can be easily adapted for specific questions. Locations of the sites are also marked in the respective map.

Three methods are used to characterize the surface. The first method is based on a simplified version of the MODIS surface classification (Friedl et al., 2002; Broxton et al., 2014). The 17 categories of the original data set are grouped into seven categories

Table 4.2: Translation of the MODIS land surface categories into the simplified categories used in this study. MODIS Category numbers as in Broxton et al. (2014).

MODIS Category	Simplified Category
0	water
1, 2, 3, 4, 5, 6	forest
7, 8, 9	savanna/shrubland
10, 11, 12, 14	grass-, cropland
13	urban
15	snow
16	barren

according to Table 4.2 in order to allow for robust statistics in the output (Fig. 4.7a). Additionally, the horizontal resolution is reduced to 0.1°. The categories do not resolve the annual cycles, e.g., due to vegetation seasons. The second method involves custom-defined regions as polygons, named according to their geographical context (Fig. 4.7b, c). These areas can be tailored to the measurement location and/or scientific interest. The third method groups the particles into latitude bands of 30° to characterize meridional transport.

The residence times for each category and each height can then be visualized as a profile (Fig. 4.6b, d). Where the residence time is 0, no air parcels were observed below the reception height during the duration of the backward simulation. In the example shown in Fig. 4.6b, above 5 km height, no airmasses resided at heights below 2 km above the ground in the previous 10 days. The theoretical maximum residence time (in hours) $t_{\max}$ depends on the number of trajectories or particles n, the duration of backward calculation d in days, and the interval of output Δo in hours:

$$t_{\max} = n\, d\, \frac{24}{\Delta o}. \tag{4.10}$$

In the final step, the obtained residence times per category are normalized with $t_{\max}$.

To illustrate the temporal evolution, successive airmass source profiles can be shown one after another. This visualization condenses the 4D history of a multitude of trajectories (or thousands of particle positions) to a quickly understandable summary, which structures information on airmass source into a time-height cross section.

Example 1: Long-range transport of dust to Limassol

On 14 September 2017, an upper-level short-wave trough moved eastward from the Aegean Sea towards Cyprus. Above 1 km height, the wind turned from south-west to south during the course of the day with velocities ranging from 5–15 $\mathrm{m\,s^{-1}}$, whereas below, wind velocity was lower and direction more variable.

The time-height cross-section of quasi particle backscatter observed by Polly$^{\mathrm{XT}}$ at Limassol shows two pronounced aerosol layers above the boundary layer (Fig. 4.8). The first layer was observed between 1 and 2 km height from 0 to 9 UTC and a second, thicker layer after 3 UTC. Until the night, this layer increased in thickness from bases

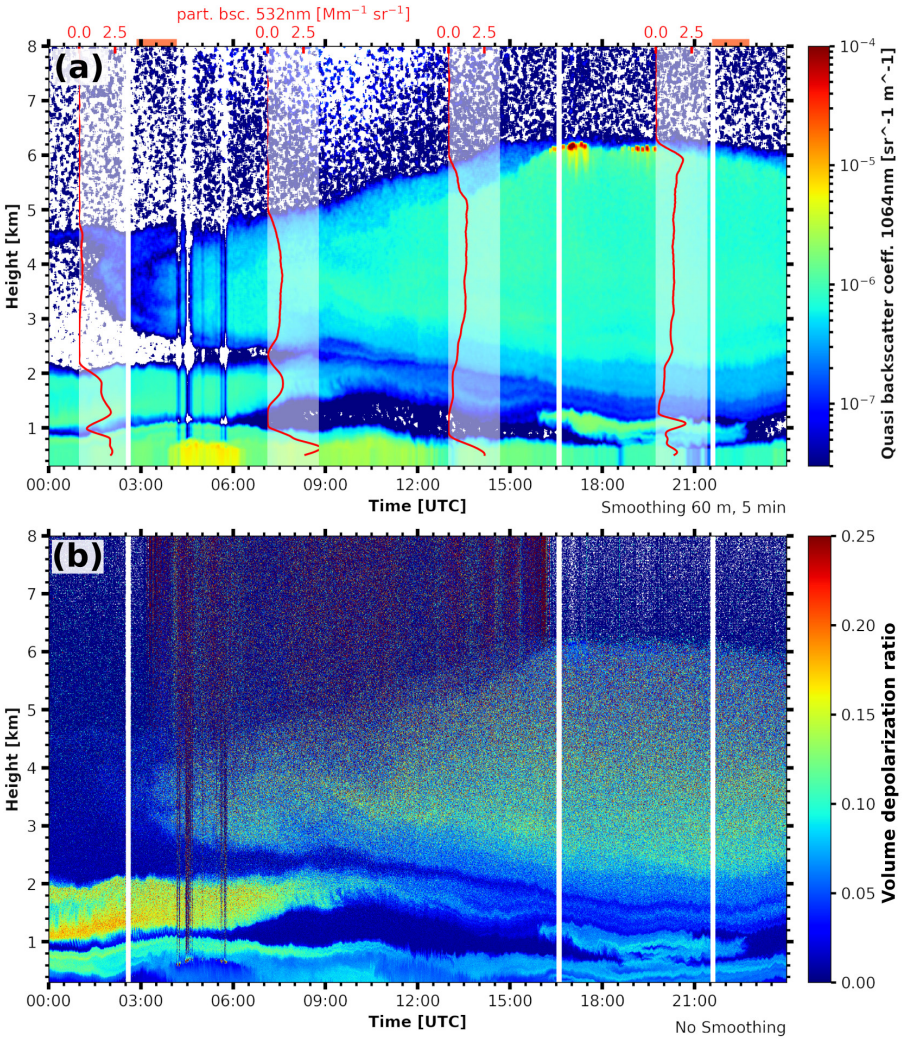

Figure 4.8: (a) Quasi particle backscatter coefficient at 1064 nm observed with Polly^{XT} at Limassol on 14 September 2017. Sliding average smoothing of 8 range bins (60 m) and 10 temporal bins (5 minutes) was applied. The red overlays show the Klett-derived particle backscatter coefficient at 532 nm. The time periods of manual analysis (Fig. 4.9 and 4.10) are marked by horizontal orange bars. (b) Volume depolarization ratio at 532 nm for the same period. No smoothing was applied.

at 3 and tops at 4.5 km height to bases at 1.2 and tops at 6.5 km height. The boundary layer itself was also laden with aerosol and showed significant backscatter below 1 km height.

The optical parameters of the aerosol plume were analyzed for two periods, 02:59 to 04:02 UTC in the morning and 21:41 to 22:39 UTC in the evening (periods marked on top of Fig. 4.8a with horizontal orange bars). The profiles from the morning period (Fig. 4.9) show particle depolarization ratios of 0.25 (355 and 532 nm), low backscatter-related Ångström exponent values and lidar ratios around 40 sr (355 and 532 nm) for the lower layer at 1.8 km height. These optical parameters and their independence of wavelength are typical for aerosol mixtures with a high dust fraction. Extinction in this layer peaks at 72 Mm^{-1} (355 and 532 nm). The second layer above 2.5 km height has particle backscatter values of less than 2 Mm^{-1} sr^{-1} (at 355 nm) and 0.5 Mm^{-1} sr^{-1} (at 532 nm). The extinction coefficient shows two sublayers, with values less 25 Mm^{-1}

between 2.5 and 4.0 km, and values around 40 Mm^{-1} above. Ångström exponent values are higher than in the lower layer, varying between 1 and 2. The particle depolarization ratios at both 355 and 532 nm wavelength are between 0.05 and 0.10. This upper layer observed during the morning is already the leading edge of the second plume, which increased in thickness during the day (both geometrically and optically). As shown in Fig. 4.8b, the volume depolarization ratio increased only slowly during the averaging period.

During the evening (Fig. 4.10), the upper layer extended from 1.3 to 6 km height and showed homogeneous and mostly wavelength-independent optical properties throughout. Particle depolarization ratios were between 0.10 and 0.15, with 532 nm values slightly higher than at 355 nm. Lidar ratios in that layer were 35 sr, typical for Middle East dust (Mamouri et al., 2013; Nisantzi et al., 2015), while the particle depolarization ratio hints towards a mixture of mineral dust and anthropogenic pollution (e.g., Tesche et al., 2009).

The airmass source estimate (Fig. 4.11) identifies transport from barren-ground-influenced air from the Sahara until 9 UTC. Later, corresponding to the change in wind direction, the source for the air aloft is identified as Arabian Peninsula, but still the barren class. Below 1 km height, a mixture of airmasses was observed, originating mostly from Europe. Comparing the source estimate based on HYSPLIT (Fig. 4.11a, c) with the one from FLEXPART (Fig. 4.11b, d), it is found that both models agree qualitatively well again. While the general transition was captured by the source estimate, the leading edge of the 'Arabian Peninsula' plume was observed over Limassol earlier than indicated. The increase in thickness of this plume is represented in the source estimate as well.

Example 2: Long-range transport of biomass-burning smoke to Punta Arenas

Though the free troposphere above Punta Arenas is clean and rarely affected by anthropogenic influences (Hamilton et al., 2014), events of aerosol long-range transport occur occasionally (Foth et al., 2019; Floutsi et al., 2021). Due to the large distance between Punta Arenas and the aerosol source regions, an attribution of observed aerosol events is, in general, rather complicated. The application of airmass source estimates for the characterization of an aerosol long-range transport event is presented here. An upper-level ridge was located off the Chilean coast on 20 May 2019, which also supported a surface high-pressure system. At Punta Arenas, the flow was zonal throughout the troposphere. Within that flow, long-range transport from across the Pacific Ocean occurred.

In the Polly^{XT} observations from 20 May 2019, a layer of increased backscatter is present from 02:00 UTC to roughly 10:00 UTC. This layer extends from 3 km to above 6 km height (Fig. 4.12). From 14:00 to 18:00 UTC a low-level liquid cloud was observed at 1.5 km height. The cloud was optically thick enough to significantly attenuate the laser beam, causing lack of signal at larger heights. Occasional cirrus clouds also enhanced the backscatter in the free troposphere, e.g., at 12:00 UTC,

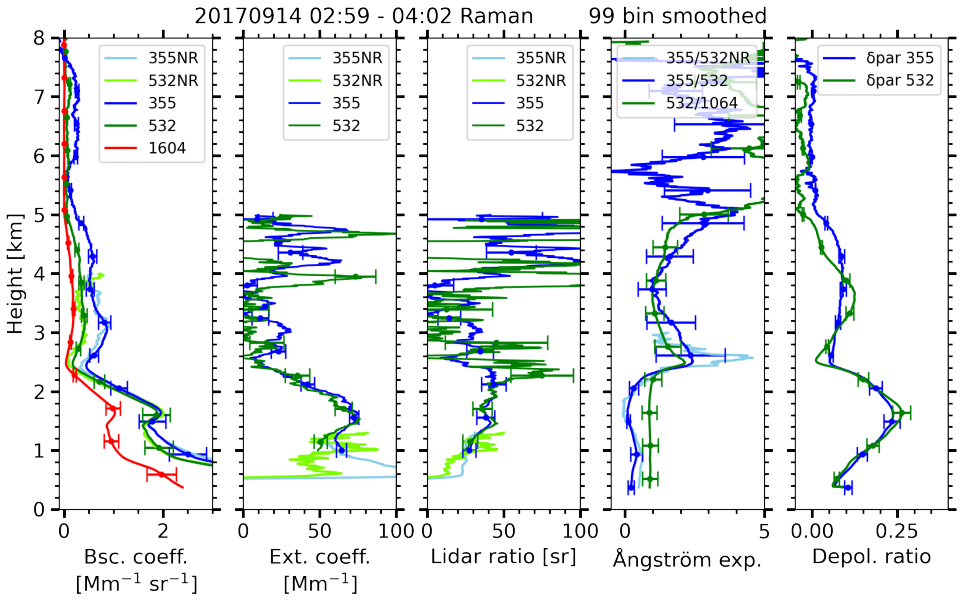

Figure 4.9: Profiles of optical properties at Limassol on 14 September 2017, 02:59–04:02 UTC, manually derived with the Raman method. A vertical smoothing of 99 range bins (742.5 m) was applied. The abbreviation NR marks profiles observed with the larger-field-of-view near-range telescope.

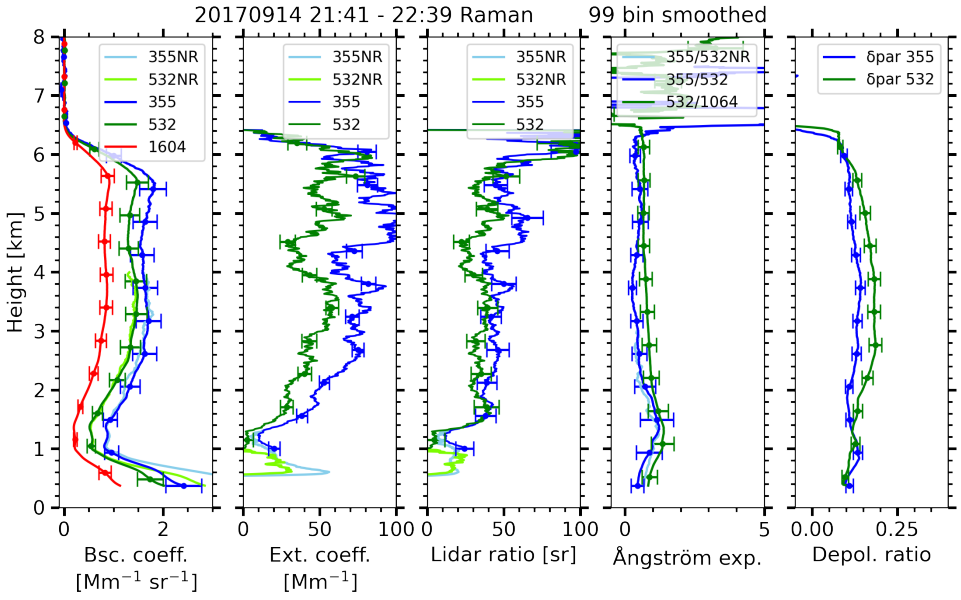

Figure 4.10: Profiles of optical properties at Limassol on 14 September 2017, 21:41–22:39 UTC, manually derived with the Raman method. A vertical smoothing of 99 range bins (742.5 m) was applied. The abbreviation NR marks profiles observed with the larger-field-of-view near-range telescope.

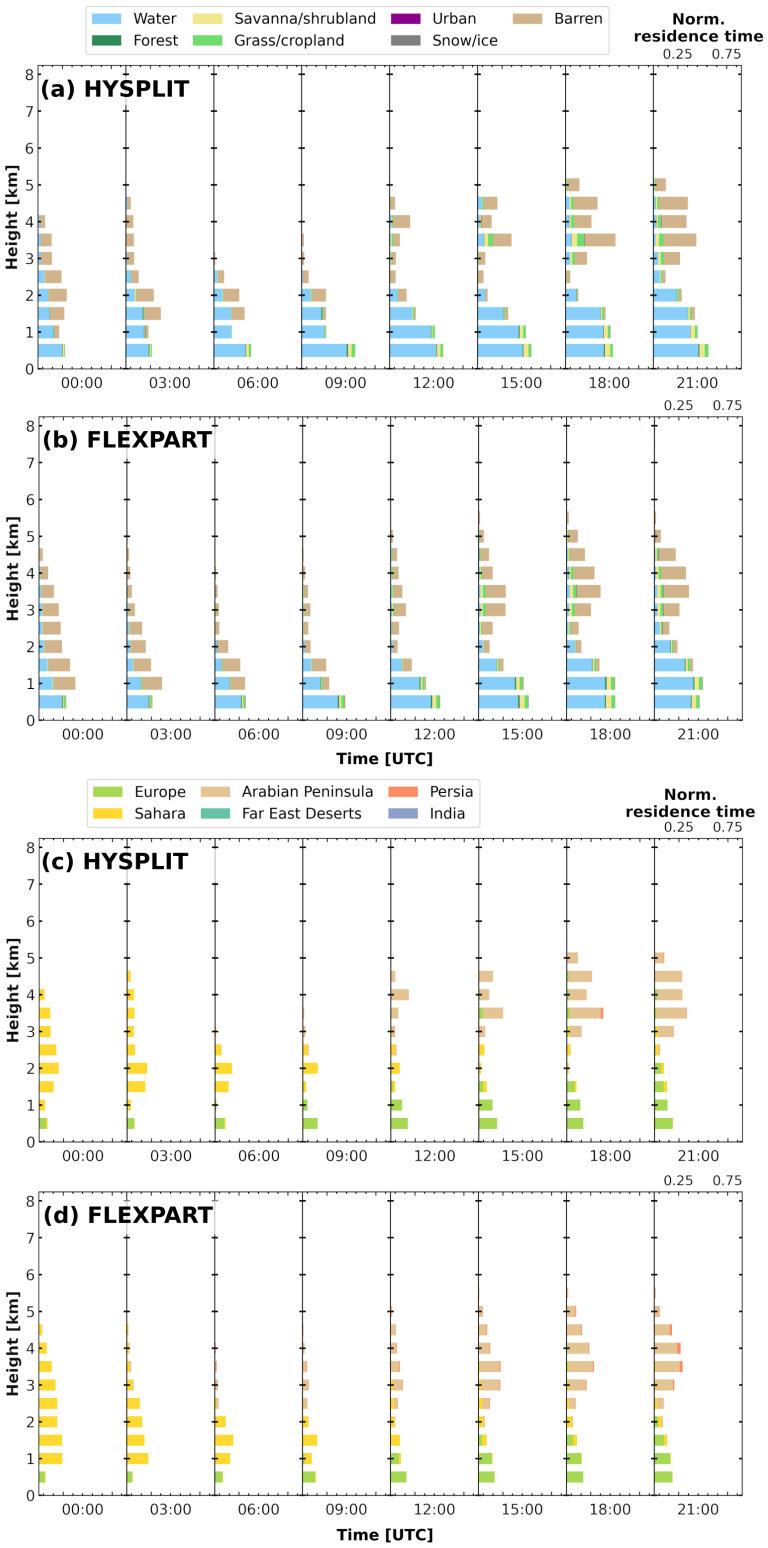

Figure 4.11: Airmass source estimate for Limassol on 14 September 2017 for the surface classification (a, b) and the named source region (b, d) based on HYSPLIT ensemble trajectories (a, c) and FLEXPART particle positions (b, d).

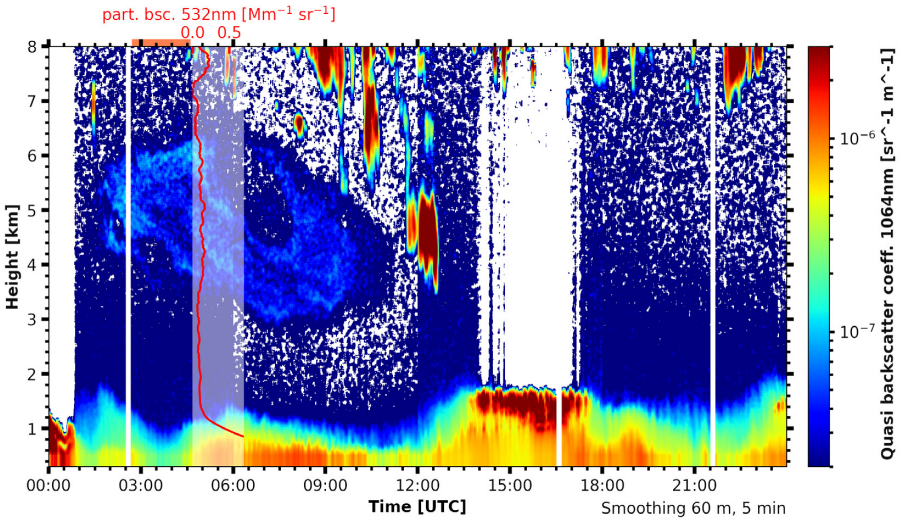

Figure 4.12: Quasi particle backscatter coefficient at 1064 nm observed with Polly^{XT} at Punta Arenas on 20 May 2019. Sliding average smoothing of 8 range bins (60 m) and 10 temporal bins (5 minutes) was applied. The red overlay shows the Klett-derived particle backscatter coefficient at 532 nm wavelength. The time period of manual analysis (Fig. 4.13) is marked by a horizontal orange bar.

between 4 and 5 km height. The values of particle backscatter peaked at 0.3 Mm^{-1} sr^{-1} (Fig. 4.13), which are significantly lower values than reported for the prior cases. In the period analyzed, extinction values were approximately 15 Mm^{-1} giving lidar ratios well above 50 sr. Also low particle linear depolarization ratios were observed. Altogether, these optical parameters agree with prior findings of wildfire smoke in the troposphere (Tesche et al., 2011; Burton et al., 2012; Groß et al., 2013; Veselovskii et al., 2015).

The airmass source estimate is also able to capture this faint aerosol layer. Fig. 4.14 shows that airmasses from Australia were present from 3 to 6 km height between 03:00 and 09:00 UTC. In terms of surface class, these airmasses were characterized by savanna/shrubland and grass. Wildfires were active in southwestern Australia between 10 and 16 May 2019, which is also the region where the backward simulations end. Apart from the described period, the airmasses were solely influenced by the Southern Ocean (i.e., the water class). FLEXPART simulations (Fig. 4.14b, d) agree with the HYSPLIT results; however, the computed temporal extent and the residence times are slightly longer for the latter. Hence, the airmass source scheme is also capable of capturing aerosol transport at hemispheric (i.e., more than 10 000 km) scales.

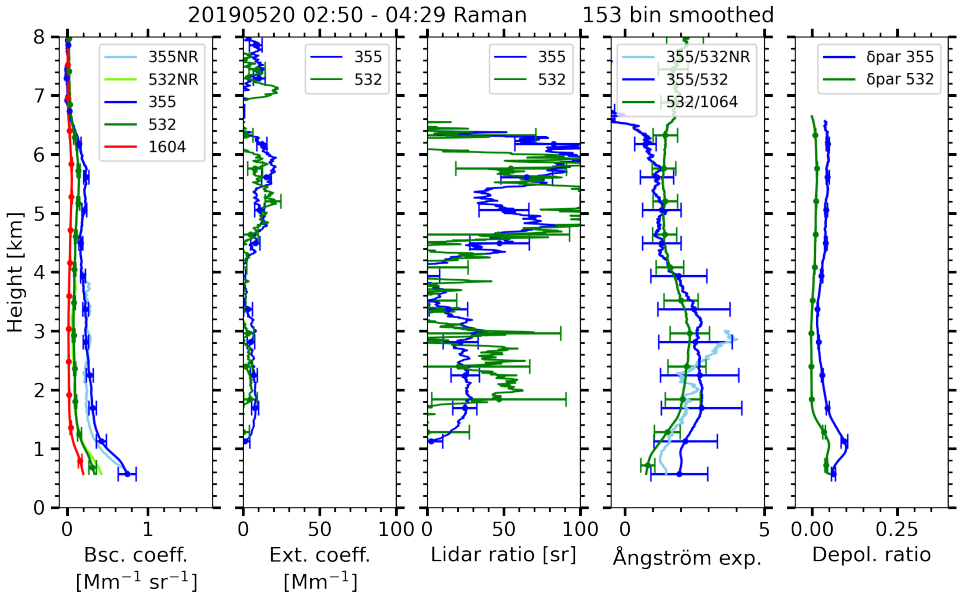

Figure 4.13: Profiles of optical properties at Punta Arenas on the 20 May 2019, 02:50–04:30 UTC, manually derived with the Raman method. A vertical smoothing of 153 range bins (1147.5 m) was applied. The abbreviation NR marks profiles observed with the larger-field-of-view near-range telescope.

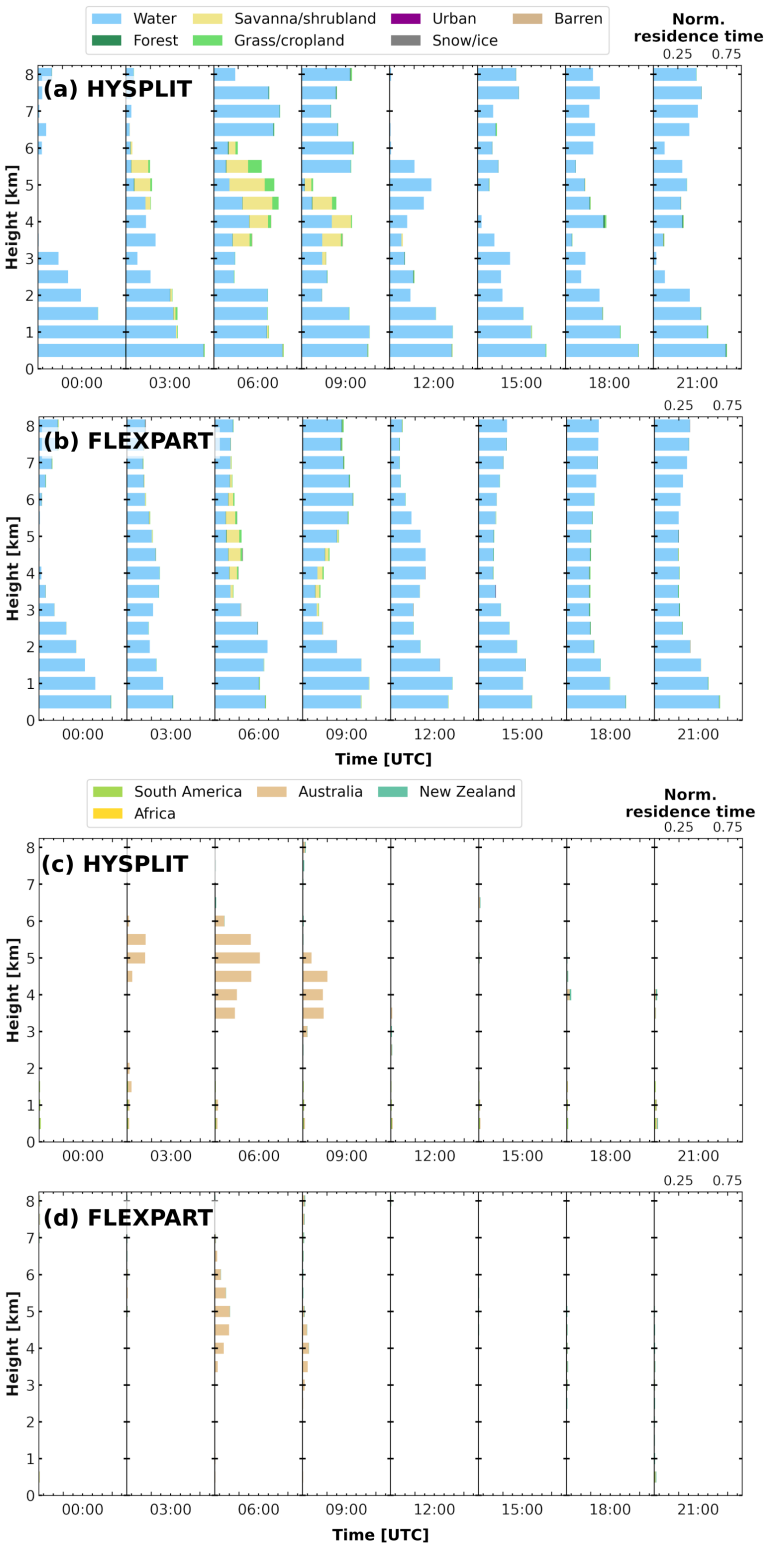

Figure 4.14: Airmass source estimate for Punta Arenas on 20 May 2019 for the surface classification (a, b) and the named source region (b, d) based on HYSPLIT ensemble trajectories (a, c) and FLEXPART particle positions (b, d).

4.8 Transforming the Doppler spectrum into a tree structure

Frequently, clouds are composed of multiple particle populations, even on small scales. Cloud radar Doppler spectra (Sec. 4.3) often show these particle populations as distinct peaks. However, multi-peaked situations are not taken into account by established analysis techniques, which focus on the moments of the Doppler spectrum.

The technique introduced in this section uses a binary tree structure to recursively represent peaks and subpeaks in a Doppler spectrum. It was published by Radenz et al. (2019a) and was successfully used to identify liquid layers as well as to separate different ice particle populations in precipitating Arctic clouds. The processing software is publicly available (Radenz et al., 2019b). When investigating thin stratiform clouds, the technique can be employed to identify situations, where the liquid-dominated layer is exposed to seeding by ice particles. An example case illustrating such a situation is presented at the end of the section.

peakTree method

Fig. 4.15a illustrates a multi-peaked Doppler spectrum as observed with MIRA-35. The three-peak structure is easily recognized by eye, but an algorithmic treatment is an unsolved problem. Following Radenz et al. (2019a), the analysis of multi-peaked Doppler spectra can actually be separated into three steps:

1. **peak identification** (or peak finding): locate the boundaries of a peak or subpeak,
2. **peak structuring**: identify the arrangement of the peak or subpeak,
3. **peak interpretation**: categorize the peaks and interprete them.

So far, almost all available methods focus on a single step. For peak identification (step 1) either noise-floor-separated peaks and/or local minima in the spectral reflectivity are used (Shupe et al., 2004; Rambukkange et al., 2011). More sophisticated approaches allow for a separation of multi-modal peaks. This is done for example by using skewness signatures (Luke and Kollias, 2013) or continuous wavelet transforms (Luke et al., 2010; Yu et al., 2014). Recently, Kalesse et al. (2019) proposed an algorithm for subjective peak identification criteria using machine learning. The structure of the identified subpeaks (step 2) is reflected by a linear list of all subpeaks, usually sorted by velocity or reflectivity. In a further step, Oue et al. (2018), using the Microscale Active Remote Sensing of Clouds (microARSCL) algorithm (Kollias et al., 2007; Luke et al., 2008), allow a primary peak to be split into two subpeaks, but they constrain the structure by assuming the left peak (faster falling particles) to have a higher reflectivity. Additionally, a noise-floor separated secondary peak is possible, but this one is assumed to be mono-modal. Such strong constraints may be justified for short periods at single geographic locations, but are not suitable for a general approach, as will be shown in Chapter 7. Categorization and interpretation is usually done by visual inspection or very simple selection rules.

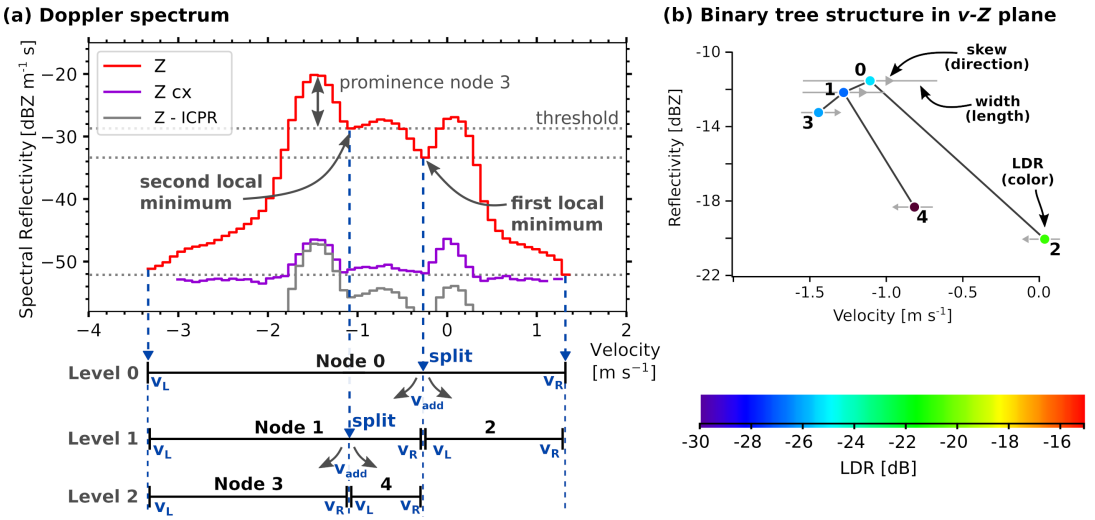

Figure 4.15: Demonstration of tree generation from a Doppler spectrum. The root node (Node 0) is split into child nodes at the indicated velocity bins (dashed blue) that contain a local minimum in spectral reflectivity. The thresholds defined by the noise-floor and the internal minima are marked with dashed grey lines. Panel (b) shows the resulting trees, where the location of a node in the v-Z space is based on its moments. Spectral width is indicated quantitatively by the length of the grey lines and sign of the skewness is indicated by a triangle (pointing to the left for negative skewness and vice-versa). The circle denoting the node position is color-coded in accordance with the LDR.

The peakTree method uses a binary tree structure, which makes it possible to drop all a-priori constraints on number and structure of subpeaks, while providing a rigid and flexible formalism and easy access for algorithms. A tree is a directed graph with one root node. Such a data structure can easily be accessed ('traversed') by algorithms. Specifically, a full binary tree is generated that might recursively either possess two child nodes or none (Garnier and Taylor, 2009). An example of a complete binary tree is given in Fig. 4.16. Each node is identified by an index derived from the level-order tree traversal. This index i of a child node is calculated by:

$$i_{\text{left child}} = 2\,i_{\text{parent}} + 1, \tag{4.11}$$

$$i_{\text{right child}} = 2\,i_{\text{parent}} + 2. \tag{4.12}$$

For a given child, the parent can also be calculated:

$$i_{\text{parent}} = \left\lfloor \frac{i_{\text{child}} - 1}{2} \right\rfloor, \tag{4.13}$$

with the floor function $\lfloor\ \rfloor$[‡].

A binary tree is complete, if all possible nodes in the lowermost level are present. In a full tree some indices might be missing, e.g., 9 and 10 or 5, 6, 11, 12, 13, and 14. The rule 'a node might possess either two child nodes or none' will always hold.

Applied to radar Doppler spectra, a node is related to a part of the Doppler spectrum that contains at least one peak. The peak boundaries are identified (step 1 as listed

‡. Function that rounds down to an integer, e.g., $\lfloor 2.8 \rfloor = 2$.

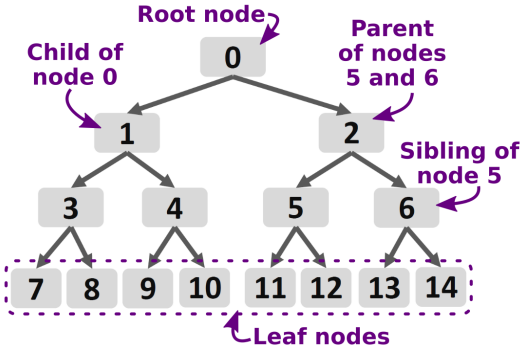

Figure 4.16: Binary tree containing 15 nodes with possible indices according to level-order tree traversal. Relationships between certain nodes are highlighted.

Table 4.3: Moments for each peak from the Doppler spectrum depicted in Fig. 4.15a with the index i of the node according to the level-order tree traversal. The boundaries v_L, v_R are given in $\mathrm{m\,s^{-1}}$. Child-nodes are denoted by their level of indentation. The units are dBZ for reflectivity Z and $\mathrm{m\,s^{-1}}$ for $\overline{v}$ and spectral width σ. The skewness γ is dimensionless, LDR is in dB. The threshold 'thres.' is in dBZ and the prominence 'prom.' is in dB.

i	Boundaries $[v_\mathrm{L}, v_\mathrm{R}]$	Z	$\overline{v}$	σ	γ	LDR	thres.	prom.
0	[−3.30, 1.32]	−11.6	−1.10	0.59	1.01	−25.3	−52.1	32.0
1	[−3.30, −0.25]	−12.2	−1.27	0.36	1.08	−26.9	−33.4	13.2
3	[−3.30, −1.07]	−13.3	−1.44	0.15	0.27	−26.1	−28.7	8.5
4	[−1.07, −0.25]	−18.4	−0.81	0.16	−0.13	-32.2	−28.7	1.4
2	[−0.25, 1.32]	−20.1	0.04	0.13	−0.31	−20.9	−33.4	6.2

above) by a noise-floor threshold and local minima in the spectral reflectivity (or spectral power density). These boundaries are then used to construct the tree structure (step 2 as listed above). The root node contains all signal of the Doppler spectrum above the noise threshold. The peak boundaries and moments are listed in Tab. 4.3. In a first step, all the noise-floor-separated peaks are added as child nodes with their boundaries v_L and v_R (in the example −3.30 and $1.32\,\mathrm{m\,s^{-1}}$). Each node is then checked for subpeaks within using the peak boundaries from the lowest to the highest spectral reflectivity. Starting with the lowest minimum at v_add, the node containing this minimum is split into two child nodes. When boundaries of the parent node are $[v_\mathrm{L}, v_\mathrm{R}]$, the left child node is $[v_\mathrm{L}, v_\mathrm{add}]$ and the right child node is $[v_\mathrm{add}, v_\mathrm{R}]$. In the example from Fig. 4.15, the internal minimum with the lowest spectral reflectivity is at $-0.25\,\mathrm{m\,s^{-1}}$ with a spectral reflectivity of $-33.4\,\mathrm{dBZ\,m^{-1}\,s}$. This reflectivity also defines the threshold that separates the subpeaks. The recursive splitting at local minima is repeated for all remaining minima. At every level the leaf node (i.e., a node that does not have any children, Fig. 4.16) that contains the v_add of the minimum is split in two new child nodes. A minimum is skipped, if the prominence of either of its subpeaks is less than 1 dB. Prominence is the difference between the maximum spectral reflectivity of a subpeak and the threshold that is defined by the spectral reflectivity at the local minimum (dashed grey lines in Fig. 4.15; similar to Shupe et al., 2004).

In the next step, the moments of the Doppler spectrum (reflectivity, mean velocity, width, skewness) are calculated for each node within its boundaries $[v_\mathrm{L}, v_\mathrm{R}]$ (see Sec. 4.3). The equivalent reflectivity factor Z (the subscript e is omitted) is calculated by integrating the spectral reflectivity of the whole peak (i.e., from the noise-floor up). For all higher moments, signal below the threshold that separated the subpeak is neglected to avoid biases. The LDR for each node is calculated using the spectral reflectivity in the cross channel, if such a channel is available.

Node 0 contains all components of the Doppler spectrum that are above the noise-floor threshold. In general, node 0 contains the same moments as obtained from traditional moment estimation methods as described in Sec. 4.3. The child nodes (1 and 2) of node 0 are the subpeaks defined by the lowest relative minimum. The second lowest minimum then splits one of these nodes and gives nodes 3 and 4 (splitting node 1) or 5 and 6 (splitting node 2). The total number of subpeaks n_subpeaks can be calculated from the number of nodes n_nodes:

$$n_\mathrm{subpeaks} = (n_\mathrm{nodes} + 1)/2. \tag{4.14}$$

Each node is characterized by its reflectivity Z, vertical velocity $\overline{v}$, spectral width, skewness, LDR and prominence. It is suitable to visualize the tree in the v-Z plane as a color-filled circle with the parent-child relationships depicted by a black line (Fig. 4.15) and each circle is color-coded in accordance with its LDR (if available). The width and skewness are shown by a horizontal grey line and a grey triangle with varying size, respectively. Thus, this representation combines all key parameters of a multi-peak Doppler spectrum.

Example: Dual-layer cloud at Punta Arenas

For demonstrating the capabilities, the multi-peak analysis technique is applied to a dual-layer cloud. On 9 January 2019 a stratiform mixed-phase cloud was observed at Punta Arenas between 18:00 and 22:00 UTC (Fig. 4.17). The lidar observed a liquid layer at 3.3 km height throughout the whole period (Fig. 4.17d). Between 19:45 and 20:30 UTC an ice virga could be observed below the liquid-dominated layer. Peak radar reflectivity in this layer was above −10 dBZ. However, no information from heights above the liquid layer can be derived by lidar alone, as the laser pulses get fully attenuated. The cloud radar reveals a second cloud layer closely above the first one (Fig. 4.17a). This layer is topped at 4.3 km height, slightly increasing to 4.7 km height. The base of this upper layer is more variable. During most of the time radar reflectivity was below −20 dBZ, but a fallstreak with higher reflectivity was observed above the virga. Due to the attenuation of the lidar signal, the upper layer is classified as ice-only (Fig. 4.17c). Sometimes the two layers are clearly separated, but especially when the virga was present, both layers were connected. From the information given by the cloud radar moments alone no deeper insights can be achieved.

The multi-peak Doppler spectra analysis reveals a bimodal situation at the interface of both layers between 19:40 and 20:40 UTC (Fig. 4.17f). During that period, two

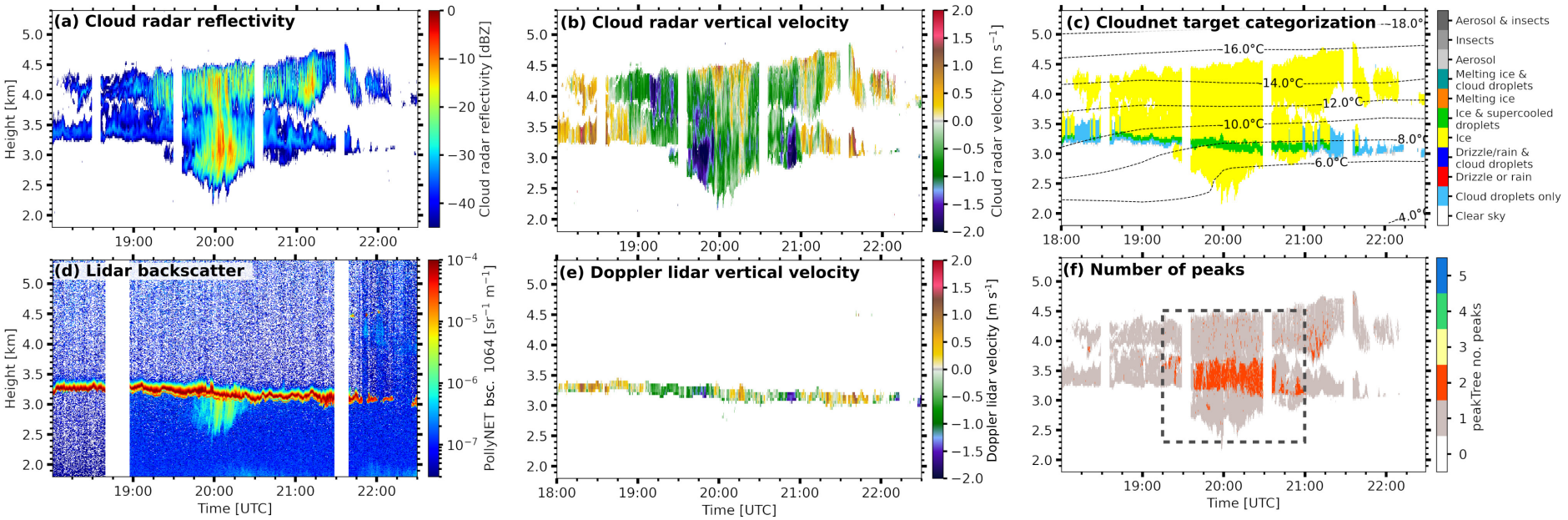

Figure 4.17: Multi-peak occurrence in a stratiform cloud at Punta Arenas on 9 January 2019, 18:00–22:30 UTC. (a) Cloud radar reflectivity, (b) cloud radar vertical velocity, (c) Cloudnet target categorization, (d) lidar backscatter, (e) Doppler lidar vertical velocity, and (f) number of peaks. The black rectangle in (f) highlights the time-height period of Fig. 4.18

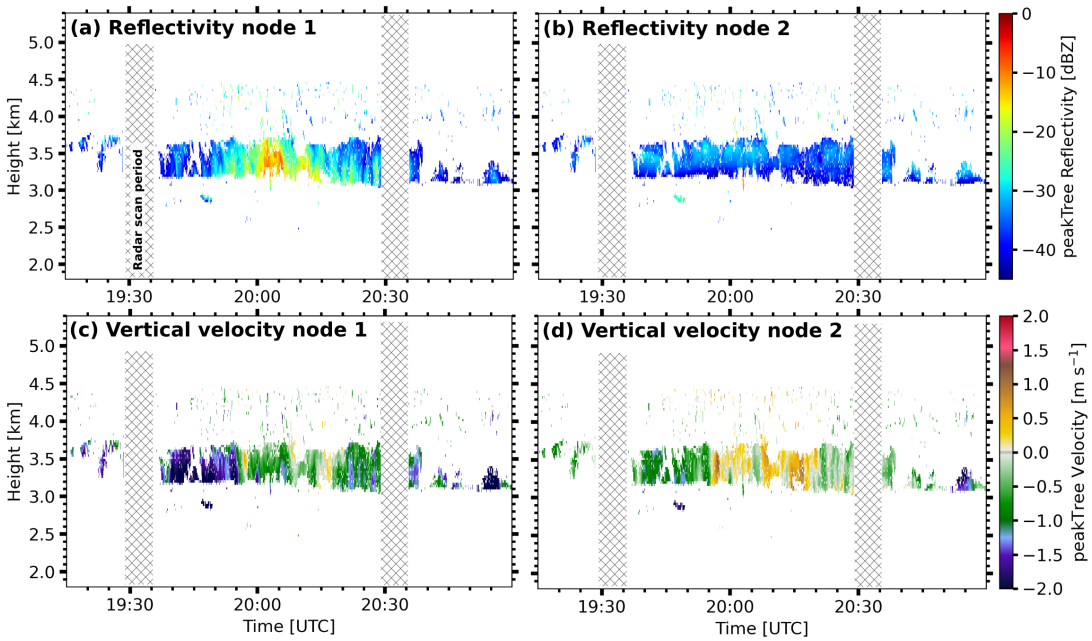

Figure 4.18: Multi-peak moments in the cloud of Fig. 4.17 (Punta Arenas, 9 January 2019). (a) Reflectivity node 1 (faster-falling particles), (b) reflectivity node 2 (slower-falling particles), (c) vertical velocity node 1, (d) vertical velocity node 2.

particle populations with different vertical velocities were present in the same volume. The highest reflectivities in the virga below the liquid layer at 3.3 km were observed during that period. Also, only then, enough ice mass precipitated out ouf the cloud to be detected by the lidar (Fig. 4.17d). Fig. 4.18 depicts the first two moments of nodes 1 and 2 during the dual-peak period. The slower-falling particles of node 2 show radar reflectivities typical for liquid droplets. Good agreement is also given for the vertical velocities found for node 2 and with the Doppler lidar. While the lidar beam is attenuated at 200 m penetration depth, the radar indicates this layer to be approximately 500 m thick. This finding is also in agreement with the single-peak periods before and after. Between 19:58 and 20:15 UTC the faster-falling particles of node 1 clearly are sedimenting ice crystals from the layer aloft. A weak increase of radar reflectivity of that particle population could be observed in the dual-peak layer. Such dual-layer clouds emphasize why only clouds with shallow liquid-dominated layers are suitable for investigating primary ice formation. However, multi-peak methods pose the potential to improve the characterization of microphysics also in deeper clouds, as illustrated in Chapter 7.

5 Contrasts in temperature, cloud and aerosol profiles

5.1 Occurrence of heterogeneous freezing regime

Heterogeneous freezing occurs under two thermodynamic prerequisites: temperatures between 0 and −35 °C and the availability of moisture. Long-term records of radiosoundings were used to asses the abundance of these thermodynamic conditions. The ascends at Lindenberg (Germany) and Athalassa (Cyprus) serve as substitutes for Leipzig and Limassol, respectively, because no long-term datasets are available directly at the sites (Sec. 3.1.4). For Punta Arenas, ascends are available directly at the airport.

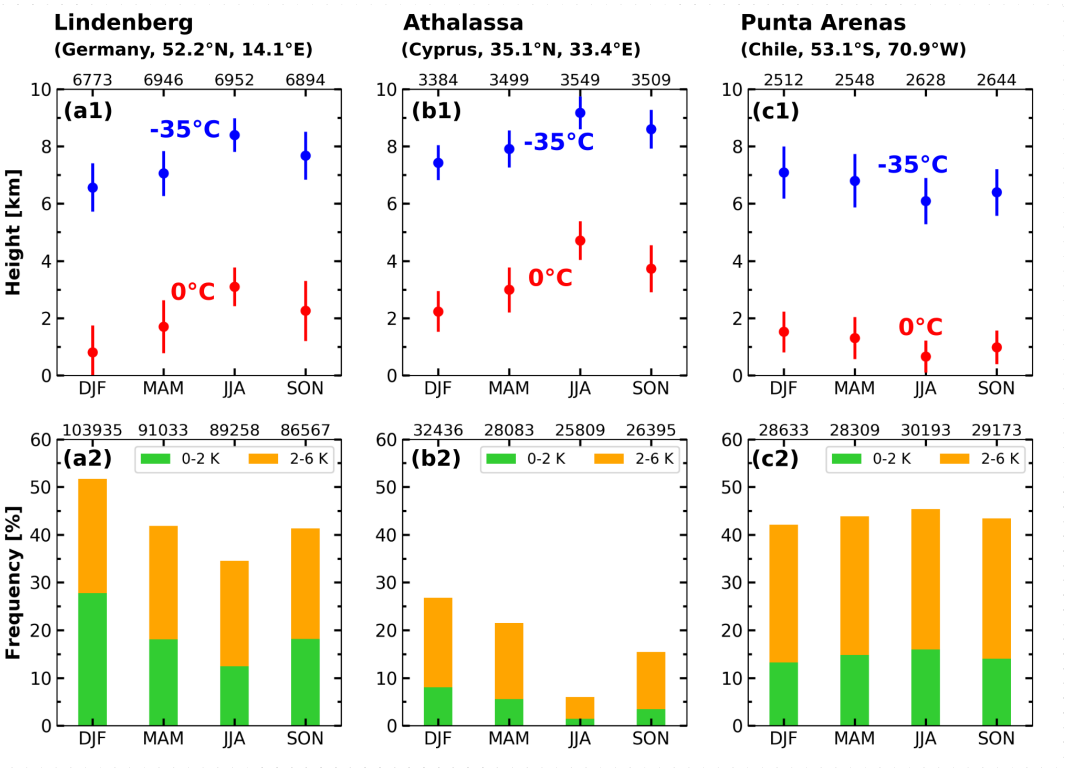

Figure 5.1: Seasonal occurrence of the heterogeneous freezing regime at (a) Lindenberg, (b) Athalassa, and (c) Punta Arenas based on radiosoundings. The upper row (1) shows the average heights of the 0 and −35 °C isotherm. Frequencies of dewpoint spreads of 0–2 K and 2–6 K within the heterogeneous freezing temperature range are shown in the lower row (2). The number of observations are given on the top of each plot. For each location soundings from 1986 to 2016 were used.

In terms of heights where heterogeneous freezing might occur (Fig. 5.1 a), all three locations show a distinct annual cycle with the maximum height of the isotherms in the respective summer seasons. At Lindenberg the 0 °C isotherm increases from 0.9 to

3.1 km height and the −35 °C isotherm from 6.6 to 8.5 km height. At Athalassa the heights increase from 2.2 to 5.7 km and from 6.2 to 9.1 km, respectively. The amplitude of the seasonal cycle is less pronounced at Punta Arenas, where the increase of the isotherms marking the heterogeneous freezing regime during summer is from 0.8 to 1.7 km and 6.1 to 7.0 km, respectively. The availability of moisture is examined in terms of dewpoint spread (Fig. 5.1 b):

$$T_{\text{spread}} = T_{\text{air}} - T_{\text{dew}}. \tag{5.1}$$

Typically, clouds form when the large-scale dewpoint spread is less than 2 K, but depending on the vertical air motions, also dewpoint spreads up to 6 K might be sufficient. In the following, the relative frequency of spread for heights with temperatures in the heterogeneous freezing regime are analyzed. At Lindenberg a clear annual cycle is visible, with maxima in winter (27% of the observed spreads less than 2 K) and minima in summer (12% respectively). A similar cycle is observed at Athalassa, but with smaller frequencies (DJF 9%, JJA 2%, respectively). At Punta Arenas seasonal variability is less pronounced, with values around 15% throughout the year. Hence, suitable conditions for clouds to form in the heterogeneous freezing regime are present throughout the year at Leipzig and Punta Arenas. However, typical for sub-tropical locations, clouds in the heterogeneous freezing regime at Limassol are only expected during winter.

5.2 Cloud frequency

The Cloudnet classification is used to provide an overview on cloud frequency and cloud properties at the three sites as observed by LACROS. Each 30 s profile is classified into one of 10 categories, which are described in the following. Two categories, 'rain_shallow' and 'rain_deep', are used for liquid precipitation. They are classified for profiles containing Cloudnet classes 'Drizzle or rain', 'Drizzle/rain & cloud droplets', 'Melting ice', or 'Melting ice and cloud droplets'. A cloud depth threshold of 4 km is used to distinguish between shallow clouds producing the rain and deep clouds. In case no rain is observed, the classification is based on the presence of liquid, ice, and mixed-phase cloud pixels. When multiple layers (i.e., a run of consecutive pixels classified as hydrometeors with 'clear sky' between them) are present and one type dominates (fraction > 0.66), the profile is assigned to the category 'multi_layer_mostly_{pure_ice, pure_liquid, mixed-phase}', otherwise to 'multi_layer_various'. Profiles with a single layer are prescribed with 'single_layer_'. If no cloud is detected, the category 'clear' is assigned.

Cloudy profiles were observed at Leipzig (Fig. 5.2a) frequently throughout the year, increasing from 60% during summer to 80% during winter. Rain is observed one-fifth of the time during the whole year. Multi-layered clouds (all types) are more frequent during the winter, whereas liquid clouds are more frequent during summer. Clouds at Limassol (Fig. 5.2b) feature a distinct annual cycle with a dry period during (boreal) summer and a rain and cloud season during winter. During winter 53% of all profiles

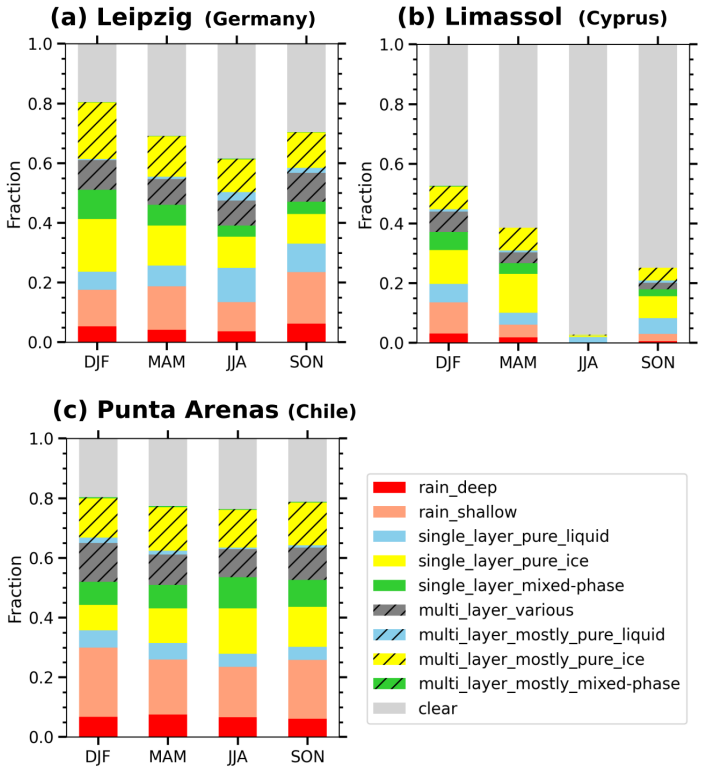

Figure 5.2: Frequency of occurrence of clouds profiles based on long-term Cloudnet observations with LACROS at (a) Leipzig, (b) Limassol, and (c) Punta Arenas.

contained clouds. This fraction drops to 4% during summer with almost no multi-layered profiles. Profiles with precipitation were present less than 14% of the time during winter and even less frequently in the remaining seasons. At Punta Arenas the sky is covered with clouds during the whole year more than 75% of the time (Fig. 5.2 c), peaking at 80% in (austral) winter. Multi-layered clouds are also most frequent during winter, whereas single-layer liquid clouds show a maximum during (austral) autumn. Rain clouds are observed 23% to 33% of the time. Based on this profile-by-profile frequency of occurrence, mixed-phase clouds are observed more than 45% of the time at Punta Arenas. At Leipzig a weak seasonal cycle is found with mixed-phase clouds occurring 35% of the time during summer and 55% during winter. Mixed-phase clouds are least frequent at Limassol, with a maximum of 30% during winter and predominantly clear-sky conditions during summer. However, this simple frequency-of-occurrence statistics neglects the structure and depth of the single clouds.

5.3 Profiles of airmass source

The source attribution methodology described in Sec. 4.7 was used to obtain a long-term overview of the frequency of the airmasses arriving over the measurement site. Average residence times covering the respective measurement periods for a reception height of 2 km are shown in Fig. 5.3, where each 3-hourly profile is binned according to ambient temperature.

A noteworthy feature at Leipzig is the predominance of European sources, with

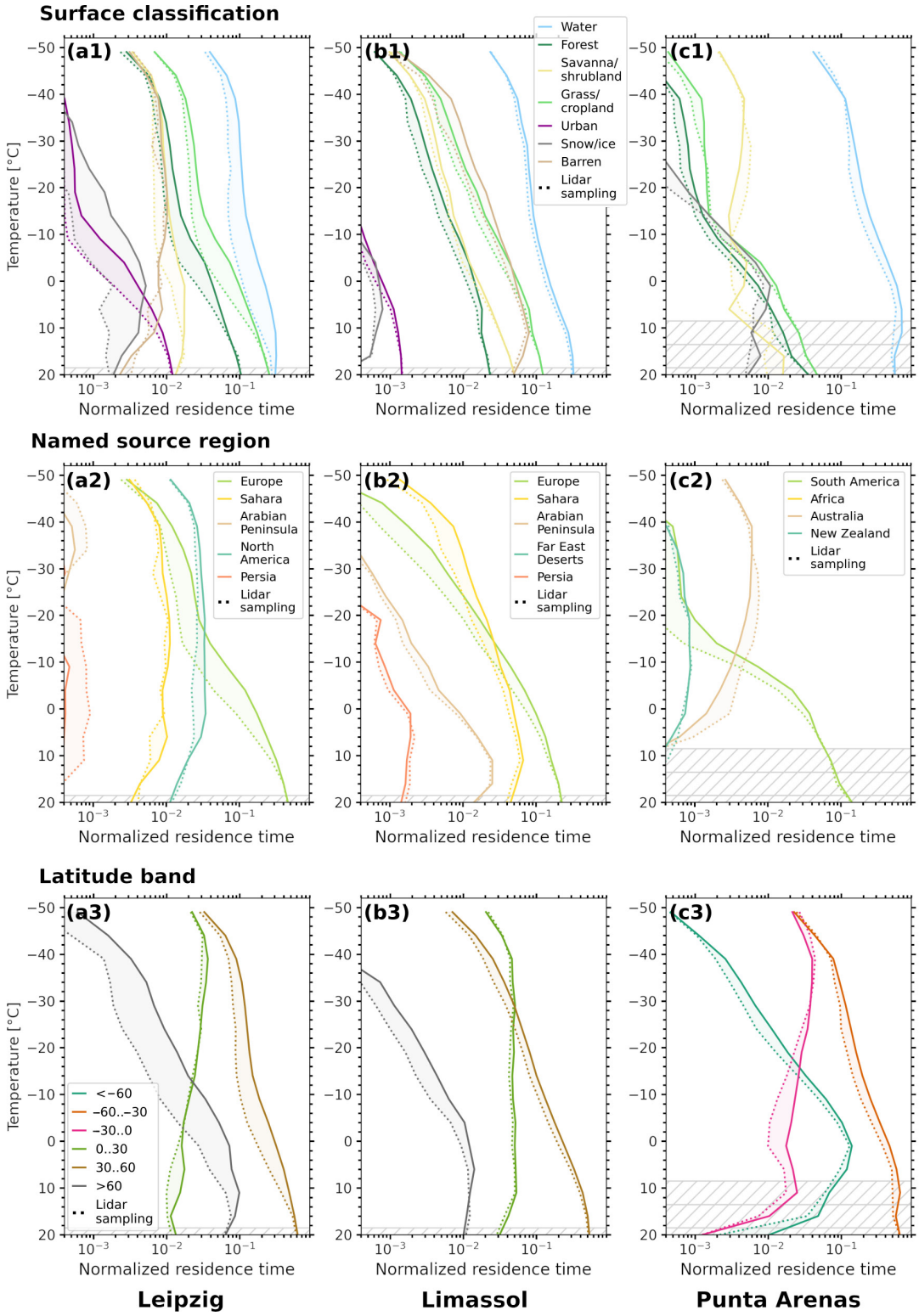

Figure 5.3: Mean normalized residence time binnend according to ambient temperature at (a) Leipzig, (b) Limassol, and (c) Punta Arenas for a reception height of 2 km. Columns show the residence time at each location for the (1) surface classification, (2) named source region, and (3) latitude bands. Dashed lines indicate the residence time only sampled for times, when lidar profiles were available. Hatching indicates bins with less than 1% of the values.

vegetated surfaces being the most frequent terrestrial sources. Airmasses from barren surfaces show a maximum between −10 and −40 °C, but contribute only less than 10% to the residence time. Above −30 °C, approximately 80% of the airmasses originate from the mid-latitudes (30–60°N), with air from high latitudes (> 60°N) being more frequent than from low latitudes (0–30°N) above −12 °C. Air from high latitudes does not contribute more than 23% at any temperature.

At Limassol, air from the Sahara and the Arabian Peninsula is more frequent. Saharan air shows the highest residence times of named source regions at temperatures below −15 °C, whereas Europe dominates at temperatures above. In terms of surface classification, water is the most dominant source followed by grass-/cropland above −10 °C and barren below. The mid-latitudes dominate above −29 °C and the low latitudes below.

At Punta Arenas, the water class dominates as an airmass source with relative contribution above 95% at all subfreezing temperatures. South America as terrestrial source contributes up to 10% between −10 and 0 °C. Below that temperature, long-range transport from Australia is the most important terrestrial source, increasing up to 5% at −40 °C. At temperatures of the heterogeneous freezing regime, airmasses from the mid-latitudes contribute between 65% and 80% to the mixture. Transport from the higher latitudes is the second most frequent source above −15 °C and peaks at 25%. At lower temperatures, air from the (southern) low latitudes increases in importance, with a 35% share at −40 °C.

All locations show the transition of predominantly local terrestrial sources to distant terrestrial sources at heights that correspond to temperatures between −12 and −17 °C. At Leipzig, this is the transition from Europe to North America as a source. At Limassol, the change is from Europe to Sahara and at Punta Arenas from South America to Australia. This pattern is visible in the meridional transport as well. At Leipzig and Punta Arenas, lower latitudes supersede polar airmasses as the second most frequent source between −12 and −17 °C. The mid-latitudies are the most important sources at these two locations.

The height-resolved statistics of aerosol optical properties is discussed in the following section. The retrieval of optical properties from lidar is only possible during cloud-free periods, which might introduce a sampling bias. As discussed in Radenz et al. (2021a), this sampling bias can be assessed with the residence-time analysis. The average profiles are subsampled for periods when lidar profiles are available and are compared with the averages of the full dataset. Generally, the sampling for all three campaigns is representative within a factor of 2 in the residence time. Notable exceptions are the undersampling of high-latitude airmasses at Leipzig and Limassol below 0 °C by a factor of 4 and 2, respectively. At Leipzig and Punta Arenas, Europe and South America as the respective local airmass source were undersampled by a factor of 2–4 between −7 and −30 °C. In summary, the lidar-derived average profiles of optical properties are quite representative for the respective location in terms of airmass source.

5.4 Aerosol optical properties

To provide a general insight into the aerosol conditions at the three sites, the average optical and microphysical aerosol properties as derived from the lidar observations (Sec. 4.2) are shown in Fig. 5.4. The impact of aerosol on clouds is controlled more strongly by temperature than geometrical height, hence the averages are also presented with temperature as a vertical coordinate. The average aerosol backscatter coefficient β_p at 532 nm and the particle linear depolarization ratio derived from the Polly^{XT} observations with the Klett method (see Sec. 4.2) are investigated in this section.

The central European site of Leipzig is characterized by predominantly continental aerosol mixed with anthropogenic pollution (Baars et al., 2016). Long-range transport of dust may occur periodically, especially during spring and autumn (Ansmann et al., 2003), as well as lofted smoke layers from wildfires (Haarig et al., 2018a; Baars et al., 2021). Mean AOT at 500 nm derived from sun-photometer observations at TROPOS, Leipzig, between 2014 and 2018 is 0.198. When only the periods with co-located Polly^{XT} observations (used in this study) are considered, the AOT is 0.216. Mean β_p at 532 nm drops below 0.2 $Mm^{-1}sr^{-1}$ only above 4 km height, which corresponds to an extinction coefficient of 1.0 Mm^{-1} assuming continental aerosol conditions and a corresponding lidar ratio of 50 sr.

As already shown in Sec. 5.2, Limassol is characterized by a distinct dry season with no precipitation and very few clouds during the summer. Generally, Limassol is frequently affected by aerosol transport from Africa, the Middle East, and Europe (Sec. 5.3) with aerosol characteristics including dust (mineral and soil), marine (organics and sea salt), and anthropogenic pollution as well as mixtures of these (Nisantzi et al., 2015). Mean AOT at 500 nm is 0.176 during the whole observational period and 0.165 during the 'cloudy season' from October to May. In the following, the non-cloud season from June to September is excluded from the statistics. The profile of mean backscatter is similar to the one at Leipzig within a factor of 1.5, whereas the median generally is higher at Leipzig.

The aerosol load at Punta Arenas can be separated into two distinct layers with an aerosol-rich boundary layer and pristine conditions aloft. The boundary layer is laden with a mixture of marine and continental aerosol, as Punta Arenas is located 230 km inland from the Pacific coast. Mean AOT at 500 nm is 0.055 during the whole campaign, but it drops to 0.047 when excluding the period of long-range wildfire smoke transport in early 2020 (Ohneiser et al., 2020). Average boundary layer height is around 1.5 km (Foth et al., 2019) with negligible β_p above 2.0 km height (90% percentile of β_p at 532 nm below 0.2 $Mm^{-1}\,sr^{-1}$). Comparing the backscatter at Punta Arenas and Limassol, the 90% percentile at Punta Arenas is more than 30% below the mean of Limassol and Leipzig at similar heights above ground. Both European sites show quite some variability as well, with the 90% percentile twice as large as the mean.

At temperatures above 5 °C, β_p shows the strongest difference between the three sites (Fig. 5.4b), which also explains the larger AOT at Limassol and Leipzig. Between 0 °C and −12 °C, the mean β_p at Limassol and Punta Arenas are almost equal.

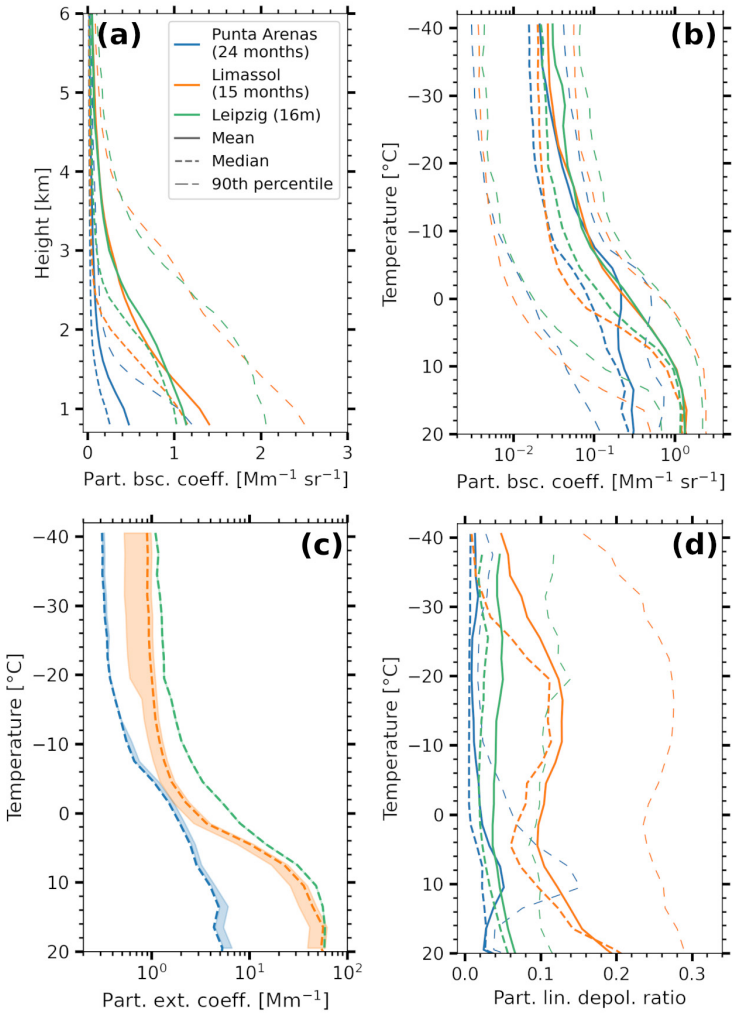

Figure 5.4: Profiles of average aerosol optical properties at 532 nm derived by the PollyNET retrieval using the Klett method. Particle backscatter coefficient over (a) height and (b) temperature for Leipzig, Limassol, and Punta Arenas. (c) Extinction coefficient and (d) particle depolarization ratio (d) for the same locations. For the extinction coefficient only the median values based on the typical lidar ratio at each site are shown. Variability caused by different aerosol mixtures at Limassol and Punta Arenas is denoted by shading in (c).

This counterintuitive behavior can be explained by different temperature regimes. The −5 °C isotherm at Punta Arenas varies between 1.1 and 3.3 km height, whereas at Limassol it varies between 3.0 and 4.8 km height (and at Leipzig between 2.1 and 4.8 km). At Punta Arenas, only very low values of β_p are observed at heights below a temperature of −10 °C, corresponding to the height of 2.0 km. The pronounced decrease of backscatter at Leipzig and Limassol is observed at slightly higher temperatures, which agrees with the, on average, higher boundary layer temperature there. Assuming typical lidar ratios of 50 (continental), 45 (dust), and 20 sr (marine) at Leipzig, Limassol, and Punta Arenas, respectively, typical aerosol extinction coefficients can be estimated from the median β_p profile (Sec. 4.2). As shown in Fig. 5.4c, the extinction coefficients at Punta Arenas are a factor of 2–3 lower than at Limassol for temperatures below −10 °C. This difference decreases to a factor of 1.5 for slight supercooling at temperatures of above −10 °C. Comparing Punta Arenas and Leipzig, the extinction is a factor of 3–4 higher at the latter site for all sub-zero temperatures. These optical properties serve as a proxy for the background reservoir of aerosol particles that could act as cloud condensation nuclei and ice nucleating particles in the free troposphere.

The particle depolarization ratio gives hints to the shape of the aerosol particles (Fig. 5.4d). At Leipzig, the mean linear depolarization ratio is approximately 0.05 at all temperatures, typical for a continental aerosol with a low contribution of mineral dust. The depolarization ratio at Limassol is bimodal, with one peak above 20 °C, a second one at −14 °C, and a minimum at 4 °C. The first peak can be ascribed to mineral dust in the boundary layer originating from local sources. The second one is caused by long-range transport of mineral dust. At Punta Arenas, a maximum at +8 °C is caused by occasional events of dried sea salt aerosol at the top of the atmospheric boundary layer (Haarig et al., 2017; Bohlmann et al., 2018). Going to lower temperatures, the depolarization ratio has a minimum of 0.01 at −20 °C and a slight increase afterwards.

5.5 Lidar-based estimate of INP profiles

An important aspect for the discussion of microphysical contrasts in clouds over the three sites is, how the differences in aerosol optical profiles are linked to contrasts in the INP load. An estimate of average INP concentrations covering the whole troposphere can be derived with the parametrizations described in Sec. 4.2.

The decision for the aerosol typing required in the INP retrieval is based on the particle depolarization ratio and airmass source estimates. At Punta Arenas marine sources are by far the most frequent, contributing 90% to the residence time throughout the troposphere with a peak of 95% at 2.7 km height. Only below 2.0 km height (or above −10 °C), local terrestrial sources contribute up to 10% of the airmass. Above 5 km height (below −20 °C), sparsely vegetated areas in Australia contribute up to 4% to the airmass source. Mean particle depolarization ratios below 0.02 in the free troposphere exclude frequent presence of mineral dust (Fig. 5.4d). Contrarily, at Limassol airmasses with a marine source contribute 50% to 80% to the mixture. However,

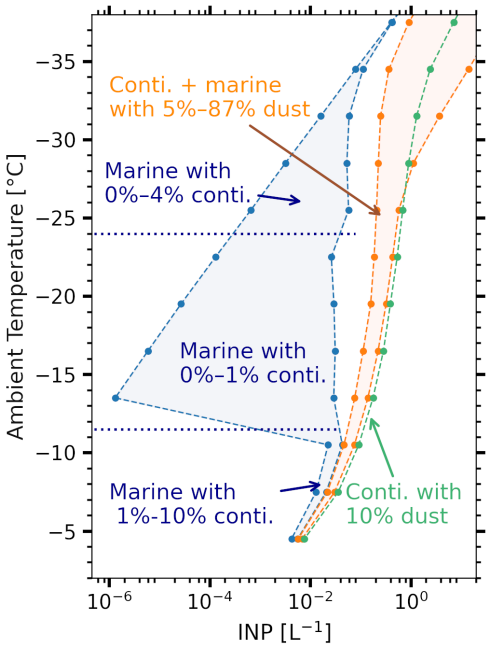

Figure 5.5: Average INP concentrations derived from optical properties for Leipzig (green), Limassol (orange), and Punta Arenas (blue). Shading shows the spread covered by different aerosol compositions, similar to Fig. 5.4c. Temperature is used as a vertical coordinate. The fraction of continental aerosol is abbreviated 'conti.'. The used parametrizations are described in Sec. 4.2.

these airmasses are not pristine marine, as the eastern Mediterranean is enclosed by densely populated landmasses with strong air pollution. Below 5 km height (above −16 °C), continental Europe is the second strongest source, contributing with up to 45% at 0.5 km height. In the upper troposphere, barren ground from the Sahara is the strongest terrestrial source with contributions of around 15%. The airmass source is in line with the aerosol optical properties. POLIPHON (see Sec. 4.2) analysis based on the linear depolarization ratio indicates a peak at −12 °C with mean dust fractions of 0.3 (90% percentile with a fraction of 0.87, not shown). Hence, the backscatter is divided into dust and non-dust according to the dust fraction. The non-dust portion is then split up into continental and marine, with 40% contribution of the continent above −12 °C and 20% below. The aerosol mixture at Leipzig is dominated by continental aerosol, with an average dust fraction of 0.1.

The derived INP concentrations are depicted in Fig. 5.5. Note that the INP concentration at a certain atmospheric temperature (as a proxy for height) is shown based on the optical properties, aerosol types, and the parameterization, not a freezing spectrum obtained from sampling a single air parcel and varying temperature.

At temperatures above −10 °C, average INP concentrations between 4×10^{-3} and $6 \times 10^{-2}\,\mathrm{L}^{-1}$ can be expected at all three locations. With decreasing temperatures, the concentration increases to 0.1–1 L^{-1} at −25 °C at the northern-hemispheric sites of Leipzig and Limassol. A strong increase of ice-nucleating efficiency with decreasing temperature is counterbalanced by a decreasing aerosol concentration at lower temperatures, which are tied to greater heights. INP concentrations at Punta Arenas are

strongly controlled by the fraction of continental aerosol in the free troposphere. Continental sources can contribute up to 1% between −11 and −24 °C and up to 4% at lower temperatures. When only pristine marine aerosol is present, the INP concentration is expected to be 3–4 orders of magnitude lower than at the two other sites. As soon as very small fractions of continental aerosol are present, the INP concentration increases significantly. However, even if a few percent of continental aerosol are assumed to be present throughout the heterogeneous freezing regime, INP concentrations remain a factor of 2–6 lower at Punta Arenas compared to Leipzig and Limassol. Due to the absence of suitable remote-sensing or in-situ measurements, the actual contribution of continental aerosol to the free-tropospheric aerosol load over Punta Arenas cannot be obtained to date. The range given in Fig. 5.5 is thus a reasonable estimate of the minimum and maximum of the expectable range of possible INP values. At temperatures above −10 °C, which refers to a height range that is frequently within the boundary layer, INP concentrations at Punta Arenas are high and, within an order of magnitude, comparable to the concentrations at the same temperature at Leipzig and Limassol. Concentrations that are similar to the ones retrieved from the remote-sensing observations above −10 °C were also found in situ at an up-wind hilltop station on Cerro Mirador at an altitude of 622 m above sea level (Gong et al., in preparation).

6 Properties of supercooled stratiform clouds

6.1 Overview on observed clouds

The automated cloud identification algorithm with the filter for stratiform clouds (Sec. 4.5) was used to evaluate the datasets from Leipzig, Limassol, and Punta Arenas. Fig. 6.1 provides an overview on all observed clouds that fulfill the criteria. In total, more than 2600 discrete cloud cases build the basis for the statistics presented in the second part of this chapter. Each of these automatically identified cloud cases can be seen as an automatized single-cloud case study. The automatically detected clouds from the case study in Fig. 4.3 are highlighted with red rectangles in Fig. 6.1c. The time share of ice virga sedimenting out of the liquid-dominated top is given by the fraction of profiles for which ice pixels were classified below the liquid layer. Values range from 0 (no ice virga observed at all) to 1 (ice virga observed all the time). At all three locations, the fraction of profiles showing an ice virga increases for decreasing temperature. This finding is straightforward, because the temperature is the dominant constraint for ice formation in a liquid layer. Similarly, the ice-to-liquid content ratio increases for lower temperatures (colors in Fig. 6.1). Liquid-only clouds (fraction of profiles for which no ice was produced from the liquid layer, indicated by grey dots in Fig. 6.1) were observed at Leipzig and Limassol down to $-20\,^{\circ}\mathrm{C}$, whereas at Punta Arenas such clouds were observed even at temperatures as low as $-38\,^{\circ}\mathrm{C}$.

Starting from this overview, three case studies are presented in more detail in Sec. 6.2. These case studies are selected to illustrate features that emerge in the statistical analysis presented in the subsequent sections of this chapter.

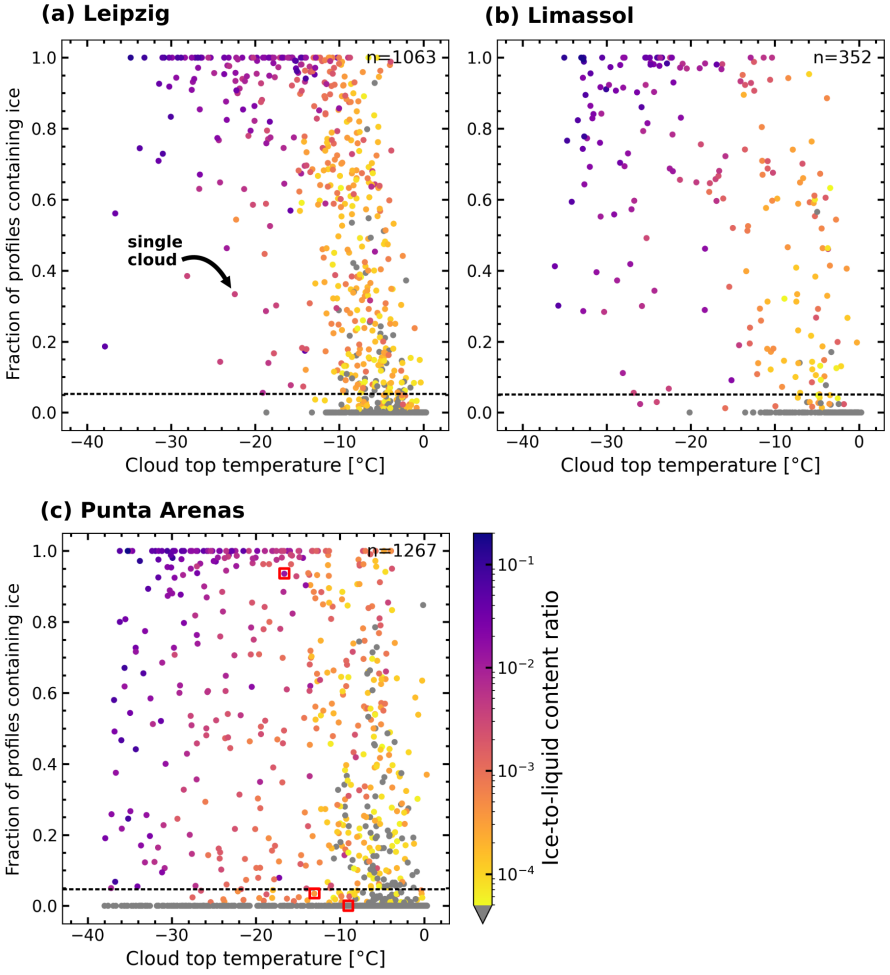

Figure 6.1: All supercooled stratiform clouds identified by the automated cloud identification algorithm for (a) Leipzig, (b) Limassol, and (c) Punta Arenas in terms of their cloud top temperature and the fraction of profiles for which ice is observed below the liquid-dominated cloud top. The 0.05 threshold for the classification is marked by a dashed line. Colors indicate the median ice-to-liquid content ratio. Red rectangles in (c) denote the clouds also marked in Fig. 4.3. n gives the number of cloud cases in each dataset.

6.2 Case studies

6.2.1 Punta Arenas, 4/5 September 2019: stratiform cloud with variable ice formation

The stratiform cloud discussed in this case study covers periods of weak and strong ice formation, illustrating the observational capabilities of lidar and cloud radar. An anticyclone dominated the synoptic situation at Punta Arenas on 4 September 2019. Its core was located west of the continent at approximately 52°S, 85°W and a weak pressure gradient prevailed. Surface winds were also weak and mostly from southerly directions. Source of the free-tropospheric airmass, estimated from 10-day backtrajectories, was the tropical western Pacific Ocean. During the day, an aerosol optical thickness of 0.069 at 500 nm was observed, while it was 0.046 on the following day. Fig. 6.2 shows the observation of a stratiform supercooled cloud layer, which formed under these conditions and was present over the LACROS site between 16:30 UTC on the 4^{th} and 03:00 UTC on the 5^{th} September.

The liquid layer at cloud top was constantly sustained at 3.9 km height. CTT steadily increased from −14.5 to −11.5 °C. The ice virga sedimenting out of the mixed-phase layer had its base between 2.3 km and 3.2 km height. During the first four hours, ice production was rather strong (maximum reflectivity −3.0 dBZ), whereas later on much lower values of reflectivity were observed. In terms of ice water content, the values in the virga dropped from $2.5 \times 10^{-5}\,\mathrm{kg\,m^{-3}}$ to below $3.0 \times 10^{-7}\,\mathrm{kg\,m^{-3}}$. Notable exception is a period from 00:30 to 02:00 UTC during which a second liquid layer at 3.5 km height was observed by lidar below the cloud top layer. The bimodal structure of the cloud radar Doppler spectra during this time supports the interpretation of a second liquid layer (Fig. 6.2f). Liquid-water paths well below $20\,\mathrm{g\,m^{-2}}$ were observed until 22:00 UTC. Slightly more liquid water, exceeding $50\,\mathrm{g\,m^{-2}}$, was present when the dual-layer structure was observed.

The properties of the ice crystals formed are further investigated with the lidar-radar version of the manual retrieval of ice crystal number concentration proposed by Bühl et al. (2019b). At 19:30 UTC, in the virga with high reflectivity and backscatter, particle size was estimated to 0.8–1.4 mm, yielding number concentrations of 300 to $1000\,\mathrm{m^{-3}}$. Later, between 23:10 and 23:50 UTC, the ice particles were smaller (≈ 0.7 mm) and less frequent with number concentrations of 7–$10\,\mathrm{m^{-3}}$. In this period, the virga was not detectable anymore in the lidar signal with high temporal resolution.

This case study illustrates two aspects that guided the statistical analysis: (1) ice formation and ice-to-liquid content ratio of individual clouds are too variable to be compared on a case-by-case basis; (2) even if no ice formation is visible in the lidar observations, ice might be formed and only be detected due to the superior sensitivity of the cloud radar, as outlined by Bühl et al. (2013a).

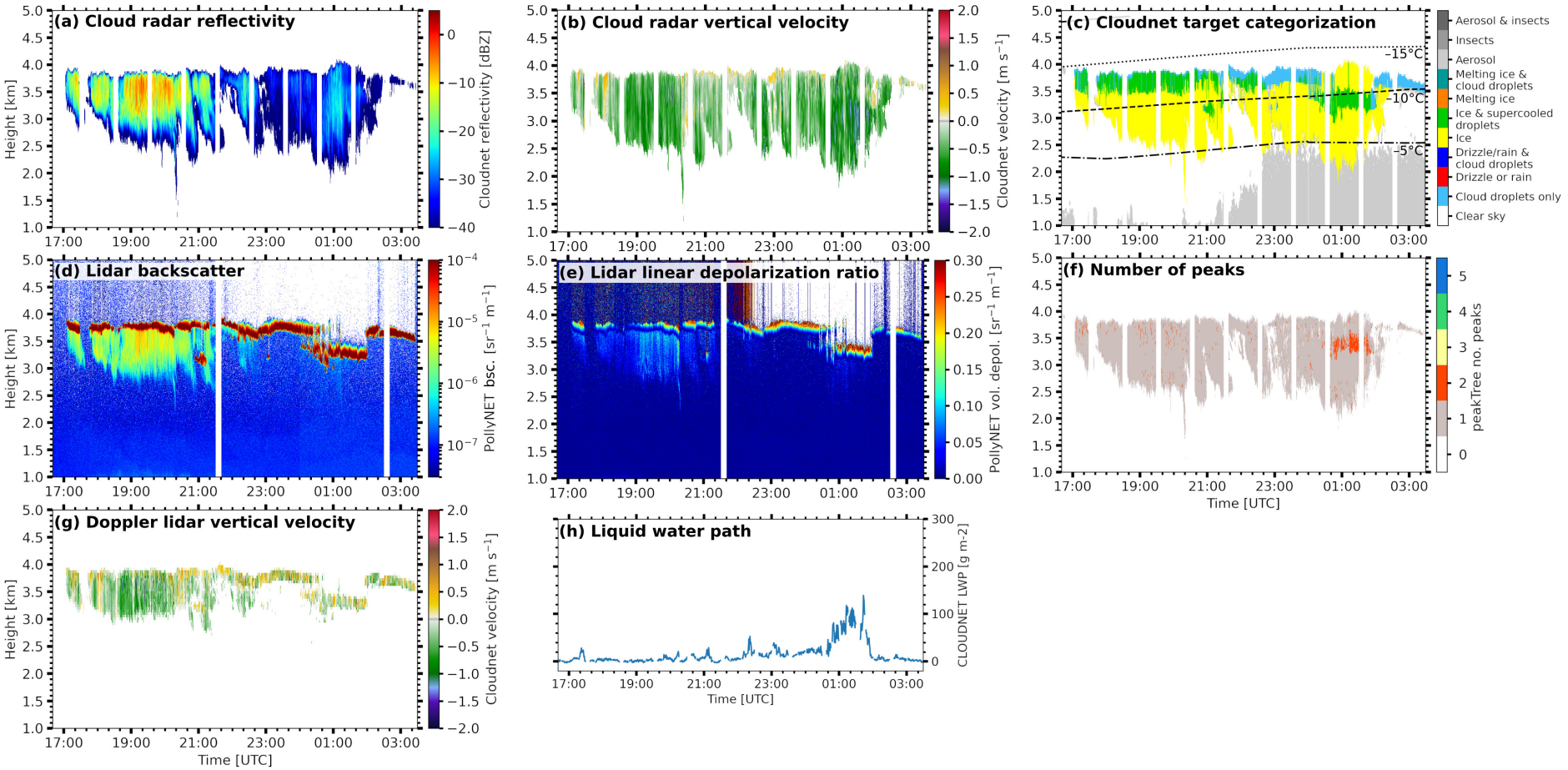

Figure 6.2: Stratiform mixed-phase cloud observed between 4 September, 16:30 UTC, and 5 September 2019, 03:00 UTC. (a) Cloud radar reflectivity, (b) cloud radar vertical velocity, (c) Cloudnet target categorization with temperatures, (d) lidar attenuated backscatter, (e) lidar linear volume depolarization ratio, (f) peakTree number of peaks, (g) Doppler lidar vertical velocity, and (h) MWR-derived liquid-water path.

6.2.2 Punta Arenas, 27 September 2019: Wave cloud

As discussed in Chapter 2, the vertical dynamics are a key driver of glaciation processes in mixed-phase clouds. Updrafts in stationary or slowly propagating gravity waves can sustain liquid layers at temperatures down to −37 °C, without showing signatures of sedimenting ice crystals to the fixed observer. Such a wave cloud observed at Punta Arenas is discussed in this case study. On 27 September 2019, a mid-tropospheric long-wave ridge was located above southern South America. Above Punta Arenas, a strong zonal, westerly flow was present, exceeding 25 m s^{-1} at 4000 m height. As it becomes clear from the ECMWF reanalysis data in Fig. 6.3, the flow triggered strong gravity waves in that area. The waves in the upper troposphere were moving westward against the mean flow and weakened slowly.

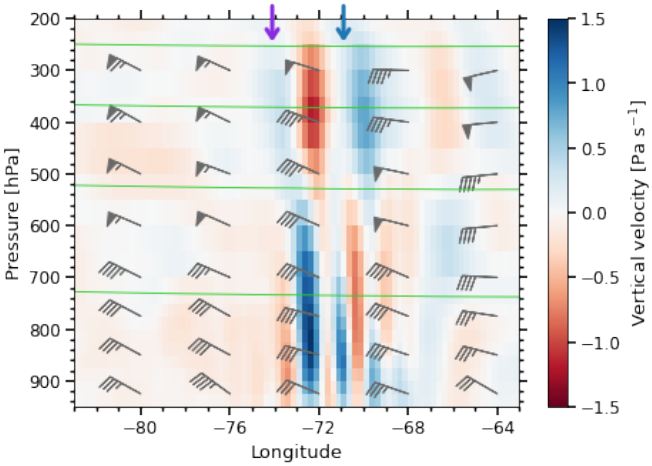

Figure 6.3: Vertical cross section along 53.25°S on 27 September 2019, 06:00 UTC. Color depicts the ECMWF reanalysis (v5) vertical velocity. Wind barbs indicate speed and direction in knots. Green lines indicate the geopotential height in intervals of 2.5 km. The longitude of Punta Arenas is marked with a blue arrow and the Pacific coast with a purple one.

Before 07:00 UTC stratiform clouds formed at several levels between 3000 and 12000 m height. Vertical velocities in those clouds were impacted by gravity waves to varying degrees. One of the layers is depicted in detail in Fig. 6.4. It serves as a good example for the horizontal separation of cloud phase in wave clouds and was already briefly discussed in Sec. 4.6. Cloud top height and thickness of the cloud layer were rather uniform with values of 7100 m and 250 to 350 m, respectively. CTT was between −34 and −31 °C. Embedded in a slowly propagating gravity wave, the cloud was advected over the site and the full life cycle could be observed. Based on the Doppler lidar vertical velocity (Fig. 4.5a), the updraft was present until 05:32 UTC. Afterwards, downward motion with increasing velocity set in. This interpretation is also in agreement with the reanalysis data, where vertical velocities at 06:00 UTC at the respective altitude are slightly negative. Throughout the observation, the vertical-velocity autocorrelation remained high. Liquid droplets dominated the lidar signal between 05:10 and 06:17 UTC (Fig. 6.4a). After 06:17 UTC the cloud layer solely consisted of ice particles for a period of 15 minutes, as it is evident from the reduced

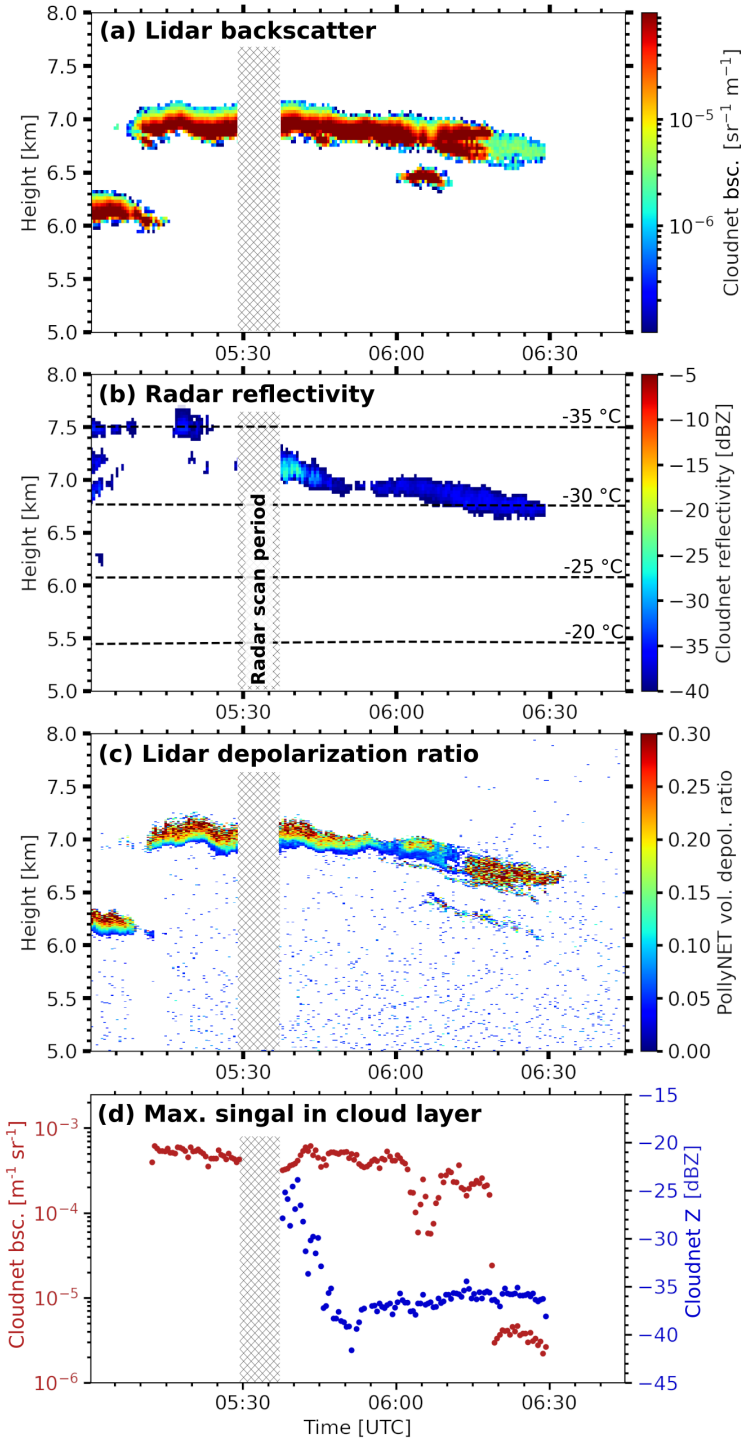

Figure 6.4: Wave cloud observed at Punta Arenas on the 27 September 2019, 05:00–06:45 UTC. (a) Lidar attenuated backscatter, (b) cloud radar reflectivity, (c) lidar volume linear depolarization ratio, and (d) maximum of the signal in the cloud layer.

backscatter coefficient and the increased linear depolarization ratio. Only this last part of the cloud is classified as ice by the Cloudnet classification scheme (Fig. 4.5b). However, there are indications that ice formation actually already happened as early as 05:47 UTC. Sudden freezing of droplets is associated with a rapid drop in the radar reflectivity by 7 dB, as the dielectric constant of ice is a factor of 5 lower than that of liquid water. From 05:47 UTC onwards the radar reflectivity remained more or less constant (Fig. 6.4d), especially no change occurred, when the ice particles became visible in the lidar signal. Very likely, the ice phase already existed in the cloud before, but it was masked in the lidar linear depolarization ratio by the strong scattering by droplets. During the period between 05:37 and 05:47 UTC, radar reflectivity dropped from -23 to -38 dBZ, but no similarly clear argument on cloud phase can be derived. One possible explanation is the co-existence of ice and liquid water, with large droplets dominating the radar and the lidar signals. When the vertical velocity is not longer sufficient to sustain the liquid phase, the WBF process sets in. The droplets shrink or freeze (as discussed in Sec. 4.6) and the ice particles dominate the radar signal. This observation is in good agreement with the theoretical treatment of Chapter 2. The updraft is strong enough to activate and sustain the liquid phase, but rapid glaciation occurs as soon as the downdraft begins. For a downward velocity larger than $-1.2\,\mathrm{m\,s^{-1}}$, theoretical glaciation times are less than 200 s (Fig. 2.3). Similar patterns of the ice phase, occurring in sustained downdrafts only, are frequently observed by in-situ observations of wave clouds (Fig. 4.4).

6.2.3 Punta Arenas, 12 June 2019: Surface coupling

Recent studies provide increasing evidence that coupling to the aerosol-rich boundary layer and thus also to the surface increases the frequency of ice formation (e.g., Griesche et al., 2021). As shown by the averaged profiles of aerosol optical properties (Sec. 5.4), there is a strong contrast in aerosol load between the boundary layer and the free troposphere at Punta Arenas. The clouds observed at Punta Arenas on 12 June 2019 are an illustrative example for the coupling effect. An upper-level long-wave trough with weak gradients developed a cut-off low above the Pacific Ocean north-west of Punta Arenas. In the lowermost 3.0 km, weak north-easterly winds prevailed during the day and caused warm-air advection. Above 1.5 km height, the temperature increased by roughly 4 K. During the first five hours depicted in Fig. 6.5, a cloud at boundary-layer top with CTT of $-13\,^{\circ}\mathrm{C}$ formed ice. The signature of the volume linear depolarization ratio below cloud base (Fig. 6.5d) is a clear indicator for the ice phase being present. However, only parts of that cloud system (Fig. 6.5, number 1) suffice the criteria of the automated cloud selection scheme, as posed in Sec. 4.5. Above cloud base, the increase in depolarization ratio can be attributed to multiple scattering (see, e.g., Jimenez et al., 2020b). With increasing temperature, ice formation in the cloud layer at boundary-layer top ceases. After 17:45 UTC, a stratiform liquid-only cloud with a CTT of $-13\,^{\circ}\mathrm{C}$ was observed (Fig. 6.5, number 2). At heights above 2500 m, this cloud was clearly decoupled from the boundary layer (Fig. 6.5a).

Cloud cases that are conform with the cloud selection criteria defined in Sec. 4.5

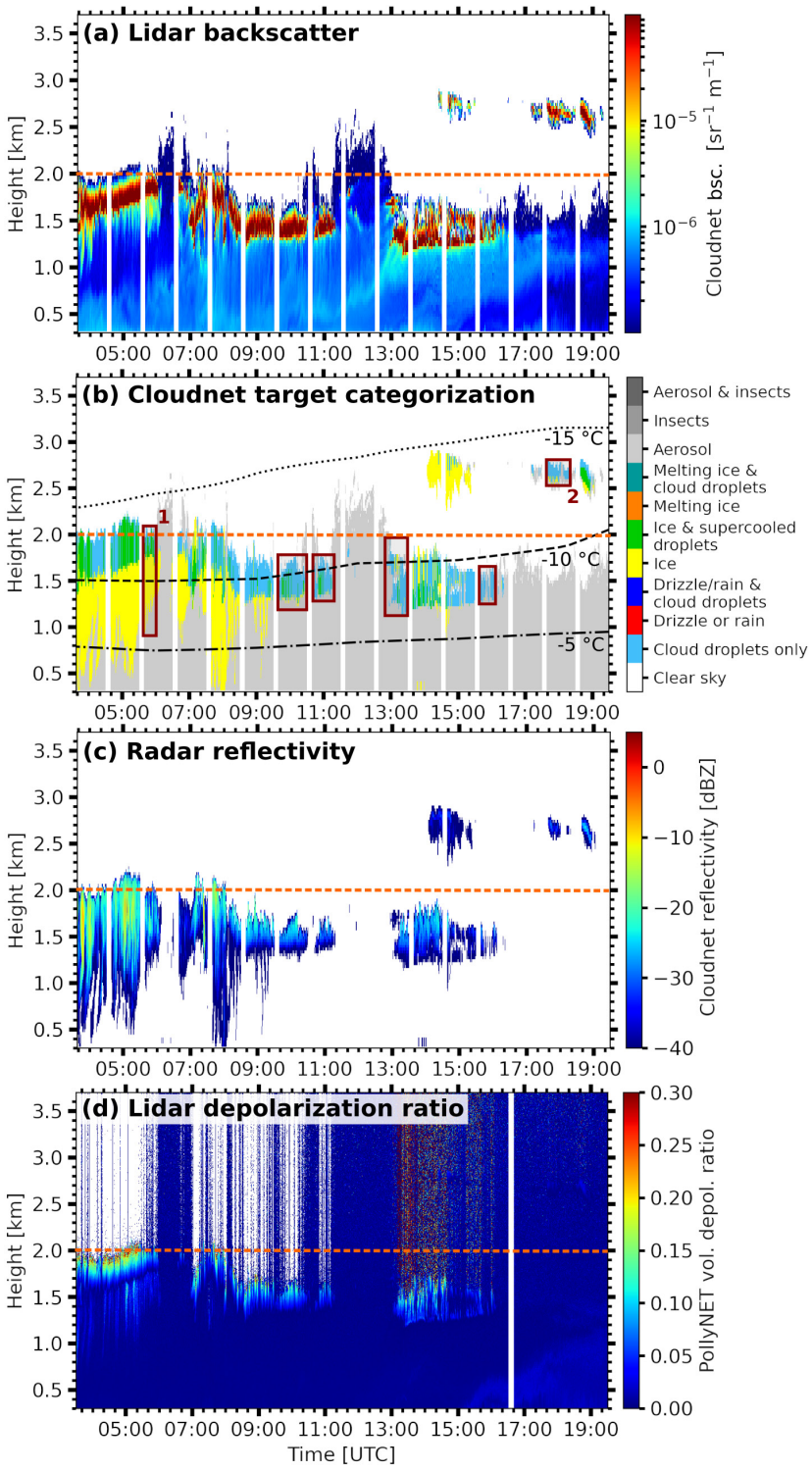

Figure 6.5: Stratiform clouds at boundary-layer top and in the free troposphere on 12 June 2019. (a) Lidar attenuated backscatter, (b) Cloudnet target categorization with model-derived temperature, (c) cloud radar reflectivity, and (d) lidar volume linear depolarization ratio. Cloud cases that match the selection criteria of the automated cloud selection scheme are marked with rectangles in (b).

are marked in Fig. 6.5b. Furthermore, this case study also features clouds, for which no clear phase classification is currently possible. For example, the short virga at 8 and 9 UTC and the cloud base at 18:50 UTC are classified as ice by Cloudnet target classification, though this is not supported by the depolarization characteristics. A statistical analysis of the coupling effects at Leipzig, Limassol, and Punta Arenas using all cloud cases follows in Sec. 6.5. For this statistics, the Cloudnet classification is considered authoritative, however, more focus will be needed in future to discriminate supercooled drizzle and ice formation under slightly supercooled conditions.

6.3 Phase occurrence frequency

After focusing on single case studies in the previous sections, the remainder of this chapter deals with the mixed-phase cloud properties across the full dataset, based on the cloud cases identified by the automatic identification scheme (Sec. 4.5) as shown in Sec. 6.1. First, the temperature-resolved fraction of occurrence of ice-forming clouds is depicted in Fig. 6.6. Comparing the frequency of ice-containing clouds at different locations provides insights into differences of primary ice formation (Choi et al., 2010; Kanitz et al., 2011; Seifert et al., 2015; Tan et al., 2014; Zhang et al., 2018; Alexander and Protat, 2018). For the phase occurrence frequency, a cloud is classified as ice-producing, if an ice virga was observed at least during 5% of the duration of a single cloud case. Temperature bins containing less than eight cloud cases are not considered in the statistics.

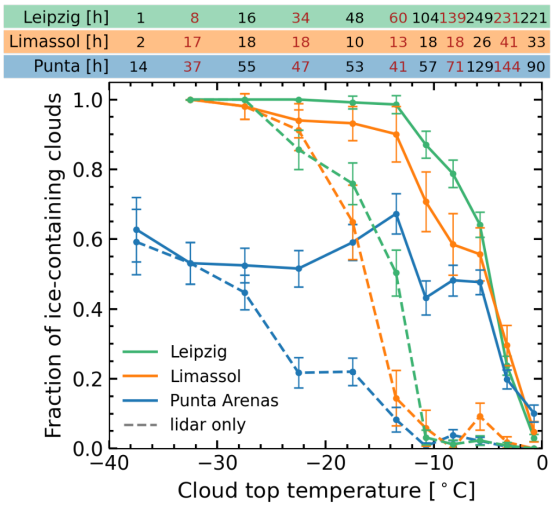

Figure 6.6: Fraction of ice-containing clouds over temperature for Leipzig, Limassol, and Punta Arenas. Total duration of the clouds in each bin is given by the numbers on top in hours. Dashed curves mark the occurrence frequency when using a lidar detection threshold of $12\,\mathrm{Mm}^{-1}$.

Generally, Fig. 6.6 (solid lines) shows that clouds contain ice more frequently for decreasing temperature. While at Leipzig and Limassol all clouds with CTT below $-16\,°\mathrm{C}$ contained ice, at Punta Arenas a fraction of 0.3−0.5 of shallow stratiform clouds were classified as liquid-only even below $-20\,°\mathrm{C}$. Such a behavior is in disagreement

with prior findings in the studies cited above with respect to several aspects: (1) a higher frequency of ice formation is found compared to lidar-only studies above −14 °C; (2) additionally at these temperatures, differences between the locations are masked by coupling to the surface; (3) strong contrasts for temperatures below −20 °C due to stationary wave clouds are obtained. Each of these points is discussed in the following three sections (6.4, 6.5, 6.6), before a revised statistics of frequency of ice-containing clouds is presented in Sec. 6.7.

6.4 Context to lidar-only observations

Compared to prior lidar-based studies (e.g., Kanitz et al., 2011; Choi et al., 2010; Seifert et al., 2010; Alexander and Protat, 2018), the fraction of ice-containing clouds in the synergistic dataset is higher at temperatures above −10 °C. At these temperatures, the amounts of ice produced and hence the optical extinction and radar reflectivity are generally very low and thus the ice remains undetected by lidar (Bühl et al., 2013a) and spaceborne radars (Bühl et al., 2016). To quantify a lidar detection threshold in terms optical extinction, the reflectivity-to-IWC and the reflectivity-to-extinction relationships by Hogan et al. (2006) are used. The only additional information needed for both parametrizations is the ambient temperature. Using these relationships, the response of the occurrence statistics to arbitrary extinction detection thresholds α_{thres} can be tested. When the retrieved extinction is below α_{thres}, the corresponding cloud is re-classified as liquid-only. In an attempt to reproduce the lidar-only ice-formation occurrence statistics for Punta Arenas and Leipzig reported by Kanitz et al. (2011), a value of $\alpha_{\text{thres}} = 12\,\text{Mm}^{-1}$ was identified, for which the lidar-radar statistics from this study agrees best to the lidar-only results. The resulting curves for ice-containing clouds below α_{thres} set to pure liquid are shown in Fig. 6.6 (dashed lines). By using the parametrization of Hogan et al. (2006), this threshold is independent of the lidar systems used in this study. The extinction threshold translates to a β_{p} of $0.6\,\text{Mm}^{-1}\,\text{sr}^{-1}$, a backscatter coefficient which is hardly observable at a temporal resolution of 30 s needed for the classification scheme. This result is of importance for lidar-only or ceilometer datasets, which are currently used for validation of climate models (e.g., Kuma et al., 2020). The occurrence of ice at these relatively warm temperatures of $> -10\,°\text{C}$ is also in line with airborne in-situ observations over the Southern Ocean (Huang et al., 2017; D'Alessandro et al., 2019).

6.5 Effect of boundary-layer aerosol load on phase occurrence

In this section, it is investigated whether contact of a cloud layer to the aerosol-rich boundary layer obscures the contrasts between different sites under slightly supercooled conditions (i.e., above −10 °C). As discussed in Sec. 5.4, the aerosol load at Punta Arenas is confined to the lowermost 2 km. This boundary-layer aerosol load is comparable to the aerosol load at temperatures above −10 °C at Limassol. To check for a possible impact of the boundary-layer aerosol on the ice formation efficiency,

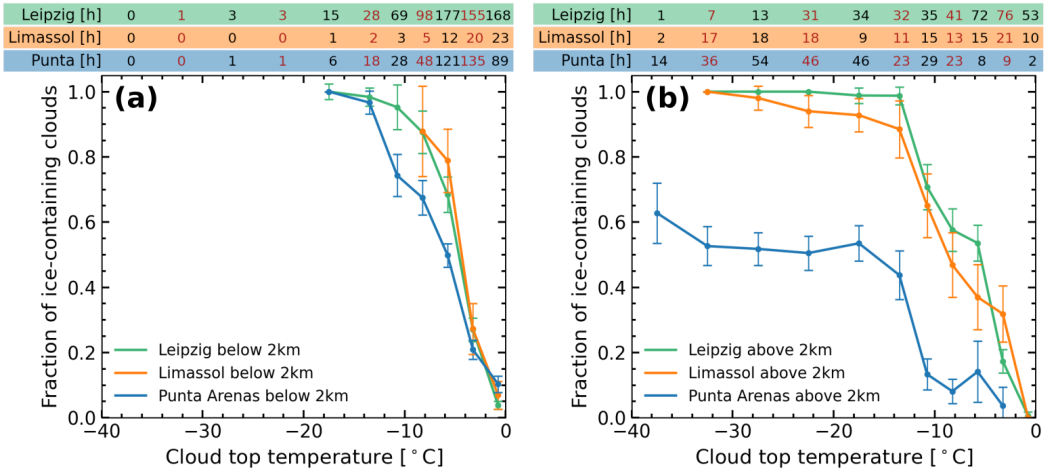

Figure 6.7: Fraction of ice-containing clouds over temperature for Leipzig, Limassol, and Punta Arenas, separately for clouds with bases (a) below 2 km, and (b) above 2 km. Total duration of the clouds in each bin is given by the numbers on top in hours.

the basic temperature-resolved phase occurrence frequency (Fig. 6.6) is split into two, one containing cloud cases with bases below 2 km height and one with cloud cases having bases above that threshold (Fig. 6.7), in the following denoted as coupled and uncoupled clouds, respectively. At any height, temperatures vary by more than 11 K (10% to 90% percentile), providing reasonable coverage for clouds above and below the height threshold. Generally, coupled clouds show higher fractions of ice (the absolute difference increases by 0.3 at −8 °C at all locations). The temperature-resolved phase occurrence frequency for the coupled clouds shows a rapid increase in fraction of ice-containing clouds, reaching 1.0 at temperatures of only −15 °C (Fig. 6.7a). The absolute difference between the fractions is less than 0.2, with the lowest fractions still being observed at Punta Arenas. Below −15 °C, almost no clouds were observed at heights below 2 km, especially at Limassol. Hence, no meaningful comparison can be done for colder temperatures. Considering only uncoupled clouds (Fig. 6.7b), stronger contrasts become evident. The fractions are similar at Leipzig and Limassol, but are 0.15 to 0.5 lower for temperatures above −10 °C at Punta Arenas.

Despite this extremely simple approach for discriminating into surface-influenced and free-tropospheric clouds, similar results were also found at other locations. In particlualr, more frequent ice formation for surface-coupled clouds was reported for the Arctic. Achtert et al. (2020) observed high fractions of ice-producing clouds in the boundary layer of the Arctic Ocean during summer. Also, Griesche et al. (2021) show that surface coupling increases the frequency of ice formation in boundary-layer clouds observed during Arctic summer.

6.6 Gravity-wave influence on phase occurrence at low temperatures

The lack of ice-containing cloud layers at temperatures below −18 °C over Punta Arenas is a prominent feature of both the lidar-radar and the lidar-only-equivalent datasets shown in Fig. 6.6. The associated excess of supercooled liquid water is frequently reported as a general phenomenon of stratiform clouds in the mid and high latitudes of the southern hemisphere. Within this subsection, the reasons for the observed behavior over Punta Arenas are elaborated in more detail.

Triggered by empirical observations, such as presented in Sec. 6.2.2, the vertical-velocity autocorrelation method (Sec. 4.6) is used to screen the cloud dataset for wave clouds. Fig. 6.8 shows the autocorrelation and power spectra of the Doppler lidar vertical velocity for clouds classified as liquid-only over Leipzig, Limassol, and Punta Arenas. Supercooled liquid-only clouds with CTT below −18 °C at Punta Arenas show high autocorrelation coefficients at long shifts (Fig. 6.8c1), whereas liquid-only clouds with similar characteristics are practically absent at Limassol (Fig. 6.8b1) and Leipzig (Fig. 6.8a1). In terms of spectral power density (Fig. 6.8c2), the strongly supercooled clouds at Punta Arenas show only low turbulence, whereas ice-forming clouds (Fig. 6.8, row 3 and 4) show no clear pattern of CTT and vertical-velocity characteristics. Strong indication is given that the stratiform liquid-only cloud layers observed at temperatures below −18 °C over Punta Arenas are frequently embedded in orographic gravity waves.

In a next step, the autocorrelation is used to filter the dataset for clouds affected by gravity waves. As described in Sec. 4.6, the length at which the autocorrelation coefficient drops below 0.8 is used as a characteristic value. Decreasing threshold value for this characteristic length will remove gravity-wave influenced clouds from the dataset. For large values of the length threshold, e.g., larger 1000 m, only clouds that are strongly forced by gravity waves will be removed, whereas going to shorter thresholds (< 500 m) will also remove weakly gravity-wave-influenced clouds. Fig. 6.9 shows an increase in the fraction of ice-containing clouds below −12 °C with decreasing correlation-length thresholds from 30 000 to 300 m. At Punta Arenas, the fraction of ice-containing clouds increases from 0.5 to 0.85. In the temperature interval between −15 and −25 °C, the fraction is 0.05 to 0.1 lower at Punta Arenas compared to Leipzig and Limassol. Hence, clouds with fully developed turbulence show similar ice-formation frequencies, independent of the location, with indications for a still slightly reduced ice-formation efficiency over Punta Arenas.

The autocorrelation-based analysis revealed that at temperatures below −14 °C, approximately one-third of the cloud layers observed at Punta Arenas were influenced by gravity waves. Similar frequencies of occurrence of non-turbulent liquid layers were also found at Utqiaġvik (Alaska) and McMurdo (Antarctica), based on radiosounding-derived stability criteria (Silber et al., 2020).

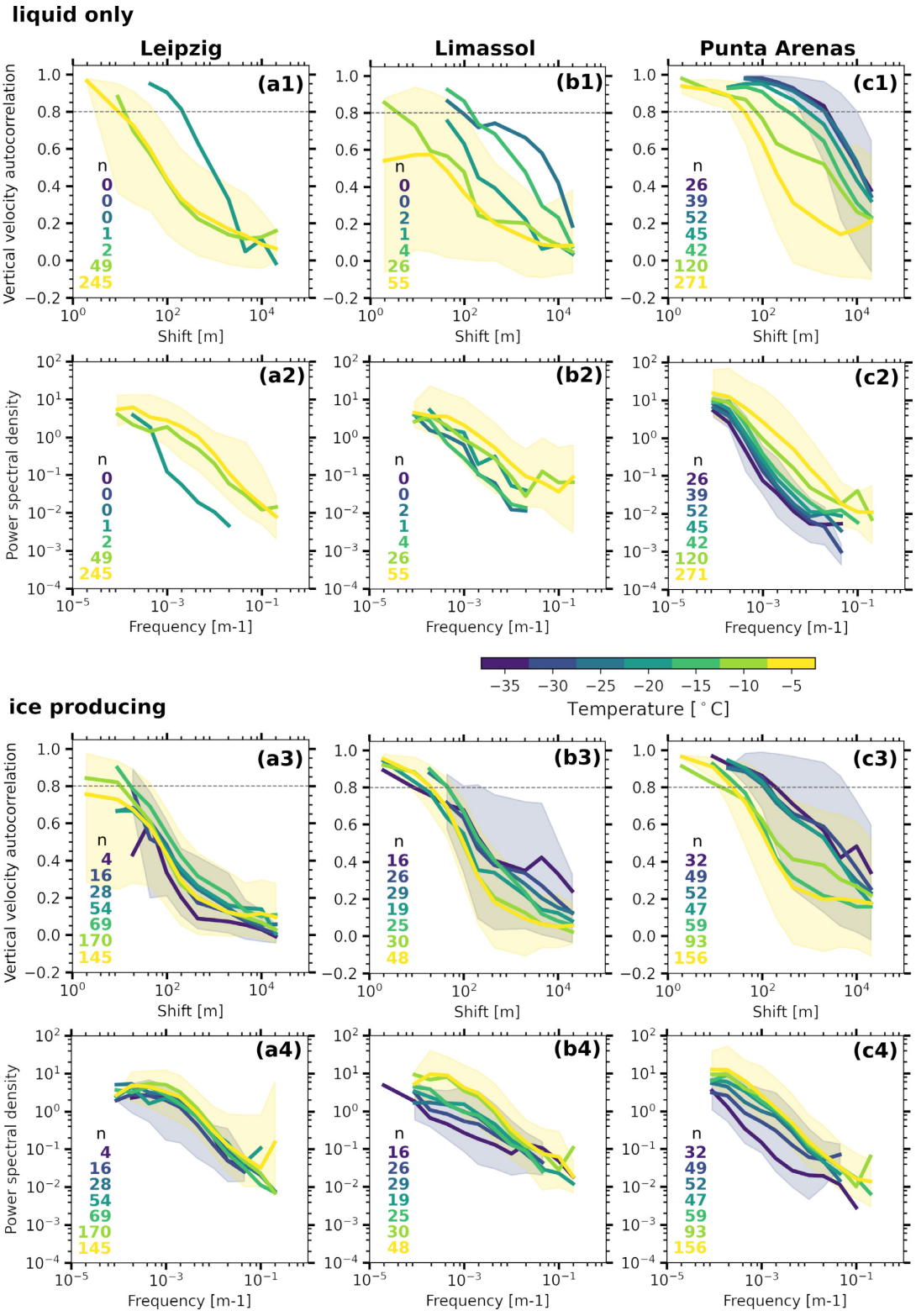

Figure 6.8: Vertical-velocity autocorrelation function (row 1 and 3) and power density (row 2 and 4) of the Doppler lidar vertical velocities for cloud cases classified as liquid-only (row 1 and 2) and ice-producing (row 3 and 4). The columns are (a) Leipzig, (b) Limassol, and (c) Punta Arenas. The curves are binned to CTT intervals of 5 K with color indicating the CTT. The number of clouds for each temperature interval is given as numbers in the respective panel. Shading denotes the 10%-90% percentile range for the −5 and −30 °C bin.

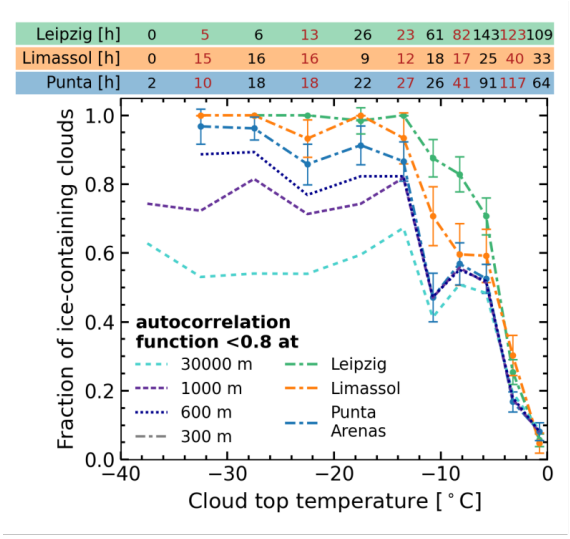

Figure 6.9: Fraction of ice-containing clouds over temperature for Leipzig, Limassol, and Punta Arenas. Dash-dotted lines show the fractions for Leipzig, Limassol, and Punta Arenas with an autocorrelation coefficient smaller than 0.8 for a horizontal shift of 300 m. The fractions for cloud cases with longer autocorrelation are only shown for Punta Arenas. Total duration of the clouds in each bin is given by the numbers on top in hours.

6.7 Ice-formation frequency of free-tropospheric and fully turbulent clouds

In a final step, the separation techniques for coupling and orographic waves are combined to assess contrasts in ice frequency for free-tropospheric and fully turbulent clouds. The resulting occurrence frequency is shown in Fig. 6.10. The fraction of ice-containing clouds at temperatures below −15 °C is above 0.85 at all three sites. Negligible changes compared to Fig. 6.6 were obtained for Limassol, where both boundary-layer coupling at subfreezing temperatures and gravity-wave occurrences were rarely observed. The Leipzig dataset shows only weak changes in the low-temperature range, because also there gravity waves affected the observed clouds only rarely. At temperatures > −15 °C, some boundary-layer-coupled clouds were removed from the combined statistics, which brings the frequency at Leipzig close to the one of Limassol. At Punta Arenas, correction for both gravity waves and boundary-layer coupling has a large impact on the resulting ice frequency. A lower frequency of ice formation in free-tropospheric and fully turbulent clouds at temperatures above −15 °C is obtained at the southern-hemisphere mid-latitude site. Almost no ice-containing free-tropospheric clouds were observed at temperatures > −10 °C. Without coupling to the near-surface aerosol reservoir, ice formation is strongly suppressed compared to Leipzig and Limassol. However, also the fraction of ice-forming clouds with CTT between −25 and −15 °C remains a fraction of 0.1 lower at Punta Arenas. Also this difference can be explained by a lack of INP. Mineral dust is known to be an efficient INP at these temperatures (Kanji et al., 2017), but was not observed at the respective temperatures at Punta Arenas (Fig. 5.4). The difference in the non-wave-cloud phase occurrence is also in agreement with satellite-based studies of Villanueva et al. (2020), who also

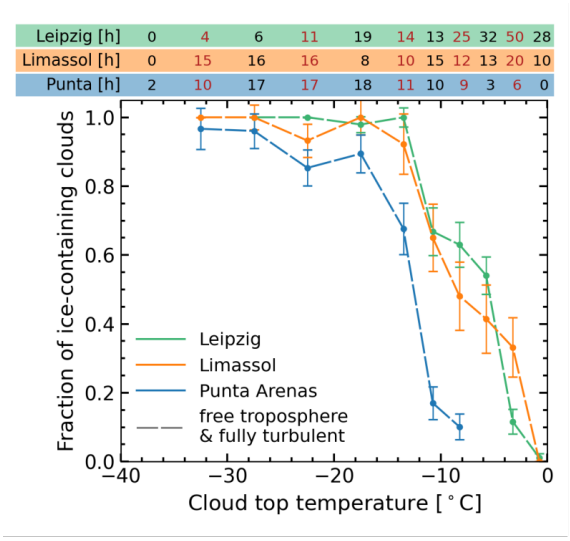

Figure 6.10: Fraction of ice-containing clouds over temperature for Leipzig, Limassol, and Punta Arenas when considering only fully turbulent clouds with an autocorrelation coefficient smaller than 0.8 for a horizontal shift of 300 m (see Fig. 6.7) and cloud bases in the free troposphere above 2 km height (see Fig. 6.9).

attributed latitudinal differences in the ice occurrence to associated differences in the dust load.

6.8 Contrasts of radar reflectivity factor in the ice virga

So far, only the occurrence frequency of ice formation in stratiform clouds was investigated. Quantification of the formed ice mass is more challenging (Zhang et al., 2014; Bühl et al., 2016; Zhang et al., 2018). For the basic analysis conducted in the following, an approximation defined by Hogan et al. (2006) is utilized, stating that for temperature intervals of a few K, ice mass is directly proportional to radar reflectivity. For comparability to existing satellite studies, the radar reflectivity is used. Prior studies of Zhang et al. (2018) identified a strong contrast in radar reflectivity factor between the different 30-deg latitude bands of the globe, with the southern mid-latitudes (30–60°S) showing the lowest mean reflectivity of all regions. They concluded that this difference in reflectivity factor is associated with a respective difference in ice-crystal mass and number concentration. In the following, a similar representation of regional contrasts of ice-virga reflectivity from a ground-based perspective is presented. Also, the stability of the mixed-phase layers is discussed in terms of the ice-to-liquid content ratio (Korolev and Field, 2008; Bühl et al., 2016), which is a measure for the efficiency with which water is converted into ice. For the first time, such a comparison is based on a single set of instruments deployed at different locations. Together with thorough calibration efforts, this approach allows for unprecedented comparability in terms of data quality.

As described in Sec. 4.5, the amount of ice formed in the mixed-phase layer is measured at six height bins (180 m) below the base of the liquid-dominated cloud top and hence at the top of the virga (Bühl et al., 2016). Fig. 6.11a shows the CTT-

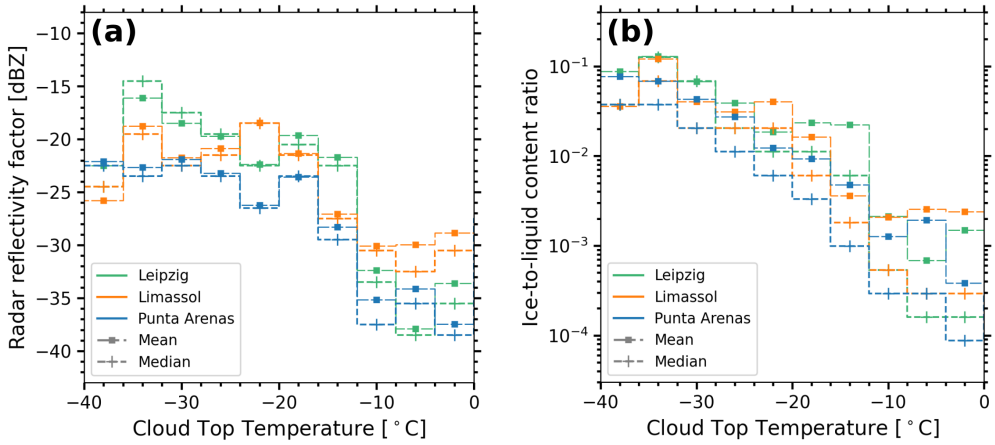

Figure 6.11: Contrasts in the ice virga in terms of (a) radar reflectivity factor observed at the top of the virga (180 m below the liquid-dominated layer base) and (b) ice-to-liquid-content-ratio binned to CTT in temperature bins of 4 K.

resolved statistics of reflectivity for the three stations based on the full cloud dataset, i.e., including the wave-influenced clouds, as these are also included in the study by Zhang et al. (2018). From −28 °C to −16 °C and again above −12 °C, Punta Arenas shows the lowest reflectivity and Limassol the highest. For most temperatures, Punta Arenas is systematically 5–8 dB below the northern-hemispheric stations, the only exception is the interval between −4 and −8 °C, where the reflectivities for Punta Arenas and Leipzig are almost equal. At temperatures below −28 °C, Limassol and Punta Arenas show equal reflectivity with values at Leipzig being slightly higher.

At all sites, the thickness of the ice-forming liquid-dominated cloud top layers agrees within 40 m above −30 °C. The ice-to-liquid content ratio (Fig. 6.11b) is smaller at Punta Arenas than at the northern-hemispheric locations, especially (factor 3) between −24 and −20 °C, but also above −10 °C. Hence, in these temperature regimes, the liquid phase is less efficiently converted into ice in clouds above Punta Arenas.

The difference in virga reflectivity is consistent with estimates from spaceborne sensors covering the full Southern Ocean (Zhang et al., 2018). As for the lower frequency of ice formation discussed above, the difference in ice mass coincides with a lack of dust INP at these temperatures. Slight differences in IWC or Z might be explained by a slower mass growth rate caused by a smaller vapor diffusion coefficient at higher ambient pressure (Hall and Pruppacher, 1976), as average temperatures of interest at Punta Arenas are reached at lower heights than at Leipzig or Limassol. When temperature and particle size are considered to be similar, the stratiform clouds subject to this study experience 10% to 20% larger growth rates at Leipzig and Limassol than at Punta Arenas. However, the difference of a factor of 3–6 larger ice mass cannot be explained solely by this effect alone.

Frequent occurrences of ice-forming clouds above −10°C were found, which were not covered by studies based on spaceborne active remote sensing. Similar to their colder counterparts, they show a lower ice amount in the virga above Punta Arenas, but with smaller difference compared to the sites in the northern hemisphere. With

an average reflectivity of −36 dBZ, they are usually well below the detection limit of the CLOUDSAT satellite in the A-Train constellation (Bühl et al., 2013a; Bühl et al., 2016). Occurrence of such clouds in other parts of the Southern Ocean cannot be ruled out. A misclassification of supercooled drizzle clouds as ice-containing is unlikely, as neither in the liquid-dominated cloud top layer nor in the virga the reflectivity exceeds −30 dBZ. From previous studies it is known that the onset of drizzle formation is usually associated with higher reflectivities, either above approximately −20 dBZ (Liu et al., 2008; Acquistapace et al., 2019) or at least above −30 dBZ (Wu et al., 2020). Nonetheless, contrasts in the amount of ice formed in mixed-phase clouds have to be investigated in more detail, especially taking into account effects of strong deposition growth for non-spherical particles.

7 Multi-peak occurrence statistics of deeper clouds

So far, statistical analysis was based on the assumption of mono-modality in the radar Doppler spectra, though the case studies illustrated that multi-peak situations occur periodically. Due to the variety of microphysical processes occurring in mixed-phase clouds, multiple particle populations regularly coexist in the same volume. Sometimes, two or more particle populations appear as distinct peaks in the cloud radar Doppler spectrum. The following section illustrates how the peakTree technique can be used to analyze large datasets of (potentially) multi-peaked Doppler spectra.

Starting from the layered clouds selected by the automated cloud identification scheme (Sec. 4.5), the criterion for the thickness of the liquid-dominated layer is relaxed. Clouds such as shown in Fig. 4.17 or 6.2 are now included into the selection. When the lidar beam is fully attenuated in the lowest liquid layer, no certain classification of the cloud particle phase can be obtained at larger heights (see Fig. 4.17). Without additional information, the Cloudnet target classification will identify ice particles solely based on the cloud radar signal. Thus, the distance between lidar-identified liquid base and radar-identified cloud top only serves as a first proxy for the thickness of the mixed-phase layer. Fig. 7.1 shows the fraction of radar pixels within a cloud case that have more than one peak for Leipzig, Limassol, and Punta Arenas. With increasing cloud thickness, the fraction of multi-peak pixels increases at all three sites. For clouds with mixed-phase layer thickness larger than 500 m, more than 5% of the pixels in a cloud show multi-peak Doppler spectra. This estimate provides a lower bound of the presence of multiple particle populations, as different hydrometeor populations do not always appear as distinct peaks in the Doppler spectrum. Multiple particle populations are a strong indicator for processes such as riming or additional ice particle production. More detailed investigation of these cases is needed in subsequent studies.

In a next step, the constraint to layered clouds is dropped completely and all cloud radar observations are considered. Also in the full dataset at all temperatures, mono-modal Doppler spectra are the most frequent ones (Fig. 7.2). They are followed by bimodal ones (3 nodes, see Eq. 4.14), which are found at all temperatures above −30 °C. Higher numbers of subpeaks are rarely found under slightly supercooled conditions (−5 to 0 °C). Above 0 °C, mono-modal spectra only account for approximately 50% of the observations, and around 25% of the Doppler spectra contain 5 nodes or more. As it becomes evident from the number of nodes sampled by the Cloudnet target classification product, the multi-peak spectra above 0 °C are predominantly associated with liquid precipitation (Fig. 7.3). Consequently, the 'drizzle/rain' class shows the highest

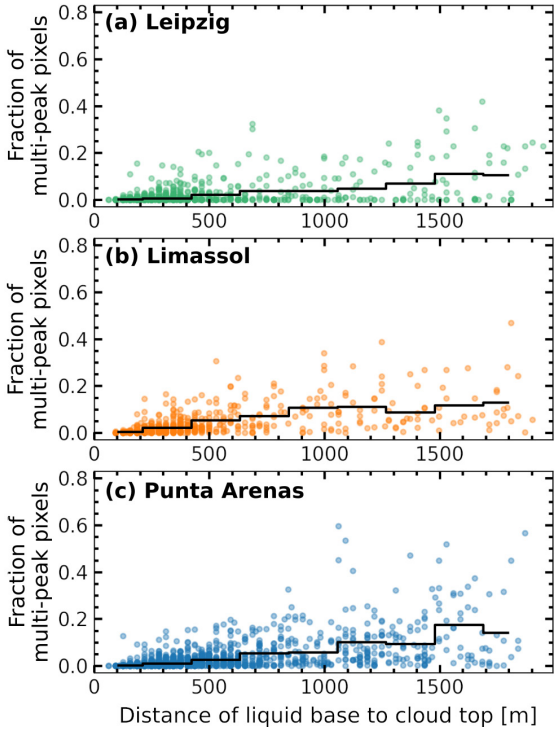

Figure 7.1: Fraction of multi-peak pixels within a stratiform cloud vs. distance of lowest liquid layer to cloud top for (a) Leipzig, (b) Limassol, and (c) Punta Arenas. The mean of 190 m bins is also shown.

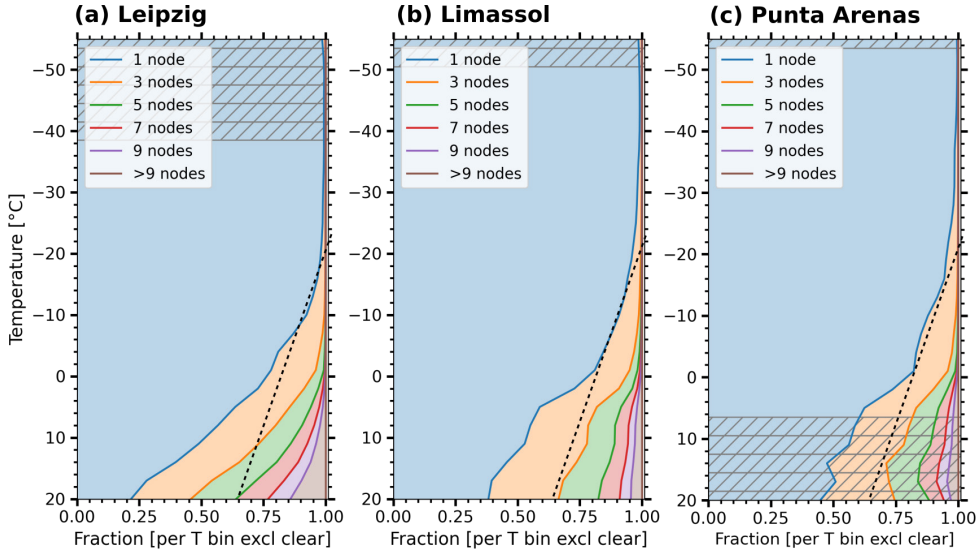

Figure 7.2: Fraction of pixels having a specific number of nodes binned in temperature steps of 3 K for (a) Leipzig, (b) Limassol, and (c) Punta Arenas. Hatching indicates bins with less than 2% of the cloudy pixels.

fraction of multi-peaked Doppler spectra – almost 55%. The categories 'drizzle/rain + droplets' and 'melting ice + droplets' follow with about 30%. For 'ice', 'cloud droplets', and the combination of both, multiple peaks occur in 6% to 17% of the Doppler spectra. However, in absolute terms, the 'ice' class features the highest number of multi-peak situations, as this is also by far the most frequent class. Multiple peaks classified as aerosol are likely caused by different species of atmospheric plankton.

The tree structure also allows the test of assumptions that are frequently imposed by established multi-peak algorithms. The microARSCL analysis (Kollias et al., 2007; Luke et al., 2008) assumes, e.g., that the subpeak with the largest reflectivity also is the fastest falling one (Oue et al., 2018). This peak is then dubbed primary peak. In terms of the tree structure, this higher-reflectivity-faster-falling assumption translates into node 1 having a larger reflectivity than node 2, a condition that can easily be tested on large datasets using peakTree. As evident from Fig. 7.4, the microARSCL assumption only holds for 35%–65%, 40%, and 35%–75% of the observations (depending on temperature) at Leipzig, Limassol, and Punta Arenas, respectively.

The presented statistics illustrate the need for further investigation of precipitating cloud systems for coexistence of multiple particle species at the scales of the radar observation volume. So far, multi-peak information is not included into synergistic retrievals and classification schemes. All established approaches assume only monomodal particle size distributions and only a single particle habit (e.g., Clothiaux et al., 2000; Wang and Sassen, 2002; Wang et al., 2004; Hogan et al., 2006; Illingworth et al., 2007; Zhang et al., 2014; Cazenave et al., 2019). If multiple hydrometeor species are present, they have to be separated and classified individually to be able to apply the correct size-fall-velocity and size-mass relationships. The rigid, though flexible tree structure might help to address the described issues.

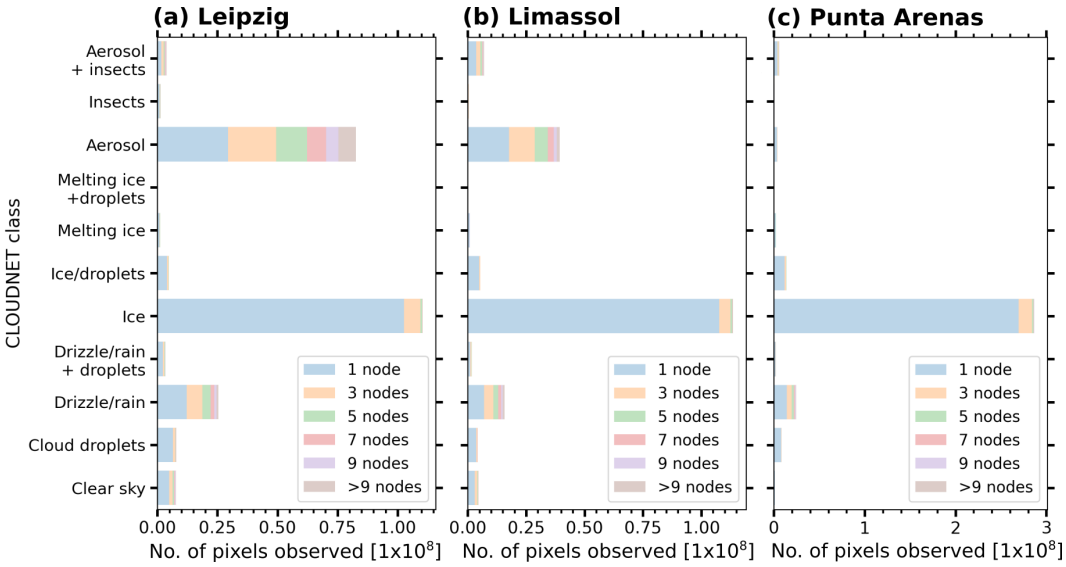

Figure 7.3: Number of pixels having a specific number of nodes per Cloudnet classification for (a) Leipzig, (b) Limassol, and (c) Punta Arenas. Hatching indicates bins with less than 2% of the cloudy pixels.

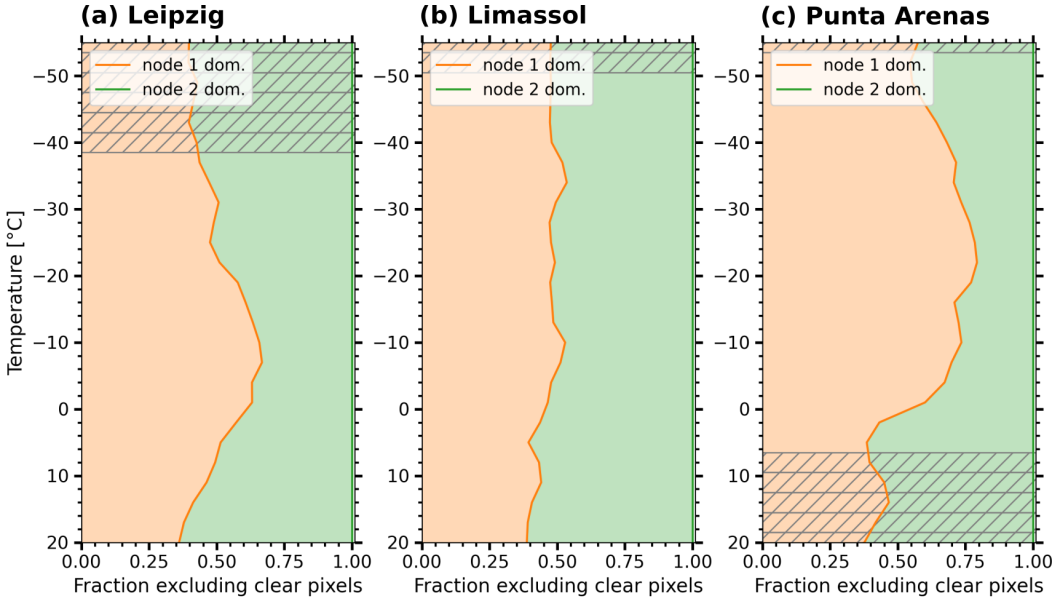

Figure 7.4: Fraction of pixels having more than 3 nodes, where node 1 or node 2 is dominant. Hatching indicates bins with less than 2% of the cloudy pixels.

8 Summary, Conclusions, and Outlook

8.1 Summary and conclusions

This study aimed to contrast hemispheric differences of heterogeneous ice formation in shallow supercooled stratiform clouds. For doing so, three long-term datasets of the ground-based remote-sensing supersite LACROS were analyzed. While the datasets at Leipzig and Limassol were readily available, the measurements at Punta Arenas were conducted in the framework of this study. Additional to planning, preparation, and continuous remote monitoring of the instrumentation, more than six months were spent by the author supervising the measurements on-site. Compared with earlier datasets at the respective locations, the LACROS-based dataset expanded the observation capabilities significantly. Most important ones are the improved sensitivity to small ice particles by adding a cloud radar and the ability to measure vertical velocity with cloud radar and Doppler lidar for the characterization of vertical motions in the observed clouds. The datasets at Limassol and Punta Arenas resemble the first multi-year ground-based remote-sensing datasets in the Eastern Mediterranean and in the western part of the Southern Ocean, respectively.

With respect to data analysis, existing methods and synergistic retrievals were expanded and new methodologies were developed. In particular, three topics were addressed: automated airmass source characterization, multi-peak analysis of radar Doppler spectra, and gravity-wave identification using Doppler lidar observations.

The automated airmass-source-analysis technique provided novel insights into the profiles of airmass history. Continuous estimates of height-resolved residence time per surface class, named source region, and latitude were presented. Based on these datasets a sampling bias analysis could be performed. It was shown that Punta Arenas is predominantly influenced by marine sources for airmasses with temperatures below 0 °C. At all three locations, the transition between local influences and long-range transport occurs between −12 and −17 °C. Also, no significant sampling biases were found for the lidar-based average aerosol optical properties. To characterize the aerosol conditions, long-term statistics of aerosol optical properties based on the PollyNET products at all sites were assembled. Adding the synergistic Cloudnet classification product to the lidar profiles ensures confident filtering for optically thin clouds. Both the profiles of optical properties and the profiles of airmass source were analyzed with temperature as a vertical coordinate, hence resolving the thermodynamical constraints to aerosol-cloud interaction in more detail. Combining the airmass source with the optical properties allows a rough estimate of INP load throughout the troposphere based on widely used parametrizations. Meanwhile, the airmass source characterization was

successfully used in further studies, e.g., Haarig et al. (2017), Foth et al. (2019), Floutsi et al. (2021), Baars et al. (2021), and Griesche et al. (2021).

With the multi-peak Doppler spectra analysis technique peakTree, it could be confirmed that stratiform clouds with thin liquid-dominated layers do not show hints of processes other than primary ice formation. This technique will, in future, provide novel insights also into deeper clouds and help to overcome limitations of standard retrievals based on a single, mono-modal particle species. Apart form the analysis shown here, case studies with multiple particle populations in Arctic mixed-phase clouds (Radenz et al., 2019a) and generating cells in complex terrain (Ramelli et al., 2021) were successfully analyzed with this technique. For the three datasets used in this study, it was found that the frequency of multi-modal Doppler spectra increases with thickness of the liquid layer at cloud top. Extending the analysis to all clouds, it was found that multi-modal situations only occur above $-20\,^{\circ}\mathrm{C}$ and the frequency is increasing for higher temperatures, with around 40% of the Doppler spectra having multiple peaks at $0\,^{\circ}\mathrm{C}$. From the structural analysis it became clear that the higher-reflectivity-faster-falling assumption only holds for 35% to 65% of the observed multi-peak Doppler spectra.

Doppler lidar vertical-velocity observations allow the characterization of vertical motion in liquid layers consisting of small droplets. A scheme for the identification of gravity waves in layered clouds was developed. The autocorrelation coefficient proved to be a suitable measure for the structure of vertical motion in an observed cloud and was successfully used to distinguish wave clouds from fully turbulent clouds in the large dataset.

All these developments were tied together with LARDA to obtain the dataset of stratiform cloud cases on which the statistical analysis is based. Major improvements, including the implementation of a distributed architecture, a browser-based interactive plotting tool, and open-sourcing the software were part of this work and prerequisite for the analysis of the multi-year record. This software development represents a crucial step forward in the integration of such a large and heterogeneous dataset. Meanwhile, the distributed LARDA version is successfully applied to operational settings, including field deployments.

Regarding the research questions posed in the introduction, the results on properties of supercooled stratiform clouds are summarized in the following. The questions are ordered by the respective sections in Chapter 6:

Did prior lidar-only studies underestimate the frequency ice formation at high temperatures? (RQ IV) The combined radar-lidar observations showed frequent ice production in clouds with CTT above $-12\,^{\circ}\mathrm{C}$. These only slightly supercooled layers produce only low IWC in the virga. Due to a lower sensitivity of lidar-only approaches much of this ice production is missed. A minimum ice extinction threshold has to be applied to the combined dataset. After filtering for these clouds with low IWC, the results of prior lidar-only studies could be reproduced.

Do enhanced INP concentrations in surface-coupled cloud layers influence the frequency of ice formation? (RQ III) Based on the average profiles of airmass source and aerosol optical properties, a distinct change was found for heights, where the temperature drops below −12 to −16 °C. Higher temperatures (lower heights) are usually associated with local sources, whereas lower temperatures (larger heights) are dominated by long-range-transported airmasses. This change is remarkably pronounced at Punta Arenas, where typical boundary-layer tops are found at temperatures of −10 to −17 °C. When comparing aerosol optical properties, average extinction coefficients at Punta Arenas and Limassol are within a factor of two between 0 and −10 °C. For lower temperatures, aerosol extinction coefficients at Limassol and Leipzig are a factor of 2–6 larger than at Punta Arenas. A further feature at Punta Arenas is the very low average particle linear depolarization ratio between −10 and −25 °C, hinting to the complete absence of mineral dust in this temperature regime. Consequently, indications were found that coupling to the surface increases ice formation at slightly supercooling temperatures at all three sites. The strongest enhancement from free-tropospheric to surface-coupled frequencies of ice formation was also found at Punta Arenas. This enhancement agrees with the found contrasts in the INP profiles at the three sites and further indicates that the free-tropospheric INP reservoir over the Southern Ocean is limited.

Is the reported high frequency of supercooled liquid water in the southern hemisphere caused by the low abundance of INP alone? (RQ II) One outstanding feature of the stratiform clouds at Punta Arenas is the frequent occurrence of liquid-only cloud layers at temperatures below −20 °C. Using the newly developed Doppler lidar vertical-velocity autocorrelation approach, these layers were identified to be embedded in orographic gravity waves. In such orographic gravity waves, the liquid and ice phases are separated horizontally, hence ice formation cannot be correctly diagnosed with the automated approach, in which ice is assumed to sediment from the liquid-dominated top. Excluding these clouds from the occurrence statistics raises the fraction of ice-containing clouds at Punta Arenas to values above 0.85 – almost similar to the frequencies at Leipzig and Limassol. For clouds with ICNC below $\sim 50\,\mathrm{L}^{-1}$, weak persistent updrafts alone are able to sustain liquid water, as shown in the analytical treatment (Chapter 2). Under these conditions, the abundance of INP is only of secondary importance. Hence, observation of in-cloud vertical air motion is necessary when investigating ice formation in stratiform clouds.

Are there aerosol-related contrasts in ice formation in stratiform mixed-phase clouds in the mid-latitudes of the southern hemisphere and the polluted northern hemisphere? (RQ I) The frequency of ice formation in fully-turbulent and free-tropospheric stratiform clouds can only be compared between the sites after accounting for the effects of surface coupling and gravity waves. At temperatures between −12 and −25 °C, the frequency of ice-containing clouds is lower by 0.05 to 0.10 at Punta Arenas compared with the northern-hemispheric sites. In this temperature interval,

also the average amount of ice formed and the ice-to-liquid content ratio is lowest at Punta Arenas. For slightly supercooled conditions, the difference in the frequency of ice formation increases to 0.3. This remaining difference can be attributed to the lower abundance of INP in the free troposphere over the Southern Ocean.

8.2 Outlook

The datasets presented in this study allow an unprecedented insight into hemispheric contrasts of ice formation in shallow supercooled clouds. However, the presented study is only the starting point for further in-depth analysis. The two most interesting new findings from Punta Arenas, the high frequency of wave clouds and the strong contrasts in aerosol load between the boundary layer and the free troposphere, alone pose further research objectives. A few topics will be briefly touched in this section.

Based on the available datasets, more detailed investigations of the microphysical properties have to be conducted, especially the number concentrations of ice and liquid hydrometeors have to be better constrained. A promising approach might be the combination of the dual-field-of-view lidar technique (Jimenez et al., 2020a; Jimenez et al., 2020b) and retrievals based on quantitative radar-lidar synergy (e.g., Bühl et al., 2019b). Precise estimates of terminal fall velocity of ice crystals will require further efforts, as the orographic gravity waves bias these observations. Also, the autocorrelation technique might prove to be useful in the analysis of gravity waves from single-site observations, a challenge that was faced by Silber et al. (2020) as well. In case of the presence of suitable tracers of air motion, the autocorrelation technique can also be applied to vertical-velocity observations from other instruments.

In terms of methodologies, the classification of slightly supercooled clouds and the criterion for boundary-layer coupling have to be improved. Currently, the Cloudnet classification scheme cannot discriminate between ice with low IWC and supercooled liquid water. Distinguishing ice and liquid water independently from the temperature will likely require scanning polarimetric radar observations, which add further complexity to synergistic retrievals. However, a probabilistic classification will be needed as both ice and supercooled drizzle might coexist. For the surface coupling, a continuous and reliable estimate of boundary-layer height is needed, even under cloudy conditions. As lidar observations of aerosol backscatter and air motion are not available under those circumstances, no continuous remote-sensing-based estimate of boundary-layer height is available yet.

Clouds with deeper mixed-phase layers are also a promising topic of further research. In those clouds, multiple particle populations frequently coexist, e.g., as embedded liquid layers or different ice crystal habits. The information content in radar Doppler spectra provides promising opportunities for more detailed investigations. With the peakTree analysis technique, the integration of this multi-peak information into existing retrievals might be feasible.

The comparison of the the aerosol in-situ observations on Cerro Mirador and lidar-retrieved aerosol optical properties is already under investigation. A combination of

both long-term datasets provides more comprehensive information about the cloud-relevant aerosol properties at Punta Arenas. First analysis (not shown) already suggests the presence of multiple species of INP in the boundary layer over Punta Arenas. These INP are ice active at temperatures slightly below 0 °C and are present independent of season.

Despite all novel insights, gaps requiring additional observations remain. The vertical velocity in the complex flow around Punta Arenas is still not well characterized. One potential approach is the inclusion of a high-power, narrow-beamwidth radar wind profiler into future ground-based remote-sensing campaigns. With frequencies in the ultra-high-frequency band, these instruments are also sensitive to clear-air scattering. The problem of simultaneous returns from hydrometeors can be approached by spectral techniques, such as proposed in earlier work (Radenz et al., 2018). The question of dynamical forcing on clouds over the open Southern Ocean is connected to the issue of better characterization of vertical velocity. Sustained updrafts triggered by waves might contribute to the abundance of liquid water, even far from any orographic forcing. Little is also known about the contribution of terrestrial and marine sources of aerosol to the free troposphere over the Southern Ocean. Significant progress on the questions of vertical motion and free-tropospheric aerosol without further comprehensive observations, especially on shipborne platforms, seems unlikely. If such an endeavor is attempted, the combination of profiling remote-sensing observations with in-situ characterization of aerosol, clouds, and dynamics in the boundary layer and the free troposphere is pivotal. Ideally, such a campaign includes long-term observations upwind and downwind of a major land mass. In that case, both the decreasing impact of continental aerosols and orographically driven gravity waves could be investigated simultaneously.

A Further equations

The coefficients from the Korolev formalism (Korolev and Mazin, 2003; Korolev, 2008; Pinsky et al., 2014) are:

$$a_0 = \frac{g}{R_\mathrm{a} T}\left(\frac{L_\mathrm{w} R_\mathrm{a}}{c_\mathrm{p} R_\mathrm{v} T} - 1\right), \tag{A.1}$$

$$a_1 = \frac{1}{q_\mathrm{v}} + \frac{L_\mathrm{w}^2}{c_\mathrm{p} R_\mathrm{v} T^2}, \tag{A.2}$$

$$a_2 = \frac{1}{q_\mathrm{v}} + \frac{L_\mathrm{w} L_\mathrm{i}}{c_\mathrm{p} R_\mathrm{v} T^2}, \tag{A.3}$$

$$a_3 = \frac{1}{q_\mathrm{v}} + \frac{L_\mathrm{i} L_\mathrm{i}}{c_\mathrm{p} R_\mathrm{v} T^2}, \tag{A.4}$$

$$A_\mathrm{i} = \left(\frac{\rho_\mathrm{i} L_\mathrm{i}^2}{k R_\mathrm{v} T^2} + \frac{\rho_\mathrm{i} R_\mathrm{v} T}{e_{\mathrm{i,\,s}} D}\right)^{-1}, \tag{A.5}$$

$$A_\mathrm{l} = \left(\frac{\rho_\mathrm{l} L_\mathrm{w}^2}{k R_\mathrm{v} T^2} + \frac{\rho_\mathrm{l} R_\mathrm{v} T}{e_{\mathrm{l,\,s}} D}\right)^{-1}, \tag{A.6}$$

$$B_\mathrm{l} = \frac{4\pi\rho_\mathrm{l} A_\mathrm{l}}{\rho_\mathrm{a}}, \tag{A.7}$$

$$B_\mathrm{i} = \frac{4\pi\rho_\mathrm{i}\phi A_\mathrm{i}}{\rho_\mathrm{a}}, \tag{A.8}$$

$$B_{\mathrm{i},0} = \frac{4\pi\rho_\mathrm{i} A_\mathrm{i}}{\rho_\mathrm{a}}, \tag{A.9}$$

$$B_\mathrm{i}^* = \frac{4\pi\rho_\mathrm{i}(\phi - 1) A_\mathrm{i}}{\rho_\mathrm{a}}, \tag{A.10}$$

$$b_\mathrm{l} = a_1 B_\mathrm{l}, \tag{A.11}$$

$$b_\mathrm{i} = a_2 B_\mathrm{i}, \tag{A.12}$$

$$b_{\mathrm{i},0} = a_2 B_{\mathrm{i},0}, \tag{A.13}$$

$$b_\mathrm{i}^* = a_2 B_\mathrm{i}^*, \tag{A.14}$$

$$\tag{A.15}$$

The harmonizing factors are:

$$\Upsilon_\mathrm{l} = \left(\frac{3\rho_\mathrm{a}}{4\pi\rho_\mathrm{l}}\right)^{1/3}, \tag{A.16}$$

$$\Upsilon_\mathrm{i} = \left(\frac{3\rho_\mathrm{a}}{4\pi\rho_\mathrm{i}}\right)^{1/3} \phi^{-1}. \tag{A.17}$$

The capacitance C_i for oblate ($r_\mathrm{c} < r_\mathrm{a}$) and prolate ($r_\mathrm{c} > r_\mathrm{a}$) particles, depending on the spheroids major and minor axis r_a and r_c:

$$C_\mathrm{i} = \frac{r_\mathrm{a}\sqrt{1-(r_\mathrm{c}/r_\mathrm{a})^2}}{\arcsin\sqrt{1-(r_\mathrm{c}/r_\mathrm{a})^2}} \quad \text{for } r_\mathrm{c} < r_\mathrm{a}, \tag{A.18}$$

$$C_\mathrm{i} = \frac{r_\mathrm{c}\sqrt{1-(r_\mathrm{c}/r_\mathrm{a})^{-2}}}{\ln\left[\left(1+\sqrt{1-(r_\mathrm{c}/r_\mathrm{a})^{-2}}\right) r_\mathrm{c}/r_\mathrm{a}\right]} \quad \text{for } r_\mathrm{c} > r_\mathrm{a}. \tag{A.19}$$

Publication record

For the publications included in this thesis, the contributions of all co-authors are described, strongly oriented on the 'Author contributions' section of the respective publications. For peer-reviewed articles not included into the thesis, only my contribution is given.

Peer-reviewed articles included in this thesis

- Radenz, M., J. Bühl, P. Seifert, H. Griesche, and R. Engelmann. 2019a. "peakTree: a framework for structure-preserving radar Doppler spectra analysis." *Atmospheric Measurement Techniques* 12 (9): 4813–4828. https://doi.org/10.5194/amt-12-4813-2019.
  Own contribution (OC): For this publication, I developed the multi-peak Doppler spectra analysis algorithm and drafted the paper. Johannes Bühl supported the implementation. Johannes Bühl and Patric Seifert supervised the work together. Patric Seifert and Hannes Griesche preprocessed the Doppler spectra of MIRA-35. Hannes Griesche, Ronny Engelmann, and me operated MIRA-35 onboard Polarstern. All authors jointly contributed to the paper and the scientific discussion.

- Radenz, M., P. Seifert, H. Baars, A. A. Floutsi, Z. Yin, and J. Bühl. 2021a. "Automated time–height-resolved air mass source attribution for profiling remote sensing applications." *Atmospheric Chemistry and Physics* 21 (4): 3015–3033. https://doi.org/10.5194/acp-21-3015-2021.
  OC: For this publication, I developed the air mass source identification algorithm and drafted the paper. Patric Seifert and Johannes Bühl supported the implementation and supervised the work. Holger Baars, Athena Augusta Floutsi and Zhenping Yin analyzed the lidar profiles (data for Fig. 5, 8, 9, and 12). Also the data for Fig. 14a and 15a was provided by Holger Baars. All authors jointly contributed to the paper and the scientific discussion.

Article under review included in this thesis

- Radenz, M., J. Bühl, P. Seifert, H. Baars, R. Engelmann, B. Barja González, R.-E. Mamouri, F. Zamorano, and A. Ansmann. 2021b. "Hemispheric Contrasts in Ice Formation in Stratiform Mixed-Phase Clouds: Disentangling the Role of Aerosol and Dynamics with Ground-Based Remote Sensing." *Atmospheric Chemistry and Physics Discussions* 2021. https://doi.org/10.5194/acp-2021-360.

OC: For this publication, I analyzed the data and drafted the manuscript. The campaigns were conducted by myself, Patric Seifert, Johannes Bühl, Holger Baars, Ronny Engelmann, Boris Barja González, Rodanthi-Elisabeth Mamouri, and Félix Zamorano. Patric Seifert, myself, and Johannes Bühl generated the Cloudnet dataset. Holger Baars processed the Polly^{XT} lidar data. Patric Seifert, Johannes Bühl, and Albert Ansmann supervised the work and revised the manuscript. All authors jointly contributed to the paper and the scientific discussion.

Further peer-reviewed articles

- Bühl, J., R. Leinweber, U. Görsdorf, M. Radenz, A. Ansmann, and V. Lehmann. 2015. "Combined Vertical-Velocity Observations with Doppler Lidar, Cloud Radar and Wind Profiler." *Atmospheric Measurement Techniques* 8 (8): 3527–3536. https://doi.org/10.5194/amt-8-3527-2015.
  OC: For this publication, I contributed an early version of the combined radar wind profiler/cloud radar processing (esp. Fig. 10) and participated in the discussion.

- Haarig, M., A. Ansmann, J. Gasteiger, K. Kandler, D. Althausen, H. Baars, M. Radenz, and D. A. Farrell. 2017. "Dry versus wet marine particle optical properties: RH dependence of depolarization ratio, backscatter, and extinction from multiwavelength lidar measurements during SALTRACE." *Atmospheric Chemistry and Physics* 17 (23): 14199–14217. https://doi.org/10.5194/acp-17-14199-2017.
  OC: For this publication, I contributed and early version of the air mass source identification, shown in Fig. 7 and contributed to Sec. 4.1.

- Radenz, M., J. Bühl, V. Lehmann, U. Görsdorf, and R. Leinweber. 2018. "Combining cloud radar and radar wind profiler for a value added estimate of vertical air motion and particle terminal velocity within clouds." *Atmospheric Measurement Techniques* 11 (10): 5925–5940. https://doi.org/10.5194/amt-11-5925-2018.
  OC: For this publication, I developed the combined radar wind profiler/cloud radar data processing for an in-cloud estimate of vertical air velocity and drafted the paper.

- Bohlmann, S., H. Baars, M. Radenz, R. Engelmann, and A. Macke. 2018. "Ship-Borne Aerosol Profiling with Lidar over the Atlantic Ocean: From Pure Marine Conditions to Complex Dust–Smoke Mixtures." *Atmospheric Chemistry and Physics* 18 (13): 9661–9679. https://doi.org/10.5194/acp-18-9661-2018.
  OC: For this publication, I operated the Polly^{XT} lidar on Polarstern (PS 98) with Stephanie Bohlmann and contributed to the interpretation of results.

- Yin, Z., A. Ansmann, H. Baars, P. Seifert, R. Engelmann, M. Radenz, C. Jimenez, A. Herzog, K. Ohneiser, K. Hanbuch, L. Blarel, P. Goloub, G. Dubois, S. Victori, and F. Maupin. 2019. "Aerosol Measurements with a Shipborne Sun–Sky–Lunar Photometer and Collocated Multiwavelength Raman Polarization Lidar over

the Atlantic Ocean." *Atmospheric Measurement Techniques* 12 (10): 5685–5698. https://doi.org/10.5194/amt-12-5685-2019.
OC: For this publication, I operated the OCEANET instrument suite on Polarstern (PS 113) together with Cristofer Jimenez and Zhenping Yin. I contributed to the discussion of the results.

- Foth, A., T. Kanitz, R. Engelmann, H. Baars, M. Radenz, P. Seifert, B. Barja, M. Fromm, H. Kalesse, and A. Ansmann. 2019. "Vertical aerosol distribution in the southern hemispheric midlatitudes as observed with lidar in Punta Arenas, Chile (53.2°S and 70.9°W), during ALPACA." *Atmospheric Chemistry and Physics* 19 (9): 6217–6233. https://doi.org/10.5194/acp-19-6217-2019.
OC: For this publication, I provided the air mass source analysis (Fig. 11d) and prepared Fig. 1. I also contributed to the discussion.

- Bühl, J., P. Seifert, M. Radenz, H. Baars, and A. Ansmann. 2019b. "Ice Crystal Number Concentration from Lidar, Cloud Radar and Radar Wind Profiler Measurements." *Atmospheric Measurement Techniques* 12 (12): 6601–6617. https://doi.org/10.5194/amt-12-6601-2019.
OC: For this publication, I contributed the methods for estimating the ice crystal terminal fall velocity and participated in the interpretation of the results.

- Jimenez, C., A. Ansmann, R. Engelmann, D. Donovan, A. Malinka, P. Seifert, R. Wiesen, M. Radenz, Z. Yin, J. Bühl, J. Schmidt, B. Barja, and U. Wandinger. 2020b. "The Dual-Field-of-View Polarization Lidar Technique: A New Concept in Monitoring Aerosol Effects in Liquid-Water Clouds – Case Studies." *Atmospheric Chemistry and Physics* 20 (23): 15265–15284. https://doi.org/10.5194/acp-20-15265-2020.
OC: For this publication, I significantly contributed to the LACROS observations at Punta Arenas in the frame of DACAPO-PESO.

- Ohneiser, K., A. Ansmann, H. Baars, P. Seifert, B. Barja, C. Jimenez, M. Radenz, A. Teisseire, A. Floutsi, M. Haarig, A. Foth, A. Chudnovsky, R. Engelmann, F. Zamorano, J. Bühl, and U. Wandinger. 2020. "Smoke of extreme Australian bushfires observed in the stratosphere over Punta Arenas, Chile, in January 2020: optical thickness, lidar ratios, and depolarization ratios at 355 and 532 nm." *Atmospheric Chemistry and Physics* 20 (13): 8003–8015. https://doi.org/10.5194/acp-20-8003-2020.
OC: For this publication, I significantly contributed to the LACROS observations at Punta Arenas in the frame of DACAPO-PESO.

- Villanueva, D., B. Heinold, P. Seifert, H. Deneke, M. Radenz, and I. Tegen. 2020. "The day-to-day co-variability between mineral dust and cloud glaciation: a proxy for heterogeneous freezing." *Atmospheric Chemistry and Physics* 20 (4): 2177–2199. https://doi.org/10.5194/acp-20-2177-2020.
OC: For this publication, I contributed to interpretation of the observations and discussion of the results.

- Griesche, H. J., P. Seifert, A. Ansmann, H. Baars, C. Barrientos Velasco, J. Bühl, R. Engelmann, M. Radenz, Y. Zhenping, and A. Macke. 2020. "Application of the Shipborne Remote Sensing Supersite OCEANET for Profiling of Arctic Aerosols and Clouds during Polarstern Cruise PS106." *Atmospheric Measurement Techniques* 13 (10): 5335–5358. https://doi.org/10.5194/amt-13-5335-2020.
  OC: For this publication, I contributed to the implementation of the cloud radar observations, operated OCEANET for the second month of the expedition and contributed to the data analysis.

- Floutsi, A. A., H. Baars, M. Radenz, M. Haarig, Z. Yin, P. Seifert, C. Jimenez, A. Ansmann, R. Engelmann, B. Barja, F. Zamorano, and U. Wandinger. 2021. "Advection of Biomass Burning Aerosols towards the Southern Hemispheric Mid-Latitude Station of Punta Arenas as Observed with Multiwavelength Polarization Raman Lidar." *Remote Sensing* 13 (1): 138. https://doi.org/10.3390/rs13010138.
  OC: For this publication, I significantly contributed to the LACROS observations at Punta Arenas in the frame of DACAPO-PESO. Furthermore I provided the air mass source data (Figs. 3, 4, 7, 8) and the overview map (Fig. 1). I contributed to the interpretation of the results.

- Baars, H., M. Radenz, A. A. Floutsi, R. Engelmann, D. Althausen, B. Heese, A. Ansmann, T. Flament, A. Dabas, D. Trapon, O. Reitebuch, S. Bley, and U. Wandinger. 2021. "Californian Wildfire Smoke Over Europe: A First Example of the Aerosol Observing Capabilities of Aeolus Compared to Ground-Based Lidar." *Geophysical Research Letters* 48 (8). https://doi.org/10.1029/2020GL092194.
  OC: For this publication, I contributed the air mass source interpretation, characterizing the long-range transport across the Atlantic Ocean (Figs. 2, 3). I also participated in discussing the results and drafting the manuscript.

- Ramelli, F., J. Henneberger, R. O. David, J. Bühl, M. Radenz, P. Seifert, J. Wieder, A. Lauber, J. T. Pasquier, R. Engelmann, C. Mignani, M. Hervo, and U. Lohmann. 2021. "Microphysical Investigation of the Seeder and Feeder Region of an Alpine Mixed-Phase Cloud." *Atmospheric Chemistry and Physics* 21 (9): 6681–6706. https://doi.org/10.5194/acp-21-6681-2021.
  OC: For this publication, I provided the peakTree analysis of the cloud radar Doppler spectra (Fig. 8c) and contributed to the interpretation.

- Griesche, H. J., K. Ohneiser, P. Seifert, M. Radenz, R. Engelmann, and A. Ansmann. 2021. "Contrasting Ice Formation in Arctic Clouds: Surface-Coupled vs. Surface-Decoupled Clouds." *Atmospheric Chemistry and Physics* 21 (13): 10357–10374. https://doi.org/10.5194/acp-21-10357-2021.
  OC: For this publication, I contributed the air mass source interpretation (Fig. 8).

- Engelmann, R., A. Ansmann, K. Ohneiser, H. Griesche, M. Radenz, J. Hofer, D. Althausen, S. Dahlke, M. Maturilli, I. Veselovskii, C. Jimenez, R. Wiesen, H. Baars, J. Bühl, H. Gebauer, M. Haarig, P. Seifert, U. Wandinger, and A. Macke. 2021. "Wildfire Smoke, Arctic Haze, and Aerosol Effects on Mixed-Phase and

Cirrus Clouds over the North Pole Region during MOSAiC: An Introduction." *Atmospheric Chemistry and Physics* 21 (17): 13397–13423. https://doi.org/10.5194/acp-21-13397-2021.
OC: For this publication, I operated the OCEANET instrument suite on Polarstern during MOSAiC leg 3.

Software publications

- Bühl, J., M. Radenz, W. Schimmel, T. Vogl, J. Röttenbacher, and M. Lochmann. 2021. "pyLARDA v3.2." https://doi.org/10.5281/zenodo.4721311.
- Radenz, M. 2021. "martin-rdz/trace_airmass_source: trace_airmass_source jan2021." https://doi.org/10.5281/zenodo.4438051.
- Radenz, M., and J. Bühl. 2021. "larda cloud sniffer." https://doi.org/10.5281/zenodo.4723824.
- Radenz, M., J. Bühl, and P. Seifert. 2019b. "peakTree version of Aug2019." https://doi.org/10.5281/zenodo.3369295.
- Radenz, M., and J. Bühl. 2018. "Software package for added value products from combined measurements of Radar Wind Profiler and Cloud Radar ("Spectra Mole") - Release from 2018-10-05." https://doi.org/10.5281/zenodo.1419486.
- The source code for reproducing the figures shown in chapter 2 is openly available at https://github.com/martin-rdz/mixed-phase_cloud_analytical.

List of Abbreviations and Acronyms

A-LIFE	Absorbing aerosol layers in a changing climate: aging, lifetime and dynamics
ACCEPT	Analysis of the Composition of Clouds with Extended Polarization Techniques
AERONET	Aerosol Robotic Network
AOT	aerosol optical thickness
ARL	Air Resources Laboratory
CCN	cloud condensation nuclei
CNT	classical nucleation theory
CTT	cloud top temperature
CyCARE	Cyprus Clouds, Aerosol and Rain Experiment
DACAPO-PESO	Dynamics Aerosol Clouds And Precipitation Observation in the Pristine Environment of the Southern Ocean
ECMWF	European Centre for Medium-Range Weather Forecast
FFT	Fast Fourier Transform
FLEXPART	FLEXible PARTicle dispersion model
FLEXTRA	FLEXible TRAjectories
GDAS1	Global Data Assimilation System at 1°
GFS	Global Forecast System
HYSPLIT	Hybrid Single-Particle Lagrangian IntegratedTrajectory model
ICNC	ice crystal number concentration
ICPR	integrated cross-polarization ratio
IFS	Integrated Forecasting System
IGRA	Integrated Global Radiosonde Archive
ILCR	ice-to-liquid content ratio
INP	ice-nucleating particle

IWC	ice-water conent
IWV	integrated water vapor
LACROS	Leipzig Aerosol and Cloud Remote Observations System
LAGRANTO	Lagrangian analysis tool
LARDA	LACROS Research Data Application
LDR	linear depolarization ratio
LPDM	Lagrangian particle dispersion model
LWC	liquid-water content
LWP	liquid-water path
microARSCL	Microscale Active Remote Sensing of Clouds
MODIS	Moderate-resolution Imaging Spectroradiometer
MWR	microwave radiometer
NFFT	number of points in the Fast Fourier Transform
NWP	Numerical weather prediction
PPI	plan-position-indicator
PRF	pulse repetition frequency
RHI	range-height-indicator
RQ	research question
TROPOS	Leibniz Institute for Tropospheric Research

List of Symbols

A_i	Deposition growth coefficient for ice	14, 95
A_l	Deposition growth coefficient for liquid water	95
α_thres	Lidar ice-water detection threshold	76
β_p	Particle backscatter coefficient	29, 30, 62, 64, 76
$\bar{r}_\mathrm{i}$	Ice crystal average radius	10–12
$\bar{r}_\mathrm{l}$	Liquid droplet average radius	10, 11
C_i	Ice crystal capacitance	14, 96
Θ	Contact angle	8
$e_{\mathrm{i,s}}$	Saturation water-vapor pressure over ice	9–11, 95
$e_{\mathrm{l,s}}$	Saturation water-vapor pressure over liquid water	9–12, 95
$\eta(\vec{r})$	Volume reflectivity	30
$\eta'(\vec{r}, v)$	Volume spectral reflectivity	30, 31
$f(\Theta)$	Energy barrier reduction factor	8
γ	Skewness	31, 52
ΔG^*_het	Critical Gibbs free energy, heterogeneous nucleation	8
ΔG_hom	Gibbs free energy, homogeneous nucleation	7
ΔG^*_hom	Critical Gibbs free energy, homogeneous nucleation	7, 8
i	Index of a node in a binary tree	51
$\Gamma(T)$	Inherent growth ratio	14
A_n	INP surface area	8, 9
$I(\vec{r}_0, \vec{r})$	Radar instrument weighting function	30
$\lvert K\rvert^2$	Dielectric factor	31
$\overline{v}$	Mean Doppler velocity	31, 52, 53
m_i	Ice crystal mass	14
N_{500}	Aerosol particle number concentration for particles $> 500\,\mathrm{nm}$ diameter	30

n_{avg}	Number of averaged spectra	19
N_{i}	Ice crystal number conentration	9–12, 14
N_{l}	Liquid droplet number conentration	8–11, 13
n_{nodes}	Number of nodes	53
$n_{\mathrm{s}}(T)$	Ice active surface site density	8
n_{subpeaks}	Number of subpeaks	53
$\mathrm{d}N_{\mathrm{l}\to\mathrm{i}}$	Nucleation rate	8
$j_{\mathrm{het}}(T,\Theta)$	Nucleation-rate coefficient	8
Ψ	Vertical velocity autocorrelation function	37, 38
$P(\vec{r}_0)$	Received signal by a cloud radar	30
q_{i}	Ice mixing ratio	13
$q_{\mathrm{i},\,0}$	Initial ice mixing ratio	11
q_{l}	Liquid water mixing ratio	13
$q_{\mathrm{l},\,0}$	Initial liquid water mixing ratio	11
q_{v}	Water-vapor mixing ratio	95
r_{a}	Ice crystal radius major semi axis	14, 96
r_{c}	Ice crystal radius minor semi axis	14, 96
t_{max}	Maximum residence time	42
r_G	Radius of the ice cluster	7
r_G^*	Critical radius of the ice cluster	7
ρ_{a}	Density of moist air	95
ρ_{i}	Ice density	14, 95
ρ_{l}	Liquid water density	95
r_{i}	Ice crystal radius	15
$\mathcal{S}_k$	Radar Doppler spectrum sampled at discrete bins	30, 31
S_{500}	Aerosol particle surface area concentration for particles $> 500\,\mathrm{nm}$ diameter	30
ϕ	Saturation difference between liquid water and ice	9, 11, 14, 95
$\mathcal{S}(\vec{r}_0, v)$	Radar Doppler spectrum	30
S_{i}	Supersaturation over ice	10
σ	Spectral width	31, 52
S_{l}	Supersaturation over liquid water	10
$S_{\mathrm{qs,\,l}}$	Quasi-steady supersaturation over liquid water	10
τ_{g}	Glacication time	11, 12

$\tau_{\mathrm{p,\,i}}$	Phase relaxation time for ice	10
$\tau_{\mathrm{p,\,l}}$	Phase relaxation time for liquid water	10
v	Vertical velocity velocity	30, 37
v_{Nyquist}	Nyquist velocity	19
w	Vertical air velocity	10–12
w^0	Threshold vertical velocity of ice mass increase	11, 12
w^+	Threshold vertical velocity of water-vapor mass increase	11, 12
w^*	Threshold vertical velocity of liquid-water mass increase	11–13
Z	Radar reflectivity factor	31, 52, 53, 82

Bibliography

Achtert, P., E. J. O'Connor, I. M. Brooks, G. Sotiropoulou, M. D. Shupe, B. Pospichal, B. J. Brooks, and M. Tjernström. 2020. "Properties of Arctic Liquid and Mixed-Phase Clouds from Shipborne Cloudnet Observations during ACSE 2014." *Atmospheric Chemistry and Physics* 20 (23): 14983–15002. https://doi.org/10.5194/acp-20-14983-2020.

Acquistapace, C., U. Löhnert, M. Maahn, and P. Kollias. 2019. "A New Criterion to Improve Operational Drizzle Detection with Ground-Based Remote Sensing." *Journal of Atmospheric and Oceanic Technology* 36 (5): 781–801. https://doi.org/10.1175/JTECH-D-18-0158.1.

Ahn, E., Y. Huang, S. T. Siems, and M. J. Manton. 2018. "A Comparison of Cloud Microphysical Properties Derived From MODIS and CALIPSO With In Situ Measurements Over the Wintertime Southern Ocean." *Journal of Geophysical Research: Atmospheres* 123 (19): 11, 120–11, 140. https://doi.org/10.1029/2018JD028535.

Alexander, S. P., G. M. McFarquhar, R. Marchand, A. Protat, É. Vignon, G. G. Mace, and A. R. Klekociuk. 2021. "Mixed-phase Clouds and Precipitation in Southern Ocean Cyclones and Cloud Systems Observed Poleward of 64°S by Ship-based Cloud Radar and Lidar." *Journal of Geophysical Research: Atmospheres,* https://doi.org/10.1029/2020JD033626.

Alexander, S. P., A. Orr, S. Webster, and D. J. Murphy. 2017. "Observations and fine-scale model simulations of gravity waves over Davis, East Antarctica (69°S, 78°E)." *Journal of Geophysical Research: Atmospheres* 122 (14): 7355–7370. https://doi.org/10.1002/2017JD026615.

Alexander, S. P., and A. Protat. 2018. "Cloud Properties Observed From the Surface and by Satellite at the Northern Edge of the Southern Ocean." *Journal of Geophysical Research: Atmospheres* 123 (1): 443–456. https://doi.org/10.1002/2017JD026552.

Alexander, S. P., K. Sato, S. Watanabe, Y. Kawatani, and D. J. Murphy. 2016. "Southern Hemisphere Extratropical Gravity Wave Sources and Intermittency Revealed by a Middle-Atmosphere General Circulation Model." *Journal of the Atmospheric Sciences* 73 (3): 1335–1349. https://doi.org/10.1175/JAS-D-15-0149.1.

Althausen, D., R. Engelmann, H. Baars, B. Heese, A. Ansmann, D. Müller, and M. Komppula. 2009. "Portable Raman Lidar PollyXT for Automated Profiling of Aerosol Backscatter, Extinction, and Depolarization." *Journal of Atmospheric and*

Oceanic Technology 26 (11): 2366–2378. https://doi.org/10.1175/2009JTECHA1304.1.

Ansmann, A., P. Seifert, M. Tesche, and U. Wandinger. 2012. "Profiling of Fine and Coarse Particle Mass: Case Studies of Saharan Dust and Eyjafjallajökull/-Grimsvötn Volcanic Plumes." *Atmospheric Chemistry and Physics* 12 (20): 9399–9415. https://doi.org/10.5194/acp-12-9399-2012.

Ansmann, A., M. Tesche, D. Althausen, D. Müller, P. Seifert, V. Freudenthaler, B. Heese, M. Wiegner, G. Pisani, P. Knippertz, and O. Dubovik. 2008. "Influence of Saharan Dust on Cloud Glaciation in Southern Morocco during the Saharan Mineral Dust Experiment." *Journal of Geophysical Research* 113 (D4): D04210. https://doi.org/10.1029/2007JD008785.

Ansmann, A. 2005. "Ice Formation in Saharan Dust over Central Europe Observed with Temperature/Humidity/Aerosol Raman Lidar." *Journal of Geophysical Research* 110 (D18): D18S12. https://doi.org/10.1029/2004JD005000.

Ansmann, A., J. Bösenberg, A. Chaikovsky, A. Comerón, S. Eckhardt, R. Eixmann, V. Freudenthaler, P. Ginoux, L. Komguem, H. Linné, M. Á. L. Márquez, V. Matthias, I. Mattis, V. Mitev, D. Müller, S. Music, S. Nickovic, J. Pelon, L. Sauvage, P. Sobolewsky, M. K. Srivastava, A. Stohl, O. Torres, G. Vaughan, U. Wandinger, and M. Wiegner. 2003. "Long-range transport of Saharan dust to northern Europe: The 11–16 October 2001 outbreak observed with EARLINET." *Journal of Geophysical Research: Atmospheres* 108 (D24): AAC 12. https://doi.org/10.1029/2003JD003757.

Ansmann, A., R.-E. Mamouri, J. Bühl, P. Seifert, R. Engelmann, J. Hofer, A. Nisantzi, J. D. Atkinson, Z. A. Kanji, B. Sierau, M. Vrekoussis, and J. Sciare. 2019. "Ice-Nucleating Particle versus Ice Crystal Number Concentrationin Altocumulus and Cirrus Layers Embedded in Saharan Dust:A Closure Study." *Atmospheric Chemistry and Physics* 19 (23): 15087–15115. https://doi.org/10.5194/acp-19-15087-2019.

Ashbaugh, L. L. 1983. "A Statistical Trajectory Technique for Determining Air Pollution Source Regions." *Journal of the Air Pollution Control Association* 33 (11): 1096–1098. Accessed March 12, 2021. https://doi.org/10.1080/00022470.1983.10465702.

Ashbaugh, L. L., W. C. Malm, and W. Z. Sadeh. 1985. "A residence time probability analysis of sulfur concentrations at grand Canyon National Park." *Atmospheric Environment (1967)* 19 (8): 1263–1270. Accessed March 12, 2021. https://doi.org/10.1016/0004-6981(85)90256-2.

Atlas, D., R. Srivastava, and R. S. Sekhon. 1973. "Doppler radar characteristics of precipitation at vertical incidence." *Reviews of Geophysics* 11 (1): 1–35. https://doi.org/10.1029/RG011i001p00001.

Baars, H., T. Kanitz, R. Engelmann, D. Althausen, B. Heese, M. Komppula, J. Preißler, M. Tesche, A. Ansmann, U. Wandinger, J.-H. Lim, J. Y. Ahn, I. S. Stachlewska, V. Amiridis, E. Marinou, P. Seifert, J. Hofer, A. Skupin, F. Schneider, S. Bohlmann,

A. Foth, S. Bley, A. Pfüller, E. Giannakaki, H. Lihavainen, Y. Viisanen, R. K. Hooda, S. N. Pereira, D. Bortoli, F. Wagner, I. Mattis, L. Janicka, K. M. Markowicz, P. Achtert, P. Artaxo, T. Pauliquevis, R. A. F. Souza, V. P. Sharma, P. G. van Zyl, J. P. Beukes, J. Sun, E. G. Rohwer, R. Deng, R.-E. Mamouri, and F. Zamorano. 2016. "An overview of the first decade of Polly^{NET}: an emerging network of automated Raman-polarization lidars for continuous aerosol profiling." *Atmospheric Chemistry and Physics* 16 (8): 5111–5137. https://doi.org/10.5194/acp-16-5111-2016.

Baars, H., P. Seifert, R. Engelmann, and U. Wandinger. 2017. "Target categorization of aerosol and clouds by continuous multiwavelength-polarization lidar measurements." *Atmospheric Measurement Techniques* 10 (9): 3175–3201. https://doi.org/10.5194/amt-10-3175-2017.

Baars, H., M. Radenz, A. A. Floutsi, R. Engelmann, D. Althausen, B. Heese, A. Ansmann, T. Flament, A. Dabas, D. Trapon, O. Reitebuch, S. Bley, and U. Wandinger. 2021. "Californian Wildfire Smoke Over Europe: A First Example of the Aerosol Observing Capabilities of Aeolus Compared to Ground-Based Lidar." *Geophysical Research Letters* 48 (8). https://doi.org/10.1029/2020GL092194.

Baker, B. A., and R. P. Lawson. 2006. "In Situ Observations of the Microphysical Properties of Wave, Cirrus, and Anvil Clouds. Part I: Wave Clouds." *Journal of the Atmospheric Sciences* 63 (12): 3160–3185. https://doi.org/10.1175/JAS3802.1.

Barreto, Á., E. Cuevas, M.-J. Granados-Muñoz, L. Alados-Arboledas, P. M. Romero, J. Gröbner, N. Kouremeti, A. F. Almansa, T. Stone, C. Toledano, R. Román, M. Sorokin, B. Holben, M. Canini, and M. Yela. 2016. "The New Sun-Sky-Lunar Cimel CE318-T Multiband Photometer – a Comprehensive Performance Evaluation." *Atmospheric Measurement Techniques* 9 (2): 631–654. https://doi.org/10.5194/amt-9-631-2016.

Barrett, A. I., R. J. Hogan, and R. M. Forbes. 2017. "Why Are Mixed-Phase Altocumulus Clouds Poorly Predicted by Large-Scale Models? Part 1. Physical Processes." *Journal of Geophysical Research: Atmospheres* 122 (18): 9903–9926. https://doi.org/10.1002/2016JD026321.

Bodas-Salcedo, A., P. Hill, K. Furtado, K. Williams, P. Field, J. Manners, P. Hyder, and S. Kato. 2016. "Large contribution of supercooled liquid clouds to the solar radiation budget of the Southern Ocean." *Journal of Climate* 29 (11): 4213–4228. https://doi.org/10.1175/JCLI-D-15-0564.1.

Bodas-Salcedo, A., K. D. Williams, M. A. Ringer, I. Beau, J. N. S. Cole, J.-L. Dufresne, T. Koshiro, B. Stevens, Z. Wang, and T. Yokohata. 2014. "Origins of the Solar Radiation Biases over the Southern Ocean in CFMIP2 Models*." *Journal of Climate* 27 (1): 41–56. https://doi.org/10.1175/JCLI-D-13-00169.1.

Bohlmann, S., H. Baars, M. Radenz, R. Engelmann, and A. Macke. 2018. "Ship-Borne Aerosol Profiling with Lidar over the Atlantic Ocean: From Pure Marine Conditions to Complex Dust–Smoke Mixtures." *Atmospheric Chemistry and Physics* 18 (13): 9661–9679. https://doi.org/10.5194/acp-18-9661-2018.

Bourgeois, Q., A. M. L. Ekman, J.-B. Renard, R. Krejci, A. Devasthale, F. A.-M. Bender, I. Riipinen, G. Berthet, and J. L. Tackett. 2018. "How Much of the Global Aerosol Optical Depth Is Found in the Boundary Layer and Free Troposphere?" *Atmospheric Chemistry and Physics* 18 (10): 7709–7720. https://doi.org/10.5194/acp-18-7709-2018.

Bromwich, D. H., K. Werner, B. Casati, J. G. Powers, I. V. Gorodetskaya, F. Massonnet, V. Vitale, V. J. Heinrich, D. Liggett, S. Arndt, B. Barja, E. Bazile, S. Carpentier, J. F. Carrasco, T. Choi, Y. Choi, S. R. Colwell, R. R. Cordero, M. Gervasi, T. Haiden, N. Hirasawa, J. Inoue, T. Jung, H. Kalesse, S.-J. Kim, M. A. Lazzara, K. W. Manning, K. Norris, S.-J. Park, P. Reid, I. Rigor, P. M. Rowe, H. Schmithüsen, P. Seifert, Q. Sun, T. Uttal, M. Zannoni, and X. Zou. 2020. "The Year of Polar Prediction in the Southern Hemisphere (YOPP-SH)." *Bulletin of the American Meteorological Society* 101 (10): E1653–E1676. https://doi.org/10.1175/BAMS-D-19-0255.1.

Broxton, P. D., X. Zeng, D. Sulla-Menashe, and P. A. Troch. 2014. "A Global Land Cover Climatology Using MODIS Data." *Journal of Applied Meteorology and Climatology* 53 (6): 1593–1605. https://doi.org/10.1175/JAMC-D-13-0270.1.

Bühl, J., A. Ansmann, P. Seifert, H. Baars, and R. Engelmann. 2013a. "Toward a quantitative characterization of heterogeneous ice formation with lidar/radar: Comparison of CALIPSO/CloudSat with ground-based observations." *Geophysical Research Letters* 40 (16): 4404–4408. https://doi.org/10.1002/grl.50792.

Bühl, J., R. Leinweber, U. Görsdorf, M. Radenz, A. Ansmann, and V. Lehmann. 2015. "Combined Vertical-Velocity Observations with Doppler Lidar, Cloud Radar and Wind Profiler." *Atmospheric Measurement Techniques* 8 (8): 3527–3536. https://doi.org/10.5194/amt-8-3527-2015.

Bühl, J., P. Seifert, A. Myagkov, and A. Ansmann. 2016. "Measuring ice- and liquid-water properties in mixed-phase cloud layers at the Leipzig Cloudnet station." *Atmospheric Chemistry and Physics* 16 (16): 10609–10620. https://doi.org/10.5194/acp-16-10609-2016.

Bühl, J., M. Radenz, W. Schimmel, T. Vogl, J. Röttenbacher, and M. Lochmann. 2021. "pyLARDA v3.2." https://doi.org/10.5281/zenodo.4721311.

Bühl, J., P. Seifert, R. Engelmann, and A. Ansmann. 2019a. "Impact of vertical air motions on ice formation rate in mixed-phase cloud layers." *npj Climate and Atmospheric Science* 2, no. 1 (December): 36. https://doi.org/10.1038/s41612-019-0092-6.

Bühl, J., P. Seifert, M. Radenz, H. Baars, and A. Ansmann. 2019b. "Ice Crystal Number Concentration from Lidar, Cloud Radar and Radar Wind Profiler Measurements." *Atmospheric Measurement Techniques* 12 (12): 6601–6617. https://doi.org/10.5194/amt-12-6601-2019.

Bühl, J., P. Seifert, U. Wandinger, H. Baars, T. Kanitz, J. Schmidt, A. Myagkov, R. Engelmann, A. Skupin, B. Heese, A. Klepel, D. Althausen, and A. Ansmann. 2013b. "LACROS: The Leipzig Aerosol and Cloud Remote Observations System."

In *SPIE Remote Sensing,* edited by A. Comeron, E. I. Kassianov, K. Schäfer, K. Stein, and J. D. Gonglewski, 889002. Dresden, Germany. https://doi.org/10.1117/12.2030911.

Burton, S. P., R. A. Ferrare, C. A. Hostetler, J. W. Hair, R. R. Rogers, M. D. Obland, C. F. Butler, A. L. Cook, D. B. Harper, and K. D. Froyd. 2012. "Aerosol classification using airborne High Spectral Resolution Lidar measurements – methodology and examples." *Atmospheric Measurement Techniques* 5 (1): 73–98. https://doi.org/10.5194/amt-5-73-2012.

Cazenave, Q., M. Ceccaldi, J. Delanoë, J. Pelon, S. Groß, and A. Heymsfield. 2019. "Evolution of DARDAR-CLOUD Ice Cloud Retrievals: New Parameters and Impacts on the Retrieved Microphysical Properties." *Atmospheric Measurement Techniques* 12 (5): 2819–2835. https://doi.org/10.5194/amt-12-2819-2019.

Chen, J.-P., and D. Lamb. 1994. "The Theoretical Basis for the Parameterization of Ice Crystal Habits: Growth by Vapor Deposition." *Journal of Atmospheric Sciences* 51 (9): 1206–1222. https://doi.org/10.1175/1520-0469(1994)051<1206:TTBFTP>2.0.CO;2.

Choi, Y.-S., R. S. Lindzen, C.-H. Ho, and J. Kim. 2010. "Space observations of cold-cloud phase change." *Proceedings of the National Academy of Sciences* 107 (25): 11211–11216. https://doi.org/10.1073/pnas.1006241107.

Clothiaux, E. E., T. P. Ackerman, G. G. Mace, K. P. Moran, R. T. Marchand, M. A. Miller, and B. E. Martner. 2000. "Objective Determination of Cloud Heights and Radar Reflectivities Using a Combination of Active Remote Sensors at the ARM CART Sites." *Journal of Applied Meteorology* 39 (5): 645–665. https://doi.org/10.1175/1520-0450(2000)039<0645:ODOCHA>2.0.CO;2.

Conen, F., C. E. Morris, J. Leifeld, M. V. Yakutin, and C. Alewell. 2011. "Biological Residues Define the Ice Nucleation Properties of Soil Dust." *Atmospheric Chemistry and Physics* 11 (18): 9643–9648. https://doi.org/10.5194/acp-11-9643-2011.

Connolly, P. J., O. Möhler, P. R. Field, H. Saathoff, R. Burgess, T. Choularton, and M. Gallagher. 2009. "Studies of Heterogeneous Freezing by Three Different Desert Dust Samples." *Atmospheric Chemistry and Physics* 9 (8): 2805–2824. https://doi.org/10.5194/acp-9-2805-2009.

Cotton, R. J., and P. R. Field. 2002. "Ice nucleation characteristics of an isolated wave cloud." *Quarterly Journal of the Royal Meteorological Society* 128 (585): 2417–2437. https://doi.org/10.1256/qj.01.150.

Crewell, S., and U. Löhnert. 2007. "Accuracy of Boundary Layer Temperature Profiles Retrieved With Multifrequency Multiangle Microwave Radiometry." *IEEE Transactions on Geoscience and Remote Sensing* 45 (7): 2195–2201. https://doi.org/10.1109/TGRS.2006.888434.

D'Alessandro, J. J., M. Diao, C. Wu, X. Liu, J. B. Jensen, and B. B. Stephens. 2019. "Cloud Phase and Relative Humidity Distributions over the Southern Ocean in Austral Summer Based on In Situ Observations and CAM5 Simulations." *Journal*

of Climate (Boston MA, USA) 32 (10): 2781–2805. https://doi.org/10.1175/JCLI-D-18-0232.1.

de Boer, G., E. W. Eloranta, and M. D. Shupe. 2009. "Arctic Mixed-Phase Stratiform Cloud Properties from Multiple Years of Surface-Based Measurements at Two High-Latitude Locations." *Journal of the Atmospheric Sciences* 66 (9): 2874–2887. https://doi.org/10.1175/2009JAS3029.1.

DeMott, P. J., A. J. Prenni, X. Liu, S. M. Kreidenweis, M. D. Petters, C. H. Twohy, M. S. Richardson, T. Eidhammer, and D. C. Rogers. 2010. "Predicting global atmospheric ice nuclei distributions and their impacts on climate." *Proceedings of the National Academy of Sciences* 107 (25): 11217–11222. https://doi.org/10.1073/pnas.0910818107.

DeMott, P. J., A. J. Prenni, G. R. McMeeking, R. C. Sullivan, M. D. Petters, Y. Tobo, M. Niemand, O. Möhler, J. R. Snider, Z. Wang, and S. M. Kreidenweis. 2015. "Integrating laboratory and field data to quantify the immersion freezing ice nucleation activity of mineral dust particles." *Atmospheric Chemistry and Physics* 15 (1): 393–409. https://doi.org/10.5194/acp-15-393-2015.

Desai, N., K. K. Chandrakar, G. Kinney, W. Cantrell, and R. A. Shaw. 2019. "Aerosol-Mediated Glaciation of Mixed-Phase Clouds: Steady-State Laboratory Measurements." *Geophysical Research Letters* 46 (15): 9154–9162. https://doi.org/10.1029/2019GL083503.

Diehl, K., and S. K. Mitra. 2015. "New Particle-Dependent Parameterizations of Heterogeneous Freezing Processes: Sensitivity Studies of Convective Clouds with an Air Parcel Model." *Atmospheric Chemistry and Physics* 15 (22): 12741–12763. https://doi.org/10.5194/acp-15-12741-2015.

Doviak, R. J., and D. S. Zrnic. 1993. *Doppler Radar & Weather Observations.* Courier Corporation. https://doi.org/10.1016/C2009-0-22358-0.

Draxler, R. R. 2003. "Evaluation of an Ensemble Dispersion Calculation." *Journal of Applied Meteorology* 42 (2): 308–317. Accessed March 15, 2017. https://doi.org/10.1175/1520-0450(2003)042<0308:EOAEDC>2.0.CO;2.

Durant, A. J. 2005. "Evaporation Freezing by Contact Nucleation Inside-Out." *Geophysical Research Letters* 32 (20): L20814. https://doi.org/10.1029/2005GL024175.

Durre, I., R. S. Vose, and D. B. Wuertz. 2006. "Overview of the Integrated Global Radiosonde Archive." *Journal of Climate* 19 (1): 53–68. https://doi.org/10.1175/JCLI3594.1.

Durre, I., X. Yin, R. S. Vose, S. Applequist, and J. Arnfield. 2018. "Enhancing the Data Coverage in the Integrated Global Radiosonde Archive." *Journal of Atmospheric and Oceanic Technology* 35 (9): 1753–1770. https://doi.org/10.1175/JTECH-D-17-0223.1.

Engelmann, R., A. Ansmann, K. Ohneiser, H. Griesche, M. Radenz, J. Hofer, D. Althausen, S. Dahlke, M. Maturilli, I. Veselovskii, C. Jimenez, R. Wiesen, H. Baars,

J. Bühl, H. Gebauer, M. Haarig, P. Seifert, U. Wandinger, and A. Macke. 2021. "Wildfire Smoke, Arctic Haze, and Aerosol Effects on Mixed-Phase and Cirrus Clouds over the North Pole Region during MOSAiC: An Introduction." *Atmospheric Chemistry and Physics* 21 (17): 13397–13423. https://doi.org/10.5194/acp-21-13397-2021.

Engelmann, R., T. Kanitz, H. Baars, B. Heese, D. Althausen, A. Skupin, U. Wandinger, M. Komppula, I. S. Stachlewska, V. Amiridis, E. Marinou, I. Mattis, H. Linné, and A. Ansmann. 2016. "The automated multiwavelength Raman polarization and water-vapor lidar Polly^{XT}: the neXT generation." *Atmospheric Measurement Techniques* 9 (4): 1767–1784. https://doi.org/10.5194/amt-9-1767-2016.

Escudero, M., A. Stein, R. Draxler, X. Querol, A. Alastuey, S. Castillo, and A. Avila. 2011. "Source apportionment for African dust outbreaks over the Western Mediterranean using the HYSPLIT model." *Atmospheric Research* 99 (3-4): 518–527. https://doi.org/10.1016/j.atmosres.2010.12.002.

Fan, J., Y. Wang, D. Rosenfeld, and X. Liu. 2016. "Review of Aerosol–Cloud Interactions: Mechanisms, Significance, and Challenges." *Journal of the Atmospheric Sciences* (Boston MA, USA) 73 (11): 4221–4252. https://doi.org/10.1175/JAS-D-16-0037.1.

Fang, M., B. A. Albrecht, V. P. Ghate, and P. Kollias. 2014. "Turbulence in Continental Stratocumulus, Part I: External Forcings and Turbulence Structures." *Boundary-Layer Meteorology* 150 (3): 341–360. https://doi.org/10.1007/s10546-013-9873-3.

Fernald, F. G. 1984. "Analysis of Atmospheric Lidar Observations: Some Comments." *Applied optics* 23 (5): 652–653.

Field, P. R., A. J. Heymsfield, B. J. Shipway, P. J. DeMott, K. A. Pratt, D. C. Rogers, J. Stith, and K. A. Prather. 2012. "Ice in Clouds Experiment–Layer Clouds. Part II: Testing Characteristics of Heterogeneous Ice Formation in Lee Wave Clouds." *Journal of the Atmospheric Sciences* 69 (3): 1066–1079. https://doi.org/10.1175/JAS-D-11-026.1.

Field, P. R., A. A. Hill, K. Furtado, and A. Korolev. 2014. "Mixed-Phase Clouds in a Turbulent Environment. Part 2: Analytic Treatment: Mixed-Phase Clouds in a Turbulent Environment. Part 2." *Quarterly Journal of the Royal Meteorological Society* 140 (680): 870–880. https://doi.org/10.1002/qj.2175.

Fleming, Z. L., P. S. Monks, and A. J. Manning. 2012. "Review: Untangling the influence of air-mass history in interpreting observed atmospheric composition." *Atmospheric Research* 104-105:1–39. https://doi.org/10.1016/j.atmosres.2011.09.009.

Floutsi, A. A., H. Baars, M. Radenz, M. Haarig, Z. Yin, P. Seifert, C. Jimenez, A. Ansmann, R. Engelmann, B. Barja, F. Zamorano, and U. Wandinger. 2021. "Advection of Biomass Burning Aerosols towards the Southern Hemispheric Mid-Latitude Station of Punta Arenas as Observed with Multiwavelength Polarization Raman Lidar." *Remote Sensing* 13 (1): 138. https://doi.org/10.3390/rs13010138.

Foth, A., T. Kanitz, R. Engelmann, H. Baars, M. Radenz, P. Seifert, B. Barja, M. Fromm, H. Kalesse, and A. Ansmann. 2019. "Vertical aerosol distribution in the

southern hemispheric midlatitudes as observed with lidar in Punta Arenas, Chile (53.2°S and 70.9°W), during ALPACA." *Atmospheric Chemistry and Physics* 19 (9): 6217–6233. https://doi.org/10.5194/acp-19-6217-2019.

Franklin, C. N., Z. Sun, D. Bi, M. Dix, H. Yan, and A. Bodas-Salcedo. 2013. "Evaluation of clouds in ACCESS using the satellite simulator package COSP: Global, seasonal, and regional cloud properties." *Journal of Geophysical Research: Atmospheres* 118 (2): 732–748. https://doi.org/10.1029/2012JD018469.

Freudenthaler, V. 2016. "About the Effects of Polarising Optics on Lidar Signals and the Δ90 Calibration." *Atmospheric Measurement Techniques* 9 (9): 4181–4255. https://doi.org/10.5194/amt-9-4181-2016.

Friedl, M., D. McIver, J. Hodges, X. Zhang, D. Muchoney, A. Strahler, C. Woodcock, S. Gopal, A. Schneider, A. Cooper, A. Baccini, F. Gao, and C. Schaaf. 2002. "Global land cover mapping from MODIS: algorithms and early results." *Remote Sensing of Environment* 83 (1-2): 287–302. Accessed March 12, 2021. https://doi.org/10.1016/S0034-4257(02)00078-0.

Frölicher, T. L., J. L. Sarmiento, D. J. Paynter, J. P. Dunne, J. P. Krasting, and M. Winton. 2015. "Dominance of the Southern Ocean in Anthropogenic Carbon and Heat Uptake in CMIP5 Models." *Journal of Climate* 28 (2): 862–886. https://doi.org/10.1175/JCLI-D-14-00117.1.

Fukuta, N., and L. A. Walter. 1970. "Kinetics of Hydrometeor Growth from a Vapor-Spherical Model." *Journal of Atmospheric Sciences* (Boston MA, USA) 27 (8): 1160–1172. https://doi.org/10.1175/1520-0469(1970)027¡1160:KOHGFA¿2.0.CO;2.

Fukuta, N., and T. Takahashi. 1999. "The Growth of Atmospheric Ice Crystals: A Summary of Findings in Vertical Supercooled Cloud Tunnel Studies." *Journal of the Atmospheric Sciences* 56 (12): 1963–1979. https://doi.org/10.1175/1520-0469(1999)056<1963:TGOAIC>2.0.CO;2.

Garnier, R., and J. Taylor. 2009. *Discrete Mathematics: Proofs, Structures and Applications, Third Edition.* Hoboken: CRC Press. ISBN: 978-1-4398-1281-5.

Gayet, J.-F., J. Ovarlez, V. Shcherbakov, J. Ström, U. Schumann, A. Minikin, F. Auriol, A. Petzold, and M. Monier. 2004. "Cirrus Cloud Microphysical and Optical Properties at Southern and Northern Midlatitudes during the INCA Experiment." *Journal of Geophysical Research: Atmospheres* 109 (D20). https://doi.org/10.1029/2004JD004803. eprint: https://agupubs.onlinelibrary.wiley.com/doi/pdf/10.1029/2004JD004803.

Görsdorf, U., V. Lehmann, M. Bauer-Pfundstein, G. Peters, D. Vavriv, V. Vinogradov, and V. Volkov. 2015. "A 35-GHz Polarimetric Doppler Radar for Long-Term Observations of Cloud Parameters—Description of System and Data Processing." *Journal of Atmospheric and Oceanic Technology* 32 (4): 675–690. https://doi.org/10.1175/JTECH-D-14-00066.1.

Griesche, H. J., K. Ohneiser, P. Seifert, M. Radenz, R. Engelmann, and A. Ansmann. 2021. "Contrasting Ice Formation in Arctic Clouds: Surface-Coupled vs. Surface-

Decoupled Clouds." *Atmospheric Chemistry and Physics* 21 (13): 10357–10374. https://doi.org/10.5194/acp-21-10357-2021.

Griesche, H. J., P. Seifert, A. Ansmann, H. Baars, C. Barrientos Velasco, J. Bühl, R. Engelmann, M. Radenz, Y. Zhenping, and A. Macke. 2020. "Application of the Shipborne Remote Sensing Supersite OCEANET for Profiling of Arctic Aerosols and Clouds during Polarstern Cruise PS106." *Atmospheric Measurement Techniques* 13 (10): 5335–5358. https://doi.org/10.5194/amt-13-5335-2020.

Grise, K. M., L. M. Polvani, and J. T. Fasullo. 2015. "Reexamining the Relationship between Climate Sensitivity and the Southern Hemisphere Radiation Budget in CMIP Models." *Journal of Climate* 28 (23): 9298–9312. https://doi.org/10.1175/JCLI-D-15-0031.1.

Groß, S., M. Esselborn, B. Weinzierl, M. Wirth, A. Fix, and A. Petzold. 2013. "Aerosol classification by airborne high spectral resolution lidar observations." *Atmospheric Chemistry and Physics* 13 (5): 2487–2505. https://doi.org/10.5194/acp-13-2487-2013.

Haarig, M., A. Ansmann, H. Baars, C. Jimenez, I. Veselovskii, R. Engelmann, and D. Althausen. 2018a. "Depolarization and lidar ratios at 355, 532, and 1064 nm and microphysical properties of aged tropospheric and stratospheric Canadian wildfire smoke." *Atmospheric Chemistry and Physics* 18 (16): 11847–11861. https://doi.org/10.5194/acp-18-11847-2018.

Haarig, M., A. Ansmann, J. Gasteiger, K. Kandler, D. Althausen, H. Baars, M. Radenz, and D. A. Farrell. 2017. "Dry versus wet marine particle optical properties: RH dependence of depolarization ratio, backscatter, and extinction from multiwavelength lidar measurements during SALTRACE." *Atmospheric Chemistry and Physics* 17 (23): 14199–14217. https://doi.org/10.5194/acp-17-14199-2017.

Haarig, M., A. Ansmann, H. Baars, C. Jimenez, I. Veselovskii, R. Engelmann, and D. Althausen. 2018b. "Depolarization and Lidar Ratios at 355, 532, and 1064 Nm and Microphysical Properties of Aged Tropospheric and Stratospheric Canadian Wildfire Smoke." *Atmospheric Chemistry and Physics* 18 (16): 11847–11861. https://doi.org/10.5194/acp-18-11847-2018.

Hall, W. D., and H. R. Pruppacher. 1976. "The Survival of Ice Particles Falling from Cirrus Clouds in Subsaturated Air." *Journal of the Atmospheric Sciences* 33 (10): 1995–2006. https://doi.org/10.1175/1520-0469(1976)033<1995:TSOIPF>2.0.CO;2.

Hamilton, D. S., L. A. Lee, K. J. Pringle, C. L. Reddington, D. V. Spracklen, and K. S. Carslaw. 2014. "Occurrence of pristine aerosol environments on a polluted planet." *Proceedings of the National Academy of Sciences* 111 (52): 18466–18471. https://doi.org/10.1073/pnas.1415440111.

Heintzenberg, J., W. Birmili, P. Seifert, A. Panov, X. Chi, and M. O. Andreae. 2013. "Mapping the Aerosol over Eurasia from the Zotino Tall Tower." *Tellus B: Chem-*

ical and Physical Meteorology 65 (1): 20062. https://doi.org/10.3402/tellusb.v65i0.20062.

Heymsfield, A. J., and C. D. Westbrook. 2010. "Advances in the Estimation of Ice Particle Fall Speeds Using Laboratory and Field Measurements." *Journal of the Atmospheric Sciences* 67 (8): 2469–2482. https://doi.org/10.1175/2010JAS3379.1.

Heymsfield, A. J., and L. M. Miloshevich. 1993. "Homogeneous Ice Nucleation and Supercooled Liquid Water in Orographic Wave Clouds." *Journal of the Atmospheric Sciences* 50 (15): 2335–2353. https://doi.org/10.1175/1520-0469(1993)050<2335:HINASL>2.0.CO;2.

Hildebrand, P. H., and R. S. Sekhon. 1974. "Objective Determination of the Noise Level in Doppler Spectra." *Journal of Applied Meteorology and Climatology* (Boston MA, USA) 13 (7): 808–811. https://doi.org/10.1175/1520-0450(1974)013¡0808:ODOTNL¿2.0.CO;2.

Hogan, R. J., M. P. Mittermaier, and A. J. Illingworth. 2006. "The Retrieval of Ice Water Content from Radar Reflectivity Factor and Temperature and Its Use in Evaluating a Mesoscale Model." *Journal of Applied Meteorology and Climatology* 45 (2): 301–317. https://doi.org/10.1175/jam2340.1.

Hogan, R. J., and E. J. O'Connor. 2004. *Facilitating cloud radar and lidar algorithms: the Cloudnet Instrument Synergy/Target Categorization product.* Tech. rep. University of Reading, Department of Meteorology. Accessed February 3, 2021. http://www.met.rdg.ac.uk/~swrhgnrj/publications/categorization.pdf.

Hoose, C., and O. Möhler. 2012. "Heterogeneous Ice Nucleation on Atmospheric Aerosols: A Review of Results from Laboratory Experiments." *Atmospheric Chemistry and Physics* 12 (20): 9817–9854. https://doi.org/10.5194/acp-12-9817-2012.

Hu, Y., S. Rodier, K.-m. Xu, W. Sun, J. Huang, B. Lin, P. Zhai, and D. Josset. 2010. "Occurrence, liquid water content, and fraction of supercooled water clouds from combined CALIOP/IIR/MODIS measurements." *Journal of Geophysical Research: Atmospheres* 115 (D4): D00H34. https://doi.org/10.1029/2009JD012384.

Huang, Y., T. Chubb, D. Baumgardner, M. deHoog, S. T. Siems, and M. J. Manton. 2017. "Evidence for Secondary Ice Production in Southern Ocean Open Cellular Convection: Secondary Ice Production over the Southern Ocean." *Quarterly Journal of the Royal Meteorological Society* 143 (704): 1685–1703. https://doi.org/10.1002/qj.3041.

Huang, Y., A. Protat, S. T. Siems, and M. J. Manton. 2015. "A-Train Observations of Maritime Midlatitude Storm-Track Cloud Systems: Comparing the Southern Ocean against the North Atlantic." *Journal of Climate* 28 (5): 1920–1939. https://doi.org/10.1175/JCLI-D-14-00169.1.

Hyder, P., J. M. Edwards, R. P. Allan, H. T. Hewitt, T. J. Bracegirdle, J. M. Gregory, R. A. Wood, A. J. S. Meijers, J. Mulcahy, P. Field, K. Furtado, A. Bodas-Salcedo, K. D. Williams, D. Copsey, S. A. Josey, C. Liu, C. D. Roberts, C. Sanchez, J. Ridley, L. Thorpe, S. C. Hardiman, M. Mayer, D. I. Berry, and S. E. Belcher. 2018. "Critical Southern Ocean Climate Model Biases Traced to Atmospheric

Model Cloud Errors." *Nature Communications* 9 (1): 3625. https://doi.org/10.1038/s41467-018-05634-2.

Illingworth, A. J., R. J. Hogan, E. J. O'Connor, D. Bouniol, J. Delanoë, J. Pelon, A. Protat, M. E. Brooks, N. Gaussiat, D. R. Wilson, D. P. Donovan, H. K. Baltink, G.-J. van Zadelhoff, J. D. Eastment, J. W. F. Goddard, C. L. Wrench, M. Haeffelin, O. A. Krasnov, H. W. J. Russchenberg, J.-M. Piriou, F. Vinit, A. Seifert, A. M. Tompkins, and U. Willén. 2007. "Cloudnet: Continuous Evaluation of Cloud Profiles in Seven Operational Models Using Ground-Based Observations." *Bulletin of the American Meteorological Society* 88 (6): 883–898. Accessed February 29, 2016. https://doi.org/10.1175/BAMS-88-6-883.

Jimenez, C., A. Ansmann, R. Engelmann, D. Donovan, A. Malinka, J. Schmidt, P. Seifert, and U. Wandinger. 2020a. "The Dual-Field-of-View Polarization Lidar Technique: A New Concept in Monitoring Aerosol Effects in Liquid-Water Clouds – Theoretical Framework." *Atmospheric Chemistry and Physics* 20 (23): 15247–15263. https://doi.org/10.5194/acp-20-15247-2020.

Jimenez, C., A. Ansmann, R. Engelmann, D. Donovan, A. Malinka, P. Seifert, R. Wiesen, M. Radenz, Z. Yin, J. Bühl, J. Schmidt, B. Barja, and U. Wandinger. 2020b. "The Dual-Field-of-View Polarization Lidar Technique: A New Concept in Monitoring Aerosol Effects in Liquid-Water Clouds – Case Studies." *Atmospheric Chemistry and Physics* 20 (23): 15265–15284. https://doi.org/10.5194/acp-20-15265-2020.

Kahl, J. D. 1993. "A cautionary note on the use of air trajectories in interpreting atmospheric chemistry measurements." *Atmospheric Environment. Part A. General Topics* 27 (17-18): 3037–3038. Accessed March 12, 2021. https://doi.org/10.1016/0960-1686(93)90336-W.

Kalesse, H., T. Vogl, C. Paduraru, and E. Luke. 2019. "Development and validation of a supervised machine learning radar Doppler spectra peak finding algorithm." *Atmospheric Measurement Techniques Discussions* 2019:1–37. https://doi.org/10.5194/amt-2019-48.

Kanitz, T., P. Seifert, A. Ansmann, R. Engelmann, D. Althausen, C. Casiccia, and E. G. Rohwer. 2011. "Contrasting the impact of aerosols at northern and southern midlatitudes on heterogeneous ice formation." *Geophysical Research Letters* 38 (17): L17802. https://doi.org/10.1029/2011gl048532.

Kanji, Z. A., L. A. Ladino, H. Wex, Y. Boose, M. Burkert-Kohn, D. J. Cziczo, and M. Krämer. 2017. "Overview of Ice Nucleating Particles." *Meteorological Monographs* 58:1.1–1.33. https://doi.org/10.1175/AMSMONOGRAPHS-D-16-0006.1.

Kay, J. E., L. Bourdages, N. B. Miller, A. Morrison, V. Yettella, H. Chepfer, and B. Eaton. 2016. "Evaluating and improving cloud phase in the Community Atmosphere Model version 5 using spaceborne lidar observations." *Journal of Geophysical Research: Atmospheres* 121 (8): 4162–4176. https://doi.org/10.1002/2015JD024699.

Kinne, S. 2019. “The MACv2 Aerosol Climatology.” *Tellus B: Chemical and Physical Meteorology* 71 (1): 1–21. https://doi.org/10.1080/16000889.2019.1623639.

Kneifel, S., M. Maahn, G. Peters, and C. Simmer. 2011. “Observation of snowfall with a low-power FM-CW K-band radar (Micro Rain Radar).” *Meteorol. Atmos. Phys.* 113:75–87. https://doi.org/10.1007/s00703-011-0142-z.

Kollias, P., M. A. Miller, E. P. Luke, K. L. Johnson, E. E. Clothiaux, K. P. Moran, K. B. Widener, and B. A. Albrecht. 2007. “The Atmospheric Radiation Measurement Program Cloud Profiling Radars: Second-Generation Sampling Strategies, Processing, and Cloud Data Products.” *Journal of Atmospheric and Oceanic Technology* 24 (7): 1199–1214. https://doi.org/10.1175/JTECH2033.1.

Korolev, A., G. McFarquhar, P. R. Field, C. Franklin, P. Lawson, Z. Wang, E. Williams, S. J. Abel, D. Axisa, S. Borrmann, J. Crosier, J. Fugal, M. Krämer, U. Lohmann, O. Schlenczek, M. Schnaiter, and M. Wendisch. 2017. “Mixed-Phase Clouds: Progress and Challenges.” *Meteorological Monographs* 58:5.1–5.50. https://doi.org/10.1175/AMSMONOGRAPHS-D-17-0001.1.

Korolev, A. 2007. “Limitations of the Wegener–Bergeron–Findeisen Mechanism in the Evolution of Mixed-Phase Clouds.” *Journal of the Atmospheric Sciences* 64, no. 9 (September 1, 2007): 3372–3375. Accessed March 7, 2021. https://doi.org/10.1175/JAS4035.1.

———. 2008. “Rates of Phase Transformations in Mixed-Phase Clouds.” *Quarterly Journal of the Royal Meteorological Society* 134 (632): 595–608. https://doi.org/10.1002/qj.230.

Korolev, A., and P. Field. 2008. “The Effect of Dynamics on Mixed-Phase Clouds: Theoretical Considerations.” *Journal of the Atmospheric Sciences* 65 (1): 66–86. https://doi.org/10.1175/2007JAS2355.1.

Korolev, A., and G. Isaac. 2003. “Phase Transformation of Mixed-Phase Clouds.” *Quarterly Journal of the Royal Meteorological Society* 129 (587): 19–38. https://doi.org/10.1256/qj.01.203.

Korolev, A., and I. Mazin. 2003. “Supersaturation of Water Vapor in Clouds.” *Journal of the Atmospheric Sciences* 60 (24): 2957–2974. https://doi.org/10.1175/1520-0469(2003)060¡2957:SOWVIC¿2.0.CO;2.

Kuma, P., A. J. McDonald, O. Morgenstern, S. P. Alexander, J. J. Cassano, S. Garrett, J. Halla, S. Hartery, M. J. Harvey, S. Parsons, G. Plank, V. Varma, and J. Williams. 2020. “Evaluation of Southern Ocean cloud in the HadGEM3 general circulation model and MERRA-2 reanalysis using ship-based observations.” *Atmospheric Chemistry and Physics* 20 (11): 6607–6630. https://doi.org/10.5194/acp-20-6607-2020.

Liu, Y., B. Geerts, M. Miller, P. Daum, and R. McGraw. 2008. “Threshold Radar Reflectivity for Drizzling Clouds.” *Geophysical Research Letters* 35 (3): L03807. https://doi.org/10.1029/2007GL031201.

Löffler-Mang, M., and J. Joss. 2000. "An Optical Disdrometer for Measuring Size and Velocity of Hydrometeors." *Journal of Atmospheric and Oceanic Technology* 17 (2): 130–139. https://doi.org/10.1175/1520-0426(2000)017<0130:AODFMS>2.0.CO;2.

Lu, Z., D. G. Streets, Q. Zhang, and S. Wang. 2012. "A novel back-trajectory analysis of the origin of black carbon transported to the Himalayas and Tibetan Plateau during 1996-2010." *Geophysical Research Letters* 39 (1). https://doi.org/10.1029/2011GL049903.

Luke, E. P., and P. Kollias. 2013. "Separating Cloud and Drizzle Radar Moments during Precipitation Onset Using Doppler Spectra." *Journal of Atmospheric and Oceanic Technology* 30 (8): 1656–1671. Accessed April 12, 2017. https://doi.org/10.1175/JTECH-D-11-00195.1.

Luke, E. P., P. Kollias, K. L. Johnson, and E. E. Clothiaux. 2008. "A Technique for the Automatic Detection of Insect Clutter in Cloud Radar Returns." *Journal of Atmospheric and Oceanic Technology* 25 (9): 1498–1513. https://doi.org/10.1175/2007JTECHA953.1.

Luke, E. P., P. Kollias, and M. D. Shupe. 2010. "Detection of supercooled liquid in mixed-phase clouds using radar Doppler spectra." *Journal of Geophysical Research* 115 (D19). Accessed September 2, 2018. https://doi.org/10.1029/2009JD012884.

Mace, G. G., S. Benson, and Y. Hu. 2020. "On the Frequency of Occurrence of the Ice Phase in Supercooled Southern Ocean Low Clouds Derived From CALIPSO and CloudSat." *Geophysical Research Letters* 47 (14). https://doi.org/10.1029/2020GL087554.

Mace, G. G., and A. Protat. 2018. "Clouds over the Southern Ocean as Observed from the R/V Investigator during CAPRICORN. Part I: Cloud Occurrence and Phase Partitioning." *Journal of Applied Meteorology and Climatology* 57 (8): 1783–1803. https://doi.org/10.1175/JAMC-D-17-0194.1.

Mamouri, R. E., A. Ansmann, A. Nisantzi, P. Kokkalis, A. Schwarz, and D. Hadjimitsis. 2013. "Low Arabian dust extinction-to-backscatter ratio." *Geophysical Research Letters* 40 (17): 4762–4766. https://doi.org/10.1002/grl.50898.

Mamouri, R.-E., and A. Ansmann. 2016. "Potential of polarization lidar to provide profiles of CCN- and INP-relevant aerosol parameters." *Atmospheric Chemistry and Physics* 16 (9): 5905–5931. https://doi.org/10.5194/acp-16-5905-2016.

———. 2017. "Potential of polarization/Raman lidar to separate fine dust, coarse dust, maritime, and anthropogenic aerosol profiles." *Atmospheric Measurement Techniques* 10 (9): 3403–3427. https://doi.org/10.5194/amt-10-3403-2017.

McCluskey, C. S., T. C. J. Hill, R. S. Humphries, A. M. Rauker, S. Moreau, P. G. Strutton, S. D. Chambers, A. G. Williams, I. McRobert, J. Ward, M. D. Keywood, J. Harnwell, W. Ponsonby, Z. M. Loh, P. B. Krummel, A. Protat, S. M. Kreidenweis, and P. J. DeMott. 2018a. "Observations of Ice Nucleating Particles Over Southern Ocean Waters." *Geophysical Research Letters* 45 (21): 11, 989–11, 997. https://doi.org/10.1029/2018GL079981.

McCluskey, C. S., J. Ovadnevaite, M. Rinaldi, J. Atkinson, F. Belosi, D. Ceburnis, S. Marullo, T. C. J. Hill, U. Lohmann, Z. A. Kanji, C. O'Dowd, S. M. Kreidenweis, and P. J. DeMott. 2018b. "Marine and Terrestrial Organic Ice-Nucleating Particles in Pristine Marine to Continentally Influenced Northeast Atlantic Air Masses." *Journal of Geophysical Research: Atmospheres* 123 (11): 6196–6212. https://doi.org/10.1029/2017JD028033.

McCoy, D. T., D. L. Hartmann, M. D. Zelinka, P. Ceppi, and D. P. Grosvenor. 2015. "Mixed-phase Cloud Physics and Southern Ocean Cloud Feedback in Climate Models." *Journal of Geophysical Research: Atmospheres* 120 (18): 9539–9554. https://doi.org/10.1002/2015JD023603.

McErlich, C., A. McDonald, A. Schuddeboom, and I. Silber. 2021. "Comparing Satellite- and Ground-Based Observations of Cloud Occurrence Over High Southern Latitudes." *Journal of Geophysical Research: Atmospheres* 126 (6). https://doi.org/10.1029/2020JD033607.

McFarquhar, G. M., C. Bretherton, R. Marchand, A. Protat, P. J. DeMott, S. P. Alexander, G. C. Roberts, et al. 2020. "Observations of Clouds, Aerosols, Precipitation, and Surface Radiation over the Southern Ocean: An Overview of CAPRICORN, MARCUS, MICRE and SOCRATES." *Bulletin of the American Meteorological Society,* 1–92. https://doi.org/10.1175/BAMS-D-20-0132.1.

Merrill, J. T., R. Bleck, and L. Avila. 1985. "Modeling atmospheric transport to the Marshall Islands." *Journal of Geophysical Research* 90 (D7): 12927. Accessed March 12, 2021. https://doi.org/10.1029/JD090iD07p12927.

Minikin, A., A. Petzold, J. Ström, R. Krejci, M. Seifert, P. van Velthoven, H. Schlager, and U. Schumann. 2003. "Aircraft Observations of the Upper Tropospheric Fine Particle Aerosol in the Northern and Southern Hemispheres at Midlatitudes." *Geophysical Research Letters* 30 (10): n/a–n/a. https://doi.org/10.1029/2002GL016458.

Mitchell, D. L. 1996. "Use of Mass- and Area-Dimensional Power Laws for Determining Precipitation Particle Terminal Velocities." *Journal of the Atmospheric Sciences* 53 (12): 1710–1723. https://doi.org/10.1175/1520-0469(1996)053<1710:UOMAAD>2.0.CO;2.

Müller, D., A. Ansmann, I. Mattis, M. Tesche, U. Wandinger, D. Althausen, and G. Pisani. 2007. "Aerosol-Type-Dependent Lidar Ratios Observed with Raman Lidar." *Journal of Geophysical Research* 112 (D16): D16202. https://doi.org/10.1029/2006JD008292.

Murray, B. J., D. O'Sullivan, J. D. Atkinson, and M. E. Webb. 2012. "Ice Nucleation by Particles Immersed in Supercooled Cloud Droplets." *Chemical Society Reviews* 41 (19): 6519. https://doi.org/10.1039/c2cs35200a.

Myagkov, A., P. Seifert, M. Bauer-Pfundstein, and U. Wandinger. 2016a. "Cloud radar with hybrid mode towards estimation of shape and orientation of ice crystals." *Atmospheric Measurement Techniques* 9 (2): 469–489. https://doi.org/10.5194/amt-9-469-2016.

Myagkov, A., P. Seifert, U. Wandinger, M. Bauer-Pfundstein, and S. Y. Matrosov. 2015. "Effects of Antenna Patterns on Cloud Radar Polarimetric Measurements." *Journal of Atmospheric and Oceanic Technology* 32 (10): 1813–1828. https://doi.org/10.1175/JTECH-D-15-0045.1.

Myagkov, A., P. Seifert, U. Wandinger, J. Bühl, and R. Engelmann. 2016b. "Relationship between Temperature and Apparent Shape of Pristine Ice Crystalsderived from Polarimetric Cloud Radar Observations during the ACCEPT Campaign." *Atmospheric Measurement Techniques* 9 (8): 3739–3754. https://doi.org/10.5194/amt-9-3739-2016.

NCEP. 2000. "National Centers for Environmental Prediction FNL Operational Model Global Tropospheric Analyses continuing from July 1999." https://doi.org/10.5065/D6M043C6.

NCEP-ARL. 2020. "ARL GDAS1 Archive." Accessed December 29, 2020. https://www.ready.noaa.gov/gdas1.php.

Niedermeier, D., R. A. Shaw, S. Hartmann, H. Wex, T. Clauss, J. Voigtländer, and F. Stratmann. 2011. "Heterogeneous Ice Nucleation: Exploring the Transition from Stochastic to Singular Freezing Behavior." *Atmospheric Chemistry and Physics* 11 (16): 8767–8775. https://doi.org/10.5194/acp-11-8767-2011.

Niemand, M., O. Möhler, B. Vogel, H. Vogel, C. Hoose, P. Connolly, H. Klein, H. Bingemer, P. DeMott, J. Skrotzki, and T. Leisner. 2012. "A Particle-Surface-Area-Based Parameterization of Immersion Freezing on Desert Dust Particles." *Journal of the Atmospheric Sciences* 69 (10): 3077–3092. https://doi.org/10.1175/JAS-D-11-0249.1.

Nisantzi, A., R. E. Mamouri, A. Ansmann, G. L. Schuster, and D. G. Hadjimitsis. 2015. "Middle East versus Saharan dust extinction-to-backscatter ratios." *Atmospheric Chemistry and Physics* 15 (12): 7071–7084. https://doi.org/10.5194/acp-15-7071-2015.

O′Sullivan, D., B. J. Murray, J. F. Ross, T. F. Whale, H. C. Price, J. D. Atkinson, N. S. Umo, and M. E. Webb. 2015. "The Relevance of Nanoscale Biological Fragments for Ice Nucleation in Clouds." *Scientific Reports* 5 (1): 8082. https://doi.org/10.1038/srep08082.

Ohneiser, K., A. Ansmann, H. Baars, P. Seifert, B. Barja, C. Jimenez, M. Radenz, A. Teisseire, A. Floutsi, M. Haarig, A. Foth, A. Chudnovsky, R. Engelmann, F. Zamorano, J. Bühl, and U. Wandinger. 2020. "Smoke of extreme Australian bushfires observed in the stratosphere over Punta Arenas, Chile, in January 2020: optical thickness, lidar ratios, and depolarization ratios at 355 and 532 nm." *Atmospheric Chemistry and Physics* 20 (13): 8003–8015. https://doi.org/10.5194/acp-20-8003-2020.

Oue, M., P. Kollias, A. Ryzhkov, and E. P. Luke. 2018. "Toward Exploring the Synergy Between Cloud Radar Polarimetry and Doppler Spectral Analysis in Deep Cold Precipitating Systems in the Arctic." *Journal of Geophysical Research: Atmospheres* 123 (5): 2797–2815. https://doi.org/10.1002/2017JD027717.

Paris, J.-D., A. Stohl, P. Ciais, P. Nédélec, B. D. Belan, M. Y. Arshinov, and M. Ramonet. 2010. "Source-receptor relationships for airborne measurements of CO_2, CO and O_3 above Siberia: a cluster-based approach." *Atmospheric Chemistry and Physics* 10 (4): 1671–1687. https://doi.org/10.5194/acp-10-1671-2010.

Pearson, G., F. Davies, and C. Collier. 2009. "An Analysis of the Performance of the UFAM Pulsed Doppler Lidar for Observing the Boundary Layer." *Journal of Atmospheric and Oceanic Technology* 26 (2): 240–250. https://doi.org/10.1175/2008JTECHA1128.1.

Petters, M. D., and T. P. Wright. 2015. "Revisiting Ice Nucleation from Precipitation Samples." *Geophysical Research Letters* 42 (20): 8758–8766. https://doi.org/10.1002/2015GL065733.

Pinsky, M., A. Khain, and A. Korolev. 2014. "Analytical Investigation of Glaciation Time in Mixed-Phase Adiabatic Cloud Volumes." *Journal of the Atmospheric Sciences* 71 (11): 4143–4157. https://doi.org/10.1175/JAS-D-13-0359.1.

Pisso, I., E. Sollum, H. Grythe, N. I. Kristiansen, M. Cassiani, S. Eckhardt, D. Arnold, D. Morton, R. L. Thompson, C. D. Groot Zwaaftink, N. Evangeliou, H. Sodemann, L. Haimberger, S. Henne, D. Brunner, J. F. Burkhart, A. Fouilloux, J. Brioude, A. Philipp, P. Seibert, and A. Stohl. 2019. "The Lagrangian particle dispersion model FLEXPART version 10.4." *Geoscientific Model Development* 12 (12): 4955–4997. Accessed March 12, 2021. https://doi.org/10.5194/gmd-12-4955-2019.

Polissar, A. V., P. K. Hopke, P. Paatero, Y. J. Kaufmann, D. K. Hall, B. A. Bodhaine, E. G. Dutton, and J. M. Harris. 1999. "The aerosol at Barrow, Alaska: long-term trends and source locations." *Atmospheric Environment* 33 (16): 2441–2458. https://doi.org/10.1016/S1352-2310(98)00423-3.

Possner, A., A. M. L. Ekman, and U. Lohmann. 2017. "Cloud response and feedback processes in stratiform mixed-phase clouds perturbed by ship exhaust." *Geophysical Research Letters,* accessed March 9, 2021. https://doi.org/10.1002/2016GL071358.

Pruppacher, H., and J. Klett. 1997. *Microphysics of Clouds and Precipitation.* Dordrecht, New York: Springer.

Pummer, B. G., C. Budke, S. Augustin-Bauditz, D. Niedermeier, L. Felgitsch, C. J. Kampf, R. G. Huber, K. R. Liedl, T. Loerting, T. Moschen, M. Schauperl, M. Tollinger, C. E. Morris, H. Wex, H. Grothe, U. Pöschl, T. Koop, and J. Fröhlich-Nowoisky. 2015. "Ice Nucleation by Water-Soluble Macromolecules." *Atmospheric Chemistry and Physics* 15 (8): 4077–4091. https://doi.org/10.5194/acp-15-4077-2015.

Radenz, M., J. Bühl, V. Lehmann, U. Görsdorf, and R. Leinweber. 2018. "Combining cloud radar and radar wind profiler for a value added estimate of vertical air motion and particle terminal velocity within clouds." *Atmospheric Measurement Techniques* 11 (10): 5925–5940. https://doi.org/10.5194/amt-11-5925-2018.

Radenz, M., and J. Bühl. 2018. “Software package for added value products from combined measurements of Radar Wind Profiler and Cloud Radar (”Spectra Mole”) - Release from 2018-10-05.” https://doi.org/10.5281/zenodo.1419486.

Radenz, M., J. Bühl, P. Seifert, H. Griesche, and R. Engelmann. 2019a. “peakTree: a framework for structure-preserving radar Doppler spectra analysis.” *Atmospheric Measurement Techniques* 12 (9): 4813–4828. https://doi.org/10.5194/amt-12-4813-2019.

Radenz, M., J. Bühl, and P. Seifert. 2019b. “peakTree version of Aug2019.” https://doi.org/10.5281/zenodo.3369295.

Radenz, M., P. Seifert, H. Baars, A. A. Floutsi, Z. Yin, and J. Bühl. 2021a. “Automated time–height-resolved air mass source attribution for profiling remote sensing applications.” *Atmospheric Chemistry and Physics* 21 (4): 3015–3033. https://doi.org/10.5194/acp-21-3015-2021.

Radenz, M., J. Bühl, P. Seifert, H. Baars, R. Engelmann, B. Barja González, R.-E. Mamouri, F. Zamorano, and A. Ansmann. 2021b. “Hemispheric Contrasts in Ice Formation in Stratiform Mixed-Phase Clouds: Disentangling the Role of Aerosol and Dynamics with Ground-Based Remote Sensing.” *Atmospheric Chemistry and Physics Discussions* 2021. https://doi.org/10.5194/acp-2021-360.

Radenz, M. 2021. “martin-rdz/trace_airmass_source: trace_airmass_source jan2021.” https://doi.org/10.5281/zenodo.4438051.

Radenz, M., and J. Bühl. 2021. “larda cloud sniffer.” https://doi.org/10.5281/zenodo.4723824.

Rambukkange, M. P., J. Verlinde, E. W. Eloranta, C. J. Flynn, and E. E. Clothiaux. 2011. “Using Doppler Spectra to Separate Hydrometeor Populations and Analyze Ice Precipitation in Multilayered Mixed-Phase Clouds.” *IEEE Geoscience and Remote Sensing Letters* 8 (1): 108–112. https://doi.org/10.1109/LGRS.2010.2052781.

Ramelli, F., J. Henneberger, R. O. David, J. Bühl, M. Radenz, P. Seifert, J. Wieder, A. Lauber, J. T. Pasquier, R. Engelmann, C. Mignani, M. Hervo, and U. Lohmann. 2021. “Microphysical Investigation of the Seeder and Feeder Region of an Alpine Mixed-Phase Cloud.” *Atmospheric Chemistry and Physics* 21 (9): 6681–6706. https://doi.org/10.5194/acp-21-6681-2021.

Ray, P. S. 1972. “Broadband Complex Refractive Indices of Ice and Water.” *Applied Optics* 11 (8): 1836. https://doi.org/10.1364/AO.11.001836.

Rose, T., S. Crewell, U. Löhnert, and C. Simmer. 2005. “A network suitable microwave radiometer for operational monitoring of the cloudy atmosphere.” *Atmospheric Research* 75 (3): 183–200. https://doi.org/10.1016/j.atmosres.2004.12.005.

Rosenfeld, D., U. Lohmann, G. B. Raga, C. D. O’Dowd, M. Kulmala, S. Fuzzi, A. Reissell, and M. O. Andreae. 2008. “Flood or Drought: How Do Aerosols Affect Precipitation?” *Science* 321 (5894): 1309–1313. https://doi.org/10.1126/science.1160606.

Sato, K., S. Tateno, S. Watanabe, and Y. Kawatani. 2012. "Gravity Wave Characteristics in the Southern Hemisphere Revealed by a High-Resolution Middle-Atmosphere General Circulation Model." *Journal of the Atmospheric Sciences* 69 (4): 1378–1396. https://doi.org/10.1175/JAS-D-11-0101.1.

Seibert, P. 1993. "Convergence and Accuracy of Numerical Methods for Trajectory Calculations." Place: Boston MA, USA Publisher: American Meteorological Society, *Journal of Applied Meteorology and Climatology* 32 (3): 558–566. https://doi.org/10.1175/1520-0450(1993)032<0558:CAAONM>2.0.CO;2.

Seifert, A., and K. D. Beheng. 2006. "A Two-Moment Cloud Microphysics Parameterization for Mixed-Phase Clouds. Part 1: Model Description." *Meteorology and Atmospheric Physics* 92 (1-2): 45–66. https://doi.org/10.1007/s00703-005-0112-4.

Seifert, A., C. Köhler, and K. D. Beheng. 2012. "Aerosol-cloud-precipitation effects over Germany as simulated by a convective-scale numerical weather prediction model." *Atmospheric Chemistry and Physics* 12, no. 2 (January 16, 2012): 709–725. https://doi.org/10.5194/acp-12-709-2012.

Seifert, P., A. Ansmann, I. Mattis, U. Wandinger, M. Tesche, R. Engelmann, D. Müller, C. Pérez, and K. Haustein. 2010. "Saharan dust and heterogeneous ice formation: Eleven years of cloud observations at a central European EARLINET site." *Journal of Geophysical Research: Atmospheres* 115 (D20): D20201. https://doi.org/10.1029/2009JD013222.

Seifert, P., C. Kunz, H. Baars, A. Ansmann, J. Bühl, F. Senf, R. Engelmann, D. Althausen, and P. Artaxo. 2015. "Seasonal variability of heterogeneous ice formation in stratiform clouds over the Amazon Basin." *Geophysical Research Letters* 42 (13): 5587–5593. https://doi.org/10.1002/2015gl064068.

Seinfeld, J. H., C. Bretherton, K. S. Carslaw, H. Coe, P. J. DeMott, E. J. Dunlea, G. Feingold, S. Ghan, A. B. Guenther, R. Kahn, I. Kraucunas, S. M. Kreidenweis, M. J. Molina, A. Nenes, J. E. Penner, K. A. Prather, V. Ramanathan, V. Ramaswamy, P. J. Rasch, A. R. Ravishankara, D. Rosenfeld, G. Stephens, and R. Wood. 2016. "Improving Our Fundamental Understanding of the Role of Aerosol-cloud Interactions in the Climate System." *Proceedings of the National Academy of Sciences* 113 (21): 5781–5790. https://doi.org/10.1073/pnas.1514043113.

Shao, Q., D. A. Randall, C.-H. Moeng, and R. E. Dickinson. 1997. "A Method to Determine the Amounts of Cloud-Top Radiative and Evaporative Cooling in a Stratocumulus-Topped Boundary Layer." *Quarterly Journal of the Royal Meteorological Society* 123 (544): 2187–2213. https://doi.org/10.1002/qj.49712354403.

Shupe, M. D., P. Kollias, S. Y. Matrosov, and T. L. Schneider. 2004. "Deriving Mixed-Phase Cloud Properties from Doppler Radar Spectra." *Journal of Atmospheric and Oceanic Technology* 21 (4): 660–670. Accessed October 12, 2015. https://doi.org/10.1175/1520-0426(2004)021<0660:DMCPFD>2.0.CO;2.

Silber, I., A. M. Fridlind, J. Verlinde, L. M. Russell, and A. S. Ackerman. 2020. "Nonturbulent Liquid-Bearing Polar Clouds: Observed Frequency of Occurrence and

Simulated Sensitivity to Gravity Waves." *Geophysical Research Letters* 47 (10): e2020GL087099. https://doi.org/10.1029/2020GL087099.

Silber, I., J. Verlinde, E. W. Eloranta, and M. Cadeddu. 2018. "Antarctic Cloud Macrophysical, Thermodynamic Phase, and Atmospheric Inversion Coupling Properties at McMurdo Station: I. Principal Data Processing and Climatology." *Journal of Geophysical Research: Atmospheres* 123 (11): 6099–6121. https://doi.org/10.1029/2018JD028279.

Simmel, M., J. Bühl, A. Ansmann, and I. Tegen. 2015. "Ice Phase in Altocumulus Clouds over Leipzig: Remote Sensing Observations and Detailed Modeling." *Atmospheric Chemistry and Physics* 15 (18): 10453–10470. https://doi.org/10.5194/acp-15-10453-2015.

Solomon, A., G. de Boer, J. M. Creamean, A. McComiskey, M. D. Shupe, M. Maahn, and C. Cox. 2018. "The relative impact of cloud condensation nuclei and ice nucleating particle concentrations on phase partitioning in Arctic mixed-phase stratocumulus clouds." *Atmospheric Chemistry and Physics* 18, no. 23 (December 3, 2018): 17047–17059. Accessed February 11, 2021. https://doi.org/10.5194/acp-18-17047-2018.

Stein, A. F., R. R. Draxler, G. D. Rolph, B. J. B. Stunder, M. D. Cohen, and F. Ngan. 2015. "NOAA's HYSPLIT Atmospheric Transport and Dispersion Modeling System." *Bulletin of the American Meteorological Society* 96 (12): 2059–2077. https://doi.org/10.1175/BAMS-D-14-00110.1.

Stohl, A., C. Forster, A. Frank, P. Seibert, and G. Wotawa. 2005. "Technical note: The Lagrangian particle dispersion model FLEXPART version 6.2." *Atmospheric Chemistry and Physics* 5 (9): 2461–2474. Accessed March 12, 2021. https://doi.org/10.5194/acp-5-2461-2005.

Stohl, A., S. Eckhardt, C. Forster, P. James, N. Spichtinger, and P. Seibert. 2002. "A replacement for simple back trajectory calculations in the interpretation of atmospheric trace substance measurements." *Atmospheric Environment* 36 (29): 4635–4648. Accessed March 12, 2021. https://doi.org/10.1016/S1352-2310(02)00416-8.

Stohl, A., G. Wotawa, P. Seibert, and H. Kromp-Kolb. 1995. "Interpolation Errors in Wind Fields as a Function of Spatial and Temporal Resolution and Their Impact on Different Types of Kinematic Trajectories." Place: Boston MA, USA Publisher: American Meteorological Society, *Journal of Applied Meteorology and Climatology* 34 (10): 2149–2165. https://doi.org/10.1175/1520-0450(1995)034<2149:IEIWFA>2.0.CO;2.

Sulia, K. J., and J. Y. Harrington. 2011. "Ice Aspect Ratio Influences on Mixed-Phase Clouds: Impacts on Phase Partitioning in Parcel Models." *Journal of Geophysical Research: Atmospheres* 116 (D21). https://doi.org/10.1029/2011JD016298.

Tan, I., T. Storelvmo, and Y.-S. Choi. 2014. "Spaceborne lidar observations of the ice-nucleating potential of dust, polluted dust, and smoke aerosols in mixed-phase

clouds." *Journal of Geophysical Research: Atmospheres* 119 (11): 6653–6665. https://doi.org/10.1002/2013JD021333.

Tarasova, O. A., I. A. Senik, M. G. Sosonkin, J. Cui, J. Staehelin, and A. S. H. Prévôt. 2009. "Surface ozone at the Caucasian site Kislovodsk High Mountain Station and the Swiss Alpine site Jungfraujoch: data analysis and trends (1990–2006)." *Atmospheric Chemistry and Physics* 9 (12): 4157–4175. Accessed March 12, 2021. https://doi.org/10.5194/acp-9-4157-2009.

Tegen, I., P. Hollrig, M. Chin, I. Fung, D. Jacob, and J. Penner. 1997. "Contribution of Different Aerosol Species to the Global Aerosol Extinction Optical Thickness: Estimates from Model Results." *Journal of Geophysical Research: Atmospheres* 102 (D20): 23895–23915. https://doi.org/10.1029/97JD01864.

Tesche, M., A. Ansmann, D. Müller, D. Althausen, R. Engelmann, V. Freudenthaler, and S. Groß. 2009. "Vertically resolved separation of dust and smoke over Cape Verde using multiwavelength Raman and polarization lidars during Saharan Mineral Dust Experiment 2008." *Journal of Geophysical Research: Atmospheres* 114 (D13): D13202. https://doi.org/10.1029/2009JD011862.

Tesche, M., S. Gross, A. Ansmann, D. Müller, D. Althausen, V. Freudenthaler, and M. Esselborn. 2011. "Profiling of Saharan dust and biomass-burning smoke with multiwavelength polarization Raman lidar at Cape Verde." *Tellus B: Chemical and Physical Meteorology* 63 (4): 649–676. https://doi.org/10.1111/j.1600-0889.2011.00548.x.

Tobo, Y., A. J. Prenni, P. J. DeMott, J. A. Huffman, C. S. McCluskey, G. Tian, C. Pöhlker, U. Pöschl, and S. M. Kreidenweis. 2013. "Biological Aerosol Particles as a Key Determinant of Ice Nuclei Populations in a Forest Ecosystem." *Journal of Geophysical Research: Atmospheres* 118 (17): 10, 100–10, 110. https://doi.org/10.1002/jgrd.50801.

Trenberth, K. E., and J. T. Fasullo. 2010. "Simulation of Present-Day and Twenty-First-Century Energy Budgets of the Southern Oceans." *Journal of Climate* 23 (2): 440–454. https://doi.org/10.1175/2009JCLI3152.1.

Val Martin, M., R. Kahn, and M. Tosca. 2018. "A Global Analysis of Wildfire Smoke Injection Heights Derived from Space-Based Multi-Angle Imaging." *Remote Sensing* 10 (10): 1609. Accessed March 12, 2021. https://doi.org/10.3390/rs10101609.

Vali, G. 2014. "Interpretation of Freezing Nucleation Experiments: Singular and Stochastic; Sites and Surfaces." *Atmospheric Chemistry and Physics* 14 (11): 5271–5294. https://doi.org/10.5194/acp-14-5271-2014.

Vali, G., P. J. DeMott, O. Möhler, and T. F. Whale. 2015. "Technical Note: A Proposal for Ice Nucleation Terminology." *Atmospheric Chemistry and Physics* 15 (18): 10263–10270. https://doi.org/10.5194/acp-15-10263-2015.

Vergara-Temprado, J., B. J. Murray, T. W. Wilson, D. O'Sullivan, J. Browse, K. J. Pringle, K. Ardon-Dryer, A. K. Bertram, S. M. Burrows, D. Ceburnis, P. J. DeMott, R. H. Mason, C. D. O'Dowd, M. Rinaldi, and K. S. Carslaw. 2017. "Contribution of feldspar and marine organic aerosols to global ice nucleating particle

concentrations." *Atmospheric Chemistry and Physics* 17 (5): 3637–3658. https://doi.org/10.5194/acp-17-3637-2017.

Veselovskii, I., D. N. Whiteman, M. Korenskiy, A. Suvorina, A. Kolgotin, A. Lyapustin, Y. Wang, M. Chin, H. Bian, T. L. Kucsera, D. Pérez-Ramírez, and B. Holben. 2015. "Characterization of forest fire smoke event near Washington, DC in summer 2013 with multi-wavelength lidar." *Atmospheric Chemistry and Physics* 15 (4): 1647–1660. https://doi.org/10.5194/acp-15-1647-2015.

Vignon, É., S. P. Alexander, P. J. DeMott, G. Sotiropoulou, F. Gerber, T. C. J. Hill, R. Marchand, A. Nenes, and A. Berne. 2021. "Challenging and Improving the Simulation of Mid-level Mixed-phase Clouds over the High-latitude Southern Ocean." *Journal of Geophysical Research: Atmospheres,* https://doi.org/10.1029/2020JD033490.

Villanueva, D., B. Heinold, P. Seifert, H. Deneke, M. Radenz, and I. Tegen. 2020. "The day-to-day co-variability between mineral dust and cloud glaciation: a proxy for heterogeneous freezing." *Atmospheric Chemistry and Physics* 20 (4): 2177–2199. https://doi.org/10.5194/acp-20-2177-2020.

Villanueva, D., F. Senf, and I. Tegen. 2021. "Hemispheric and Seasonal Contrast in Cloud Thermodynamic Phase From A-Train Spaceborne Instruments." *Journal of Geophysical Research: Atmospheres* 126 (6). https://doi.org/10.1029/2020JD034322.

Wang, Z., and K. Sassen. 2002. "Cirrus Cloud Microphysical Property Retrieval Using Lidar and Radar Measurements. Part I: Algorithm Description and Comparison with In Situ Data." *Journal of Applied Meteorology* 41 (3): 218–229. https://doi.org/10.1175/1520-0450(2002)041<0218:CCMPRU>2.0.CO;2.

Wang, Z., K. Sassen, D. N. Whiteman, and B. B. Demoz. 2004. "Studying Altocumulus with Ice Virga Using Ground-Based Active and Passive Remote Sensors." *Journal of Applied Meteorology* 43 (3): 449–460. https://doi.org/10.1175/1520-0450(2004)043<0449:SAWIVU>2.0.CO;2.

Weger, M., B. Heinold, C. Engler, U. Schumann, A. Seifert, R. Fößig, C. Voigt, H. Baars, U. Blahak, S. Borrmann, C. Hoose, S. Kaufmann, M. Krämer, P. Seifert, F. Senf, J. Schneider, and I. Tegen. 2018. "The Impact of Mineral Dust on Cloud Formation during the Saharan Dust Event in April 2014 over Europe." *Atmospheric Chemistry and Physics* 18 (23): 17545–17572. https://doi.org/10.5194/acp-18-17545-2018.

Weinzierl, B., and A-LIFE Science Team. 2021. *The A-LIFE Field Experiment in the Eastern Mediterranean - Overview and Selected Highlights.* Other. pico. https://doi.org/10.5194/egusphere-egu21-16129.

Welti, A., E. K. Bigg, P. J. DeMott, X. Gong, M. Hartmann, M. Harvey, S. Henning, P. Herenz, T. C. J. Hill, B. Hornblow, C. Leck, M. Löffler, C. S. McCluskey, A. M. Rauker, J. Schmale, C. Tatzelt, M. van Pinxteren, and F. Stratmann. 2020. "Ship-Based Measurements of Ice Nuclei Concentrations over the Arctic, Atlantic, Pacific

and Southern Oceans." *Atmospheric Chemistry and Physics* 20 (23): 15191–15206. https://doi.org/10.5194/acp-20-15191-2020.

Wernli, B. H., and H. C. Davies. 1997. "A lagrangian-based analysis of extratropical cyclones. I: The method and some applications." *Quarterly Journal of the Royal Meteorological Society* 123 (538): 467–489. Accessed March 12, 2021. https://doi.org/10.1002/qj.49712353811.

Westbrook, C. D., and A. J. Illingworth. 2011. "Evidence That Ice Forms Primarily in Supercooled Liquid Clouds at Temperatures > -27°C." *Geophysical Research Letters* 38 (14). https://doi.org/10.1029/2011GL048021.

———. 2013. "The Formation of Ice in a Long-Lived Supercooled Layer Cloud." *Quarterly Journal of the Royal Meteorological Society* 139 (677): 2209–2221. https://doi.org/10.1002/qj.2096.

Wu, P., X. Dong, B. Xi, J. Tian, and D. M. Ward. 2020. "Profiles of MBL Cloud and Drizzle Microphysical Properties Retrieved From Ground-Based Observations and Validated by Aircraft In Situ Measurements Over the Azores." *Journal of Geophysical Research: Atmospheres* 125 (9). https://doi.org/10.1029/2019JD032205.

Yin, Z., A. Ansmann, H. Baars, P. Seifert, R. Engelmann, M. Radenz, C. Jimenez, A. Herzog, K. Ohneiser, K. Hanbuch, L. Blarel, P. Goloub, G. Dubois, S. Victori, and F. Maupin. 2019. "Aerosol Measurements with a Shipborne Sun–Sky–Lunar Photometer and Collocated Multiwavelength Raman Polarization Lidar over the Atlantic Ocean." *Atmospheric Measurement Techniques* 12 (10): 5685–5698. https://doi.org/10.5194/amt-12-5685-2019.

Yin, Z., and H. Baars. 2021. "PollyNET/Pollynet_Processing_Chain: Version 2.1." https://doi.org/10.5281/zenodo.4694451.

Yu, G., J. Verlinde, E. E. Clothiaux, and Y.-S. Chen. 2014. "Mixed-phase cloud phase partitioning using millimeter wavelength cloud radar Doppler velocity spectra." *Journal of Geophysical Research: Atmospheres* 119 (12): 7556–7576. Accessed September 2, 2018. https://doi.org/10.1002/2013JD021182.

Zaremba, T. J., R. M. Rauber, G. M. McFarquhar, M. Hayman, J. A. Finlon, and D. M. Stechman. 2020. "Phase Characterization of Cold Sector Southern Ocean Cloud Tops: Results from SOCRATES." E2020JD033673 2020JD033673, *Journal of Geophysical Research: Atmospheres* n/a (n/a): e2020JD033673. https://doi.org/10.1029/2020JD033673.

Zhang, D., Z. Wang, P. Kollias, A. M. Vogelmann, K. Yang, and T. Luo. 2018. "Ice particle production in mid-level stratiform mixed-phase clouds observed with collocated A-Train measurements." *Atmospheric Chemistry and Physics* 18 (6): 4317–4327. https://doi.org/10.5194/acp-18-4317-2018.

Zhang, D., Z. Wang, A. Heymsfield, J. Fan, and T. Luo. 2014. "Ice Concentration Retrieval in Stratiform Mixed-Phase Clouds Using Cloud Radar Reflectivity Measurements and 1D Ice Growth Model Simulations." *Journal of the Atmospheric Sciences* 71 (10): 3613–3635. https://doi.org/10.1175/JAS-D-13-0354.1.

Zhao, X., X. Liu, S. M. Burrows, and Y. Shi. 2021. “Effects of Marine Organic Aerosols as Sources of Immersion-Mode Ice-Nucleating Particles on High-Latitude Mixed-Phase Clouds.” *Atmospheric Chemistry and Physics* 21 (4): 2305–2327. https://doi.org/10.5194/acp-21-2305-2021.

Acknowledgements

This work would not have been possible without the company, guidance, and support by a lot of people. I owe gratitude to all of them. Especially I would like to thank the following people:
Andreas Macke for supervising this thesis. Ulla and Albert for your trust and the freedom to letting me explore my ideas, but pushing me back on track whenever needed. Ulla for her efforts to improve my writing. Johannes and Patric for everything. I won't dare to start to list all of the things, but particularly for your feedback and support in the final phase. The whole ~~lidar~~ ground-based remote sensing group for making all the challenges a team effort and for lively coffee break discussions. Holger for his efforts to teach me the details of lidar techniques and his patience during my humble tries. Ronny for getting me onboard the ship and always sharing his knowledge on any piece of technology. Dietrich for his advice on how to run measurements almost anywhere. Karsten for discussing about optics and mechanics and sharing the hot sauce. Annett and Birgit for their support on all the small things. Volker and Alexander for getting me hooked with the radar stuff — you set the bar pretty high. The administration and workshop of TROPOS for getting me and the instruments in functioning to all the places (and back). The remote sensing group of LIM, especially Heike, Teresa, Willi, and Andi for being part of DACAPO-PESO and the joint hacking sessions. Heike and the in-situ group for the scientific discussions. To my fellow PhD students at LIM and TROPOS (Cristofer, Hannes, Moritz, Athena, Julian, Sebastian, Jan, Teresa, Willi, Robert, Nadja, Daniel, Zhenping, and many more) for sharing the struggle, the successes, and some beers.

Also I want to thank everyone, who joined me in the field and at sea, making stuff work in 'the trenches of climate science'. Without you a lot things would not have worked out and the whole endeavor would not have been the joy it was. Countless shared memories are connected to that part of the work: Stepping on board Polarstern for the first time, dust storms downtown Punta Arenas, hilltop location scouting for the DACAPO-PESO in-situ part, MET-City being different every time we visited, attempting to debug iptables without google, stepping off Polarstern – hopefully not for the last time, and always seeing the green beam above all these locations, once the sun set.

Muchas gracias a Boris, Raúl, Israel y Félix por sus incansables esfuerzos. Sin ti, nada de esto habría sido posible.

And, most importantly, thanks to my friends and family for unconditionally supporting me during all lows and highs, regardless what I am pursuing. Danke für euren Rückhalt!